Applied Computational Electromagnetics Society

Journal

March 2011 Vol. 26 No. 3

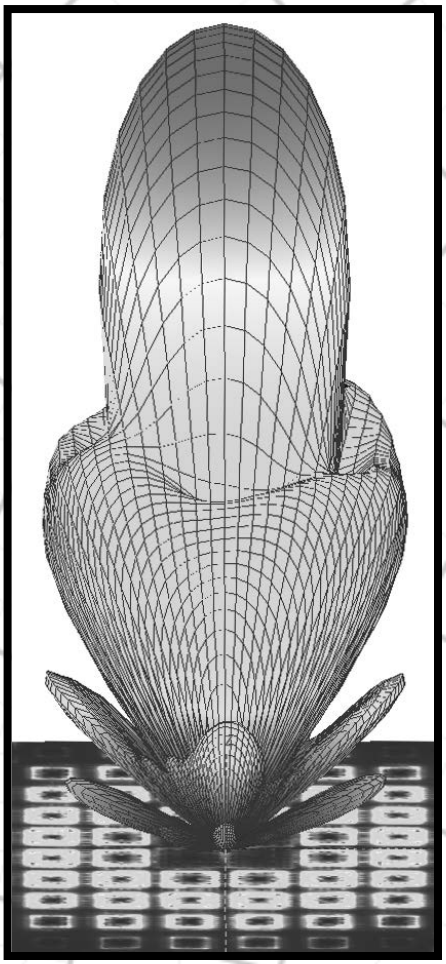

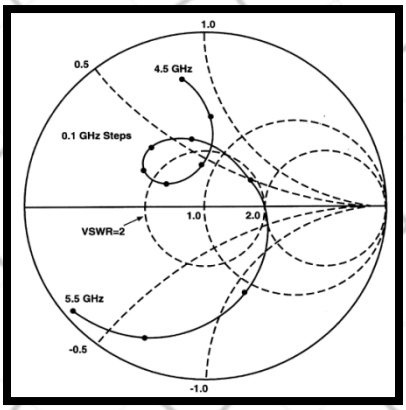

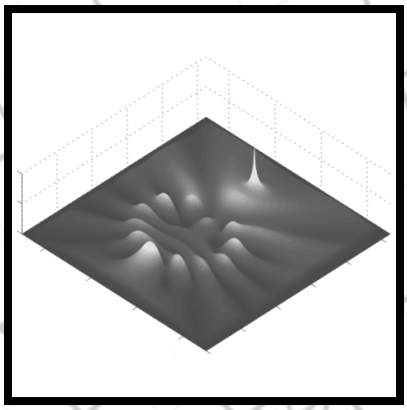

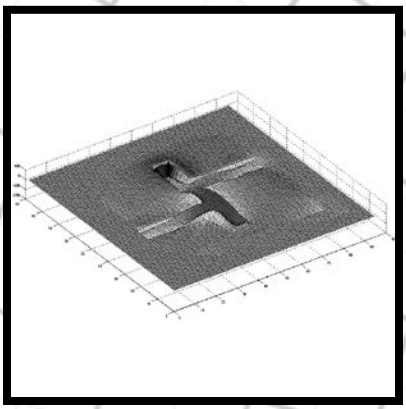

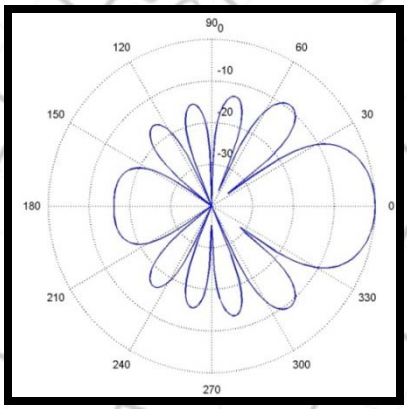

ISSN 1054-4887

GENERAL PURPOSE AND SCOPE: The Applied Computational Electromagnetics Society ***(ACES)*** Journal hereinafter known as the ***ACES Journal*** is devoted to the exchange of information in computational electromagnetics, to the advancement of the state-of-the art, and the promotion of related technical activities. The primary objective of the information exchange is to inform the scientific community on the developments of new computational electromagnetics tools and their use in electrical engineering, physics, or related areas. The technical activities promoted by this publication include code validation, performance analysis, and input/output standardization; code or technique optimization and error minimization; innovations in solution technique or in data input/output; identification of new applications for electromagnetics modeling codes and techniques; integration of computational electromagnetics techniques with new computer architectures; and correlation of computational parameters with physical mechanisms.

SUBMISSIONS: The ***ACES Journal*** welcomes original, previously unpublished papers, relating to applied computational electromagnetics. Typical papers will represent the computational electromagnetics aspects of research in electrical engineering, physics, or related disciplines. However, papers which represent research in applied computational electromagnetics itself are equally acceptable.

Manuscripts are to be submitted through the upload system of ***ACES*** web site http://aces.ee.olemiss.edu See "Information for Authors" on inside of back cover and at ***ACES*** web site. For additional information contact the Editor-in-Chief:

Dr. Atef Elsherbeni
Department of Electrical Engineering
The University of Mississippi
University, MS 386377 USA
Phone: 662-915-5382
Email: atef@olemiss.edu

SUBSCRIPTIONS: All members of the Applied Computational Electromagnetics Society are entitled to access and download the ***ACES Journal*** any published journal article available at http://aces.ee.olemiss.edu. Printed issues of the ***ACES Journal*** are delivered to institutional members. Each author of published papers receives a printed issue of the ***ACES Journal*** in which the paper is published.

Back issues, when available, are $50 each. Subscription to ***ACES*** is through the web site. Orders for back issues of the ***ACES Journal*** and change of address requests should be sent directly to ***ACES*** office at:

Department of Electrical Engineering
The University of Mississippi
University, MS 386377 USA
Phone: 662-915-7231
Email: aglisson@olemiss.edu

Allow four weeks advance notice for change of address. Claims for missing issues will not be honored because of insufficient notice, or address change, or loss in the mail unless the ***ACES*** office is notified within 60 days for USA and Canadian subscribers, or 90 days for subscribers in other countries, from the last day of the month of publication. For information regarding reprints of individual papers or other materials, see "Information for Authors".

LIABILITY. Neither ***ACES***, nor the ***ACES Journal*** editors, are responsible for any consequence of misinformation or claims, express or implied, in any published material in an ***ACES Journal*** issue. This also applies to advertising, for which only camera-ready copies are accepted. Authors are responsible for information contained in their papers. If any material submitted for publication includes material which has already been published elsewhere, it is the author's responsibility to obtain written permission to reproduce such material.

APPLIED COMPUTATIONAL ELECTROMAGNETICS SOCIETY JOURNAL

March 2011
Vol. 26 No. 3
ISSN 1054-4887

The ACES Journal is abstracted in INSPEC, in Engineering Index, DTIC, Science Citation Index Expanded, the Research Alert, and to Current Contents/Engineering, Computing & Technology.

The illustrations on the front cover have been obtained from the research groups at the Department of Electrical Engineering, The University of Mississippi.

MARCH 2011 REVIEWERS

Iftikhar Ahmed
Shirook Ali
Rodolfo Araneo
Sami Barmada
Gerard Berginc
David Chen
Nirod Das
Khaled ElMahgoub
Jieran Fang
Amir Hajiaboli
Mr. Idula
Leo Kempel
Fadi Khalil
Gordon MacDonald
Zhen Peng
C. J. Reddy
Randall Reeves
Luca Rienzo
Colan Ryan
António Espírito Santo
Yury Shestopalov
Yasuhiro Tsunemitsu
Su Yan
Wenhua Yu

THE APPLIED COMPUTATIONAL ELECTROMAGNETICS SOCIETY

JOURNAL

Vol. 26 No. 3 March 2011

TABLE OF CONTENTS

Homogenization of Thin Dielectric Composite Slabs: Techniques and Limitations

Henrik Kettunen, Jiaran Qi, Henrik Wallén, and Ari Sihvola

Department of Radio Science and Engineering
Aalto University School of Electrical Engineering
PO Box 13000, FI-00076 Aalto, Finland
henrik.kettunen@aalto.fi qi.jiaran@aalto.fi henrik.wallen@aalto.fi ari.sihvola@aalto.f

Abstract – This paper compares different methods for retrieving the transverse effective permittivity of periodic composite slabs whose longitudinal thickness is only a few unit cells. Two computational methods are considered, one based on simulated scattering parameters (S-parameters) and the other one based on fiel averaging by integration. The effect of frequency dispersion is studied by comparing the results with electrostatic estimates given by analytical mixing formulas. Furthermore, the influenc of the slab thickness is studied. We also discuss the boundary effects on the interfaces of the slabs.

Index Terms – Boundary transition layers, effective permittivity, fiel averaging, S-parameters.

I. INTRODUCTION

Heterogeneous media, such as composite materials, are often treated as effectively homogeneous materials [1, 2, 3]. The idea and the benefi of this approximative modeling is that the complex internal microstucture of the material can be forgotten and the material characteristics are averaged into a macroscopic scale. That is, the electromagnetic behavior of the material is described only by two (effective) parameters, the electric permittivity ϵ and the magnetic permeability μ. Such an approximation actually applies to all conventional bulk materials, as well. Naturally, the condition of such homogenization is that the inhomogeneities of the material are very small with respect to the wavelengths of the impinging electromagnetic fields

Once being able to analyze the effective behavior of composite materials, we can go the other way round and see the possibility of synthesizing new artificia materials with desired effective response. In theory, it is possible to create materials even with properties not readily existing in nature. These so called metamaterials have lately been under major interest [4, 5]. However, the homogenization of many proposed materials very seldom goes without problems or doubts [6, 7].

In this paper, we focus on a homogenization of a very simple dielectric structure in order to investigate some fundamental characteristics and limitations of material homogenization. We consider a composite slab consisting of dielectric spheres arranged in a periodic simple cubic lattice in vacuum. The slab is infinit in the transverse plane but in the longitudinal dimension it is only a few layers thick. The slab is excited with a normally incident time-harmonic plane wave (see Fig. 1). The structure is assumed nonmagnetic, *i.e.*, $\mu = \mu_0$, which, for instance, is reasonable when studying polymeric composite materials [8]. Therefore, the only parameter we are retrieving is the effective permittivity ϵ_{eff}, which is a dimensionless number relative to the permittivity of vacuum ϵ_0. Moreover, the spheres are assumed dispersionless and lossless.

In this article, we study the homogenization in a dynamic case in order to see how quickly and strongly the increase of the electrical size of the unit cell makes the effective permittivity estimate deviate from the (quasi)static value. Furthermore, an important objective of this paper is to study how the thickness of the slab, *i.e.*, the number of consecutive unit cell layers, affects the retrieval results.

The simulations are performed using COMSOL

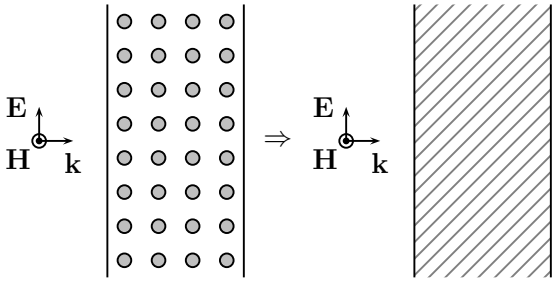

Fig. 1. The original composite medium consisting of a periodic lattice of spherical inclusions is modeled as an effectively homogeneous material.

MULTIPHYSICS 3.5 (3D RF Module, Electromagnetic Waves, Harmonic Propagation), which is a commercial software based on the finite element method (FEM).

In parallel, another related homogenization study is going on, where we more extensively consider the effect of frequency dispersion for a composite slab and an infinite periodic lattice. In those simulations, CST MICROWAVE STUDIO is used. The results of this research are reported in [9]

II. COMPUTATIONAL MODEL OF THE GEOMETRY

The composite slab consists of spheres in a simple cubic lattice, *i.e.*, the unit cell is a cube with a concentric sphere inside (see Fig. 2). The unit cell side length is denoted by a. We consider a composite where the spherical inclusions occupy a volume fraction of $p = 1/4$, *i.e.*, the radii of the spheres become $r = a\sqrt[3]{3/(16\pi)}$. The relative permittivity of the spheres is $\epsilon_{\mathrm{i}} = 10$ and the background material is vacuum with $\epsilon_{\mathrm{e}} = 1$.

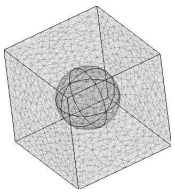

Fig. 2. The unit cell is an $a \times a \times a$ cube with a dielectric sphere inside.

We only consider the case where a linearly polarized transverse electromagnetic (TEM) plane wave is normally incident on the composite slab. In this case, the transverse periodical symmetry of the slab can be modeled using perfect electric conductor (PEC) and perfect magnetic conductor (PMC) boundary conditions. To achieve the desired periodicity, PEC boundaries are placed perpendicularly and PMC boundaries parallel to the chosen direction of the electric field vector. Due to the symmetry of the unit cells, with normal incidence, only one quarter of the unit cells needs to be modeled in the transverse direction, which essentially reduces the computational cost. More general periodic boundary conditions could also be applied, but in that case the whole cells must be modeled. In the longitudinal direction, *i.e.*, the direction of the plane wave propagation, we have to model all the consecutive layers of cells in the slab. We consider three configurations, slabs with thickness of 1, 5, and 9 layers of unit cells. On both sides of the slab, the width of two unit cells of free space is added to ensure sufficient attenuation of possible evanescent higher order modes. The computational domain is terminated with ports, which give rise to the TEM plane wave and allow the computation of the S-parameters. Figure 3 presents the actual modeled geometry in the case of 5 layers.

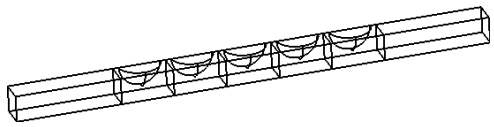

Fig. 3. Example of the modeled geometry with 5 layers.

The geometry is discretized with a tetrahedral mesh. The accuracy of the mesh should remain roughly equal for all geometry configurations, *i.e.*, slabs with a different number of layers. For a certain slab, the same mesh is applied for all frequencies, that is, when we perform a frequency sweep, the mesh needs to be created only once. The field solution is constructed using quadratic vector elements. In our simulations, for slabs with 1, 5, and 9 layers, the meshes consist of 7949, 13997, and 21013 elements, yielding 55148, 97286, and 145626 degrees of freedom, respectively. The simulations are run using a desktop PC with Intel Core 2 Duo CPU 2.66 GHz and 4 GB of RAM. For example, in the case of 5 layers, a sweep of 200 frequency points takes 2141 sec-

onds, which is a little less than 11 seconds per each frequency point.

To validate our simulation results, we also modeled the 5 layered case using the frequence-domain solver of CST MICROWAVE STUDIO (MWS). The geometry setup and the boundary conditions are the same as described above. The unit cell side length was chosen $a = 0.01\,\mathrm{m}$. Figure 4 shows the absolute difference between the obtained S-parameter results, which in the considered frequency range is of the order of 10^{-3}.

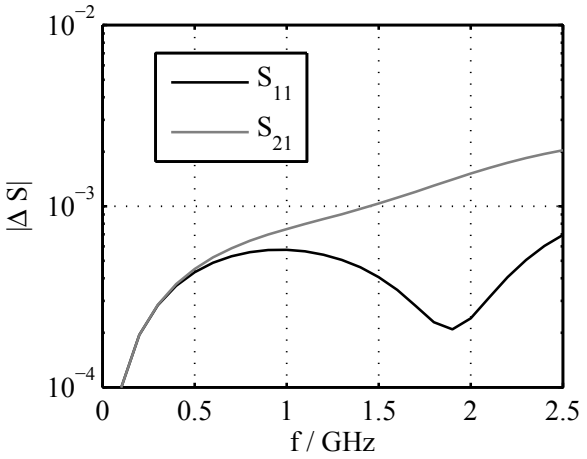

Fig. 4. The difference in simulated S-parameters between COMSOL and CST MWS.

We are considering an electrodynamic case where a propagating wave interacts with the composite material. However, the unit cells must be small enough with respect to the wavelength for the material to behave as homogeneous, so, in that sense, we are near the (quasi)static limit. For convenience, we choose a reference frequency where the edge length of one unit cell equals 1/20 of the wavelength, *i.e.*, $a = \lambda/20$. The wavelength should not, however, be considered the free-space wavelength but the reduced (effective) one inside the material. Therefore, the corresponding reference frequency,

$$f_{20} = \frac{c}{20a\sqrt{\epsilon_{\text{eff}}}}, \tag{1}$$

where c denotes the speed of light in vacuum, depends on the effective permittivity, which is the unknown parameter we are solving. A reasonable a priori estimate is considered in the following.

III. ELECTROSTATIC MIXING RULES

In the electrostatic limit, the effective permittivity of an infinite lattice can be estimated by various analytical mixing formulas [10]. One of the most famous and simplest mixing rules suitable for this case is the Maxwell Garnett (MG) formula, which using the above-mentioned parameter values ($\epsilon_{\text{i}} = 10$, $\epsilon_{\text{e}} = 1$ and $p = 1/4$) gives

$$\epsilon_{\text{eff}} = \epsilon_{\text{e}} + 3p\epsilon_{\text{e}}\frac{\epsilon_{\text{i}} - \epsilon_{\text{e}}}{\epsilon_{\text{i}} + 2\epsilon_{\text{e}} - p(\epsilon_{\text{i}} - \epsilon_{\text{e}})} \approx 1.6923. \tag{2}$$

A more accurate estimate is given by the Lord Rayleigh mixing rule

$$\epsilon_{\text{eff}} = \epsilon_{\text{e}} + \frac{3p\epsilon_{\text{e}}}{\frac{\epsilon_{\text{i}}+2\epsilon_{\text{e}}}{\epsilon_{\text{i}}-\epsilon_{\text{e}}} - p - 1.305\frac{\epsilon_{\text{i}}-\epsilon_{\text{e}}}{\epsilon_{\text{i}}+4\epsilon_{\text{e}}/3}p^{10/3}} \approx 1.6989, \tag{3}$$

and an even more accurate one by the mixing formula derived by McPhedran and McKenzie [11], $\epsilon_{\text{eff}} \approx 1.6990$, which we will use as a static bulk reference value in Eq. (1).

IV. S-PARAMETER RETRIEVAL

The widely applied S-parameter retrieval method is based on measured or simulated reflection and transmission data, namely S_{11} and S_{21}. The method is often referred to as Nicolson–Ross–Weir (NRW) technique named after its originators [12, 13]. Along with the metamaterials research this method has required certain modifications [14, 15].

The normalized impedance z is obtained by

$$z = \pm\sqrt{\frac{(1+S_{11})^2 - S_{21}^2}{(1-S_{11})^2 - S_{21}^2}}, \tag{4}$$

where the sign must be chosen so that the real part of z is positive. The exponent function including the refractive index n is then given by

$$x = e^{-jnk_0d} = \frac{S_{21}}{1 - S_{11}\frac{z-1}{z+1}}, \tag{5}$$

where $k_0 = \omega\sqrt{\epsilon_0\mu_0}$ is the free-space wave number and d is the thickness of the slab. This method aims at solving both ϵ_{eff} and μ_{eff} by $\epsilon_{\text{eff}} = n/z$ and $\mu_{\text{eff}} = nz$. However, the solution is not unambiguous due to the branches of the logarithm function. The refractive index becomes

$$n = \frac{1}{k_0 d}(j\ln x + 2\pi m), \quad m = 0, 1, 2, \ldots \tag{6}$$

If both ϵ_{eff} and μ_{eff} are unknown, or the material is strongly dispersive, determining the integer m may become difficult. However, as in our case the composite is assumed non-dispersive and non-magnetic, the correct value for the integer m can simply be adjusted by the condition $\mu_{\text{eff}} = nz \approx 1$.

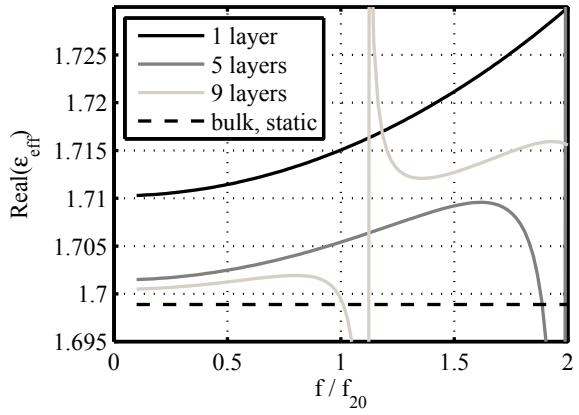

Fig. 5. The retrieved effective permittivity (real part) for different number of layers.

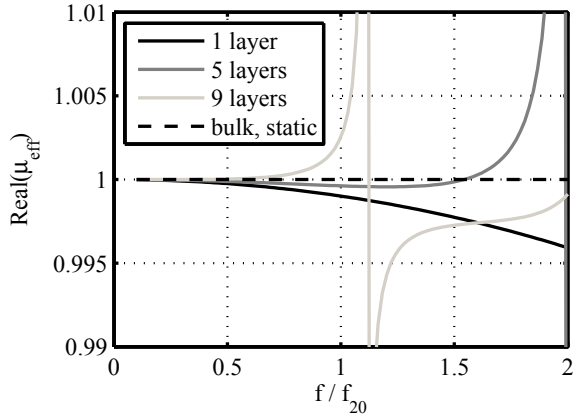

Fig. 6. The retrieved effective permeability (real part) for different number of layers.

Problems appear, when the total effective thickness of the slab becomes $\lambda/2$, or any integer multiple of it. At such frequencies, there occurs a Fabry–Pérot type of resonance where the wave passes through the lossless slab without any reflection. Although the Fabry–Pérot resonance is a natural response of the slab, it should not affect the material parameter retrieval results. However, as $S_{11} = 0$ and $|S_{21}| = 1$, the impedance z cannot be solved correctly by Eq. (4), which causes the resonances to transfer also to the retrieved parameters ϵ_{eff} and μ_{eff} (see Figs. 5 and 6, respectively). Naturally, these resonances in permittivity and permeability are not physical properties of the studied material but a characteristic of the retrieval method. Moreover, the behavior of ϵ_{eff} is anti-resonant, *i.e.*, near the resonance the permittivity decreases with increasing frequency, which violates the principle of causality (see Fig. 5).

The retrieval also yields very small imaginary parts for ϵ_{eff} and μ_{eff} (not plotted herein). At the resonance, their maximum level is of the order of 10^{-4}, *i.e.*, they are not numerically zero, but compared with the real part they become negligible. However, the imaginary parts may appear with incorrect sign, which indicates a violation of passivity. Especially for metamaterials, where the inclusions often are resonant and lossy, the NRW technique tends to give unphysical material parameters. This problem is discussed more extensively in [7].

However, the refractive index n is not affected by the Fabry–Pérot resonances remaining smooth over all frequencies. This allows us to fight the problem by demanding $\mu_{\text{eff}} = 1$ and solving the permittivity directly by $\epsilon_{\text{eff}} = n^2$. This modified retrieval yields smooth and physically reasonable estimates for ϵ_{eff} (see Fig. 7).

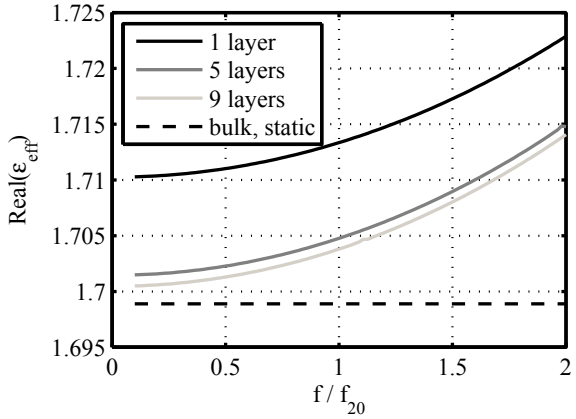

Fig. 7. The effective permittivity (real part) retrieved by $\epsilon_{\text{eff}} = n^2$ for different number of layers.

As a general observation, it can be seen that as the frequency increases, the obtained permittivity starts to notably deviate from the static reference. Also, the number of layers affects the permittivity. The increase of the number of layers makes the permittivity tend to the bulk value at the static limit. With only one layer, the retrieved permittivity is clearly higher.

V. FIELD AVERAGING BY INTEGRATION

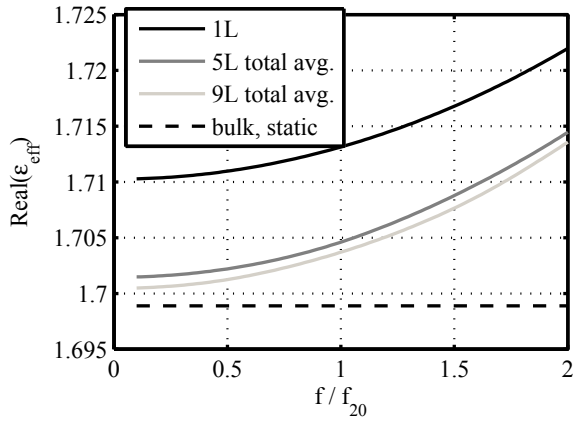

Fig. 8. The effective permittivity (real part) retrieved by f eld integration.

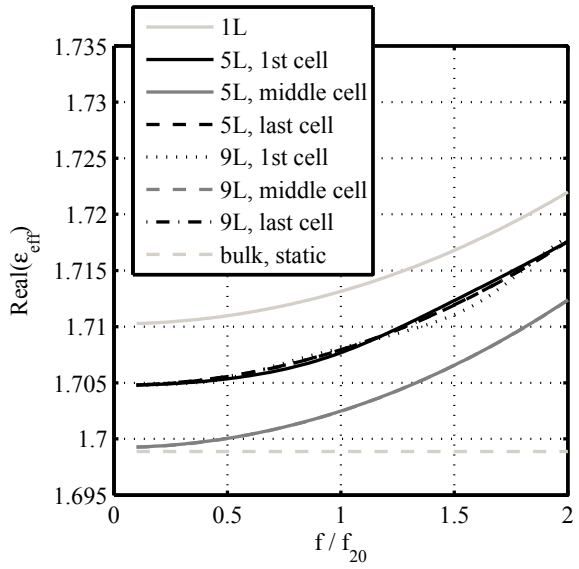

Fig. 9. The effective permittivity values retrieved by f eld integration in different unit cells.

Whereas the previous method observed the material from the outside, another approach is to consider the constitutive relation within the material. In each individual point $\mathbf{D}(\mathbf{r}) = \epsilon(\mathbf{r})\mathbf{E}(\mathbf{r})$. Then, if averaged over the whole material, the relation between the displacement current $\mathbf{D}$ and the electric f eld $\mathbf{E}$ is def ned by the effective permittivity, $\langle \mathbf{D} \rangle = \epsilon_{\text{eff}} \epsilon_0 \langle \mathbf{E} \rangle$.

Field averaging is studied, for instance, in [16]. We, however, choose a very simple and straightforward procedure where the f elds are averaged by volume integration over each unit cell. Actually, due to the symmetry and linearly polarized normally incident plane wave excitation, one quarter of a cell is needed. The effective permittivity of a unit cell is obtained by

$$\epsilon_{\text{eff}} = \frac{\langle D_t \rangle}{\epsilon_0 \langle E_t \rangle} = \frac{\int D_t dV}{\epsilon_0 \int E_t dV}, \tag{7}$$

where subscript t refers to the component transverse to the wave propagation. Finally, for the whole slab, the permittivities of separate cells are averaged once more over all consecutive layers. Figure 8 presents the retrieved permittivities for different slabs.

This method allows us to investigate the permittivity separately in each cell. It turns out that there are only three different kinds of cells, as can be seen in Fig. 9. In a one-layered case, the unit cells do not have any neighboring cells around them. This situation yields the highest permittivity value. Another case are the layers on the boundary that have neighbors on one side and the third group are the cells inside the slabs with neighbors on both sides. All the interior cells give the same permittivity, although only the values of the midmost cells are plotted in Fig. 9. The boundary permittivity is higher than the interior permittivity. At the static limit, the interior permittivity tends to the bulk value given by static mixing formulas. The values of the boundary and interior permittivities do not depend on the number of layers.

These results support the theory of boundary transition layers, which suggests that the effective model of the homogenized material should include separate boundary layers with permittivity different from the interior material [7]. This boundary permittivity becomes higher than the bulk value and the suff cient thickness of the transition layer would be one unit cell, which is in agreement with previous literature [17, 18]. Also, [18] suggests a modif cation to the Maxwell Garnett formula for computing the static transverse boundary permittivity. Unfortunately, the volume fraction $p = 1/4$ considered in our study is too large for the MG formula, Eq. (2), to give accurate results. Nonetheless, the predicted difference between the boundary and the bulk permittivities becomes 0.006, which quantitatively agrees with the difference seen in Fig. 9 very well.

VI. COMPARISON BETWEEN THE METHODS

Figure 10 presents the effective permittivities retrieved by different methods. The original S-parameter method (NRW) is suffering from the

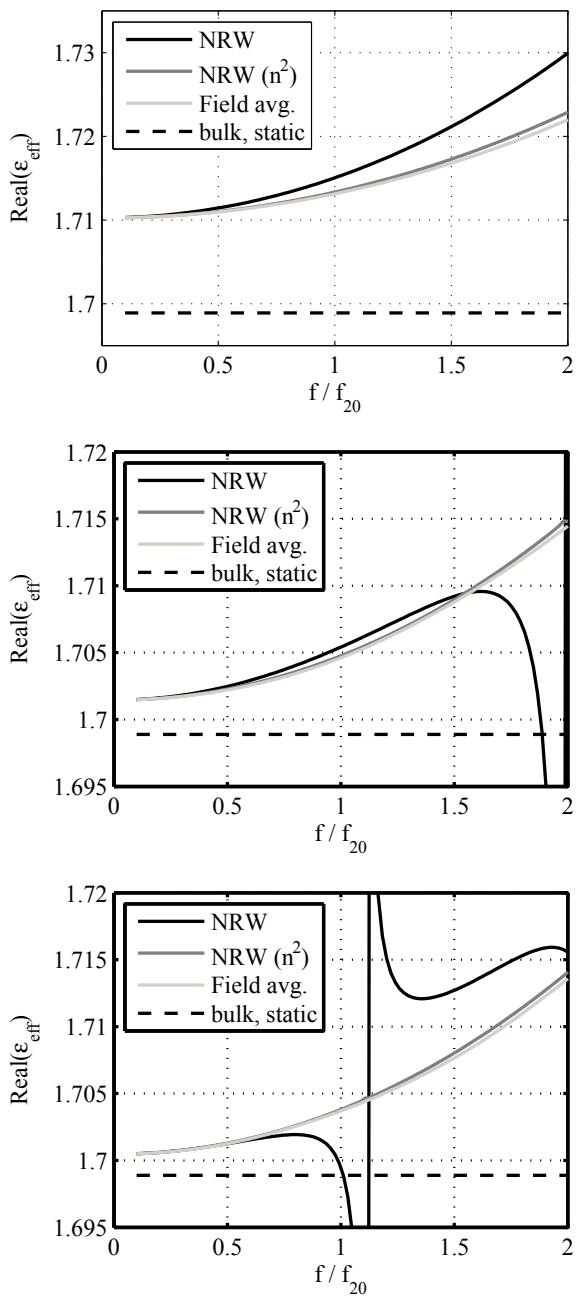

Fig. 10. Comparison of the retrieval methods for a slab with 1 layer (top), 5 layers (middle), and 9 layers (bottom).

Fabry–Pérot resonances that also contaminate the retrieval results. Increasing the slab thickess makes the resonances shift lower in frequency. Despite the nonmagnetic nature of the original composite, the method also yields effective permeability μ_{eff}, which, with increasing frequency, starts to deviate from unity. Moreover, the retrieved parameters show unphysical behavior. Instead, assuming $\mu_{\text{eff}} = 1$ and computing ϵ_{eff} as the square of the refractive index n gives smooth results that are very similar to the ones given by the f eld averaging method. In the static limit, all methods tend to the same value. This value depends on the number of layers.

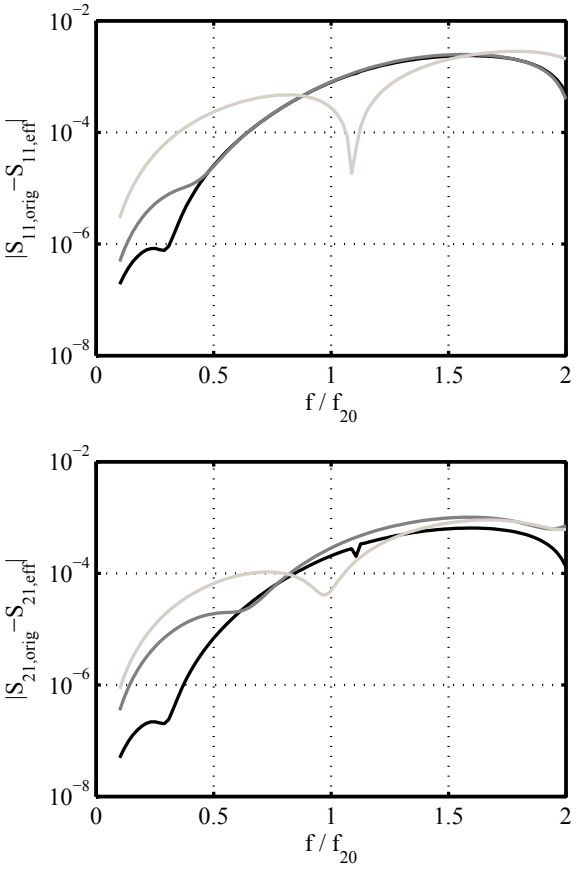

Fig. 11. The absolute error between the S_{11} (top) and S_{21} (bottom) of the original 9-layered composite slab and the homogenized model. The used models: modif ed NRW with $\epsilon_{\text{eff}} = n^2$ (black), f eld averaging method (grey), and boundary transition layer model (light grey).

Altogether, based on two different methods, we have four ways to build the homogenized model for the composite slab: the original NRW approach with both $\epsilon_{\text{eff}} = n/z$ and $\mu_{\text{eff}} = nz$, the modif ed NRW with $\mu_{\text{eff}} = 1$ and $\epsilon_{\text{eff}} = n^2$, the f eld averaging method with homogeneous ϵ_{eff} for the whole slab, and the piecewise homogeneous model with separate transition layers with different permittivity. If the effective model is correct, it should also have the same scattering properties as the original composite. It turns out

that the other models but the original NRW do not exactly reproduce the original S-parameters.

Figure 11 presents the absolute differences between the simulated S-parameters of the original slab and the different homogenized models in the case of 9 layers. The errors are anyway relatively small, yet not numerically negligible, and they start to grow with increasing frequency. Also, there are no significant differences between the models.

VII. CONCLUSIONS AND DISCUSSION

Two different computational methods for homogenization of thin composite slabs were considered and compared, namely the S-parameter (NRW) method and the field averaging method. Both techniques also offered modified ways to model the effective permittivity, in S-parameter method by the non-magnetic material assumption and in the averaging method by using the boundary transition layers. The original NRW method yielded both ϵ_{eff} and μ_{eff} resonant and unphysical violating the principles of causality and passivity. When $\mu_{\text{eff}} = 1$ was assumed and the permittivity computed as $\epsilon_{\text{eff}} = n^2$, the result was smooth and similar to the one obtained by field averaging. The field averaging method, however, suggested a piecewise homogeneous model where the boundary layers are modeled separately using slightly higher permittivity.

When the frequency, *i.e.*, the electrical size of the unit cells, was increased, neither of the methods proved superior. However, important fundamental conclusions can be drawn.

Firstly, for homogenization purposes, the electrical size of the unit cell should be very small. As seen in Fig. 11, with increasing frequency, the homogenized models fail to produce the same scattering parameters with the original composite slab. Our results suggest that the unit cell size $a \approx \lambda/20$, where λ is the reduced wavelength inside the material, is a limit, after which the material cannot safely be considered perfectly homogeneous. Futhermore, from Figs. 5–10 we see that the cells must be extremely small, $a \approx \lambda/100$, before the (quasi)static state is reached. Naturally, in practical experiments a certain tolerance for an acceptable error must be defined. In our case, the absolute differences are small numbers and in many cases they may seem negligible. The focus of this paper is, however, to find fundamental limitations of material homogenization approach in general, and to discuss the characteristics of different homogenization methods.

Secondly, the value of material parameters should not depend on the amount of the material. A sufficient amount of layers is required for the slab to behave as a bulk material. From Fig. 10, it is seen that not even the 9-layered slab exactly converges to the bulk value. This is explained by the effect of the boundary layers, which have higher permittivity than the interior layers increasing the total average permittivity of the slab. That is, a homogeneous material should include enough layers in order to make the boundary effect negligible. A slab with only one or two layers cannot be considered a material at all.

Moreover, considering the applicability of the original NRW method, we see from Fig. 10 that we must operate with frequencies where the electrical thickness of the slab remains below $\lambda/2$. However, at the same time, the thickness must be large enough in terms of unit cell layers for the slab to resemble bulk material. These two limitations roughly imply that for reliable usage of the NRW technique, the slab thickness should be at least 10 layers or more, which means that the maximum unit cell size should be of the order of $\lambda/50$.

Furthermore, the current study is still restricted focusing only on dielectric composite and the normal incidence. By considering oblique incidence from different angles, possible effects of anisotropy and spatial dispersion could be studied. Also, assuming the composite non-magnetic, non-dispersive, and lossless is quite an idealization. Moreover, especially in metamaterials research, the inclusions are assumed strongly dispersive and resonant having also negative material parameter values. In these more complex cases, extra care must be taken that the assumption of effective homogeneity holds. Therefore, futher fundamental study is needed.

ACKNOWLEDGMENT

This study was supported in part by the Academy of Finland. The work of H. Kettunen was also supported by the (Finnish) Graduate School in Electronics, Telecommunications and Automation (GETA).

REFERENCES

[1] G. W. Milton, *The Theory of Composites*. Cambridge Univ. Press, Cambridge, 2002.

[2] C. Brosseau, “Modelling and Simulation of Di-

electric Heterostructures: A Physical Survey from an Historical Perspective," *J. Phys. D: Appl. Phys*, vol. 39, no. 7, pp. 1277–1294, 2006.

[3] D. S. Killips, *Composite Material Design and Characterization for RF Applications*. Ph.D. Thesis, Michigan State University, 2007.

[4] N. Engheta and R. W. Ziolkowski, eds., *Metamaterials: Physics and Engineering Explorations*. Wiley-Interscience, Hoboken, NJ, 2006.

[5] A. K. Sarychev and V. M. Shalaev, *Electrodynamics of Metamaterials*. World Scientif c, Singapore, 2007.

[6] C. Menzel, T. Paul, C. Rockstuhl, T. Pertsch, S. Tretyakov, and F. Lederer, "Validity of Effective Material Parameters for Optical Fishnet metamaterials," *Phys. Rev. B*, vol. 81, no. 3, pp. 035320:1–5, 2010.

[7] C. R. Simovski, "Material Parameters of Metamaterials (a review)," *Opt. Spectrosc.*, vol. 107, no. 5, pp. 726–753, 2009.

[8] L. Bennett, W. E. Hutchcraft, R. K. Gordon, E. Lackey, J. G. Vaughan, and R. Averill, "Extracting the Electrical Properties of Polymeric Composite Materials through Circuit Simulation and Optimization," *Appl. Comput. Electromagnetics Soc. J.*, vol. 23, no. 1, pp. 84–89, 2008.

[9] J. Qi, H. Kettunen, H. Wallén, and A. Sihvola, "Quasi-Dynamic Homogenization of Geometrically Simple Dielectric Composites," *Appl. Comput. Electromagnetics Soc. J.*, vol. 25, no. 12, pp. 1036–1045, 2010.

[10] A. Sihvola, *Electromagnetic Mixing Formulas and Applications*. IEE, London, 1999.

[11] R. C. McPhedran and D. R. McKenzie, "The Conductivity of Lattices of Spheres I. The Simple Cubic Lattice," *Proc. R. Soc. Lond. A*, vol. 359, pp. 45–63, 1978.

[12] A. M. Nicolson and G. F. Ross, "Measurement of the Intrinsic Properties of Materials by Time-Domain Techniques," *IEEE Trans. Inst. Meas.*, vol. IM-19, no. 4, pp. 377–382, 1970.

[13] W. B. Weir, "Automatic Measurement of Complex Dielectric Constant and Permeability at Microwave Frequencies," *Proc. IEEE*, vol. 62, no. 1, pp. 33–36, 1974.

[14] D. R. Smith, S. Schultz, P. Markoš, and C. M. Soukoulis, "Determination of Effective Permittivity and Permeability of Metamaterials from Ref ection and Transmission Coeff cients," *Phys. Rev. B*, vol. 65, no. 19, pp. 195104:1–5, 2002.

[15] X. Chen, T. M. Grzegorczyk, B.-I. Wu, J. Pacheco, Jr., and J. A. Kong, "Robust Method to Retrieve the Constitutive Effective Parameters of Metamaterials," *Phys. Rev. E*, vol. 70, no. 1, pp. 016608:1–7, 2004.

[16] D. R. Smith and J. B. Pendry, "Homogenization of Metamaterials by Field Averaging," *J. Opt. Soc. Am. B*, vol. 23, no. 3, pp. 391–403, 2006.

[17] G. D. Mahan and G. Obermair, "Polaritons at Surfaces," *Phys. Rev.*, vol. 183, no. 3, pp. 834–841, 1969.

[18] C. R. Simovski, S. A. Tretyakov, A. H. Sihvola, and M. M. Popov, "On the Surface Effect in Thin Molecular or Composite Layer," *Eur. Phys. J. AP*, vol. 9, no. 3, pp. 195–204, 2000.

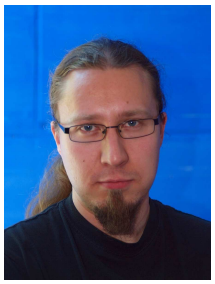

Henrik Kettunen was born in Orimattila, Finland, in 1980. He received the M.Sc. (Tech.) and Lic.Sc. (Tech) degrees in Electrical Engineering from the Helsinki University of Technology (TKK), Espoo, Finland, in 2006 and 2009, respectively. He is currently working toward the D.Sc. (Tech.) degree in Electrical Engineering at Aalto University School of Science and Technology, Finland. His research interests include electromagnetic modeling of complex materials.

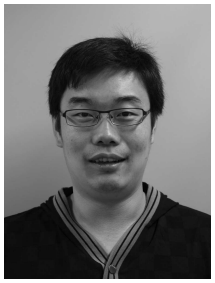

Jiaran Qi was born in Harbin, China, in 1981. He received the B.E. (Communication Engineering) and M.E. degrees (Electromagnetics and Microwave Technology) from Harbin Institute of Technology, China, in 2004 and 2006, respectively. He is currently working toward the D.Sc. degree at Department of Radio Science and Engineering in Aalto University School of Science and Technology, Finland. His current research interests include electromagnetic wave interaction with complex media and modeling of metamaterials.

Henrik Wallén was born in 1975 in Helsinki, Finland. He received the M.Sc. (Tech.) and D.Sc. (Tech.) degrees in Electrical Engineering in 2000 and 2006 from the Helsinki University of Technology (which is now part of the Aalto University). He is currently working as a Postdoctoral Researcher at the Aalto University School of Science and Technology, Department of Radio Science and Engineering in Espoo, Finland. He is Secretary of the Finnish National Committee of URSI (International Union of Radio Science). His research interests include electromagnetic theory, modeling of complex materials, and computational electromagnetics.

Ari Sihvola was born on October 6th, 1957, in Valkeala, Finland. He received the degrees of Diploma Engineer in 1981, Licentiate of Technology in 1984, and Doctor of Technology in 1987, all in Electrical Engineering, from the Helsinki University of Technology (TKK), Finland. Besides working for TKK and the Academy of Finland, he was visiting engineer in the Research Laboratory of Electronics of the Massachusetts Institute of Technology, Cambridge, in 1985–1986, and in 1990–1991, he worked as a visiting scientist at the Pennsylvania State University, State College. In 1996, he was visiting scientist at the Lund University, Sweden, and for the academic year 2000–01, he was visiting professor at the Electromagnetics and Acoustics Laboratory of the Swiss Federal Institute of Technology, Lausanne. In the Summer of 2008, he was visiting professor at the University of Paris XI, France. Ari Sihvola is professor of electromagnetics in Aalto University School of Science and Technology (before 2010 Helsinki University of Technology) with interest in electromagnetic theory, complex media, materials modelling, remote sensing, and radar applications. He is Chairman of the Finnish National Committee of URSI (International Union of Radio Science) and Fellow of IEEE. He was awarded the f ve-year Finnish Academy Professor position starting August 2005. Starting January 2008, he is director of the Graduate School of Electronics, Telecommunications, and Automation (GETA).

Hardware Accelerated Design of Millimeter Wave Antireflective Surfaces: A Comparison of Field-Programmable Gate Array (FPGA) and Graphics Processing Unit (GPU) Implementations

Ozlem Kilic[1], Miaoqing Huang[2], Charles Conner[1], and Mark S. Mirotznik[3]

[1]Department of Electrical Engineering and Computer Science
The Catholic University of America, Washington, DC 20064, USA
{kilic,connerc}@cua.edu

[2]Department of Computer Science and Computer Engineering
University of Arkansas, Fayetteville, AR 72701, USA
mqhuang@uark.edu

[3]Department of Electrical and Computer Engineering
University of Delaware, Newark, DE 19716, USA
mirotzni@ece.udel.edu

***Abstract*—**Engineered materials that demonstrate a specific response to electromagnetic energy incident on them in antenna and radio frequency component design applications are in high demand due to both military and commercial needs. The design of such engineered materials typically requires numerically intensive computations to simulate their behavior as they may have electrically small features on a large area or often the overall system performance is required, which means modeling the entire integrated system. Furthermore, to achieve an optimal performance these simulations need to be run many times until a desired solution is achieved, presenting a major hindrance in arriving at a feasible solution in a reasonable amount of time. One example of such applications is the design of antireflective (AR) surfaces at millimeter wave frequencies, which often involves sub-wavelength gratings in an electrically large multilayer structure. This paper investigates the use of field-programmable gate arrays (FPGAs) and graphics processing units (GPUs) as coprocessors to the CPU in order to expedite the computation time. Preliminary results show that the hardware implementation (100 MHz) on Xilinx Virtex4LX200 FPGA is able to outperform a single-thread software implementation on Intel Itanium 2 processor (1.66 GHz) by 20 folds. However, the performance of the FPGA implementation lags behind the single-thread implementation on a modern Xeon (2.26 GHz) by 3.6×. On the other hand, modern GPUs demonstrate an evident advantage over both CPU and FPGA by achieving 20× speedup than the Xeon processor.

***Index Terms*—**Antireflective Surface, Engineered Materials, FPGA, GPU, Parallel Computing, Reconfigurable Programming, High-Performance Computing.

I. INTRODUCTION

The design of engineered materials that demonstrate a specific response to incident electromagnetic energy often requires the use of periodic structures with dimensions that are much smaller than the wavelength for electrically large structures (i.e., overall size of many wavelengths). As a result, the accurate and fast modeling of these large scale structures with fine features often becomes a major challenge. The challenge is even bigger when these models have to be run iteratively to identify an optimal solution. Recently, hardware accelerated computing has been gaining momentum due to its applicability to parallel computing while using a fraction of the power requirement of the conventional microprocessors and requiring much less cost in comparison to supercomputers.

The objective of this paper is two folds: (i) investigate the use of FPGAs and GPUs as coprocessors to CPU in electromagnetic simulations, (ii) utilize the hardware acceleration in simulating complex devices and optimizing their performance. These objectives will be achieved in the context of the design of antireflective (AR) surfaces with sub-wavelength gratings.

A common approach to the design of AR surfaces in optical regimes is to coat the surface with multiple layers of thin films with specific dielectric properties that result in the desired performance. This approach is not practical at millimeter wave frequencies as there is limited availability of dielectric materials with the desired material properties. For this purpose, alternative techniques using gratings in the substrate can be used to simulate the same effect [1]. The gratings in essence modify the effective dielectric property of each layer. As a first order approximation, an effective permittivity for each layer can be computed using the effective media theory [2]. However, this approach is only suitable

Table 1: Comparison between FPGA and GPU

Criterion		FPGA	GPU
Power Consumption		Low (Virtex4LX200: ~10 W)	High (GTX 480: 450 W)
Cost		High (Virtex4LX200: ~$6,000)	Low (GTX 480: $500)
Programming	Learning Curve	Long	Short
	Difficulty	High (Use hardware discription language)	Low (Use high level language)
	Flexibility	High	Low
	Portability	Low	High
Floating-Point Performance		Low	High

for gratings with dimensions that are much smaller than the incident wavelength. For the case of sub-wavelength gratings (i.e., resonant regime) considered in this paper, a more precise approach is required as the assumptions of the effective media theory are no longer valid.

This paper uses the rigorous coupled wave (RCW) algorithm, which employs an eigenmode approach as described in [3], to model the AR surface created with sub-wavelength gratings. RCW algorithm applies to structures with periodic gratings. The electric field and the periodic permittivity values inside the structure are expanded into a Fourier series in spatial harmonics, resulting in a matrix of coupled wave equations. With this approach, the field inside the medium is expanded in terms of the space harmonics in the periodic structure and phase matched to the fields outside the grating. The fields can be treated as waveguide modes in the grating region, and the total field is expressed as a sum of all possible modes.

The remaining part of the paper is organized as follows. Section II describes the underlying principles of hardware acceleration and presents the features of FPGA and GPU with particular attention to the systems used in this implementation. The details of the RCW algorithm are provided and its numerically intensive components are identified in Section III. Section IV describes the implementation of the RCW algorithm on two different platforms: a state-of-the-art reconfigurable computer, SGI Altix RASC RC100 [4], and the NVIDIA GPUs (i.e., Tesla C1060 and GeForce GTX480). The platform specifications for the hardware implementation and the interaction between the CPU and the two hardware platforms are also presented in this section. Significant performance improvement has been achieved on both FPGA and GPU platforms compared with the software implementation on Intel Itanium 2 and Xeon E5520 processors. Finally, the conclusion remarks are given in Section VI.

II. HARDWARE ACCELERATION ON FPGA AND GPU

Parallelism and pipelining are in the essence of hardware accelerated computing. A more conventional way of hardware acceleration based on von-Neuman architecture, where instructions and data are stored in the same memory, is typically achieved by the use of multiple processors in a system. In this approach, instruction stream programming can be used as in any traditional computer. An example of such a system is the Beowulf cluster [5]. As an alternative, this paper focuses on a different kind of hardware acceleration, where a coprocessor is used to support the CPU for specific tasks in an algorithm. Traditional von-Neuman architectures tend to create bottlenecks between the CPU and the main memory. The use of a dedicated coprocessor with its own memory can accelerate numerically intensive computations. One of the early uses of such coprocessors is the digital signal processor (DSP), which is a highly specialized form of a microprocessor. While the use of DSPs was universal for hardware acceleration in its early stages, the growing need for flexibility for many computationally intensive applications outstripped the functionalities offered by these chips. As a result, FPGAs, which are a form of highly configurable hardware, began entering the market. FPGAs contain programmable logic components called "logic blocks", and a hierarchy of reconfigurable interconnects that allow the blocks to be connected together to perform custom computation. With the abundance of available transistors, modern FPGAs are capable of carrying out big scientific applications. Thousands of performance speedup has been observed on reconfigurable computers [6].

While FPGAs are highly reconfigurable and energy efficient, there is a prize for the flexibility offered by these platforms, i.e., the difficulty in hardware implementation. Typically, hardware description languages, such as Verilog and VHDL, are required to program the FPGAs in order to achieve desirable performance speedup.

Recently, another platform, i.e., graphics processing unit, has been gaining popularity due to their relatively easier learning curve. GPU was presented as early as in 1989 as a stream computing engine [7]. Modern GPUs from both NVIDIA and AMD consist of hundreds of stream processing units and are capable of achieving remarkable processing parallelism. Both companies provide SDK to facilitate the end user use high level languages (e.g., C language) to program the GPUs, therefore significantly lowering the programming difficulty.

FPGAs and GPUs, have demonstrated the ability to speed up a wide range of applications from image processing to encryption, as demonstrated in previous work [8]–[12]. Each technology has its advantage and disadvantage, as listed in Table 1. In general, GPU provides the ease of use and higher parallelism. On the other hand, FPGA consumes much less power, has better programming flexibility, and provides deep pipelining, which is very useful for many applications.

III. RIGOROUS COUPLED WAVE ALGORITHM

The rigorous coupled wave (RCW) algorithm applies to diffraction problems from multiple layers with periodic gratings. It is based on an extension of enhanced transmittance

$$\begin{bmatrix} \partial^2 S_{l,y}/\partial z'^2 \\ \partial^2 S_{l,x}/\partial z'^2 \end{bmatrix} = \Omega_l \begin{bmatrix} S_{l,y} \\ S_{l,x} \end{bmatrix}, \tag{1a}$$

$$\Omega_l = \begin{bmatrix} k_x^2 + D[\alpha\varepsilon_l + (1-\alpha)A_l^{-1}] & k_y\{\varepsilon_l^{-1}k_x[\alpha A_l^{-1} + (1-\alpha)\varepsilon_l] - k_x\} \\ k_x\{\varepsilon_l^{-1}k_y[\alpha\varepsilon_l + (1-\alpha)A_l^{-1}] - k_y\} & k_y^2 + B[\alpha A_l^{-1} + (1-\alpha)\varepsilon_l] \end{bmatrix}. \tag{1b}$$

$$\underset{A}{\begin{bmatrix} \times & \times & \times & \times & \times \\ \times & \times & \times & \times & \times \\ \times & \times & \times & \times & \times \\ \times & \times & \times & \times & \times \\ \times & \times & \times & \times & \times \end{bmatrix}} \xrightarrow{\text{Phase 1}} \underset{\text{Hessenberg } H}{\begin{bmatrix} \times & \times & \times & \times & \times \\ \times & \times & \times & \times & \times \\ 0 & \times & \times & \times & \times \\ 0 & 0 & \times & \times & \times \\ 0 & 0 & 0 & \times & \times \end{bmatrix}} \xrightarrow{\text{Phase 2}} \underset{\text{Triangular } S}{\begin{bmatrix} \otimes & \times & \times & \times & \times \\ 0 & \otimes & \times & \times & \times \\ 0 & 0 & \otimes & \times & \times \\ 0 & 0 & 0 & \otimes & \times \\ 0 & 0 & 0 & 0 & \otimes \end{bmatrix}}. \tag{2}$$

matrix approach in [13] and adopts Lalanne's improved eigenvalue formalism [14]. A detailed discussion on the RCW algorithm can be found in these references. We provide a brief overview in this section in order to describe our motivations for the hardware implementation.

The stacked multiple layer in RCW algorithm can consist of any number of gratings. However, all gratings must be periodic with the same periodicity along a given direction on the plane. The periodicity results in a spatially periodic permittivity (and inverse permittivity) within each layer and can be represented as a Fourier series expansion, as follows.

$$\varepsilon_l(x,y) = \sum_{g,h} \varepsilon_{l,gh} \exp\left(j\frac{2\pi gx}{\Lambda_x} + j\frac{2\pi hy}{\Lambda_y}\right), \tag{3a}$$

$$\varepsilon_l^{-1}(x,y) = \sum_{g,h} A_{l,gh} \exp\left(j\frac{2\pi gx}{\Lambda_x} + j\frac{2\pi hy}{\Lambda_y}\right). \tag{3b}$$

where $\varepsilon_{l,gh}$ and $A_{l,gh}$ are the Fourier coefficients for the lth layer in the stack for the permittivity and inverse permittivity respectively. The electric field inside the layers can similarly be expressed as a Fourier series in terms of spatial harmonics. Maxwell's equations for the layered structure can be written in terms of the tangential components of the electric and magnetic fields, resulting in a coupled equation set in (1), where S_l represents the amplitudes of the spatial harmonics of the electric field in the lth layer, with subscripts x and y denoting the directions of periodicity in the plane of the stack. The parameters B and D in (1b) are matrices given as

$$B = k_x\varepsilon_l^{-1}k_x - I, \tag{4a}$$

$$D = k_y\varepsilon_l^{-1}k_y - I. \tag{4b}$$

The k_x and k_y in (1b) and (4) are diagonal matrices formed by k_{x_m} and k_{y_n} as shown in (5), in which k_0 is the free space wave number.

$$k_x = \frac{k_{x_m}}{k_0}, \tag{5a}$$

$$k_y = \frac{k_{y_n}}{k_0}. \tag{5b}$$

k_{x_m} and k_{y_n} are the wave vector components along x and y, respectively. They are computed from phase matching and Floquet conditions as (6).

$$k_{x_m} = k_0\left(n_1\sin\theta\cos\varphi - m\left(\frac{\lambda_0}{\Lambda_x}\right)\right), \tag{6a}$$

$$k_{y_n} = k_0\left(n_1\sin\theta\sin\varphi - n\left(\frac{\lambda_0}{\Lambda_y}\right)\right). \tag{6b}$$

Λ_x and Λ_y in (3) and (6) represent the periodicity of the gratings along x and y respectively. α in (1b) is a grating geometry dependent parameter, which is a real positive number between $[0, 1]$ as introduced in [14].

Therefore, the coupled wave equation can be solved by finding the eigenvalues of the matrix Ω_l, which is a function of the stack properties. The rank of this matrix is $M \times N$, where M and N are the number of spatial harmonics retained along the two dimensions of periodicity in the plane of stacked layers. Ideally an infinite number of them are needed for an exact solution but truncation with minimal error is possible. Despite this truncation, the rank can be in the order of magnitude of 400 or more for a typical application of AR surface design. Hence, the most numerically intensive component of the RCW algorithm is this eigenvalue computation. The hardware platforms will be used to implement the eigenvalue computations of the RCW algorithm to achieve acceleration.

A. QR eigenvalue algorithm

Given a square matrix $A \in \mathbb{C}^{n\times n}$, an eigenvalue λ and its associated eigenvector $\mathbf{v}$ are, by definition, a pair obeying the relation $A\mathbf{v} = \lambda\mathbf{v}$. Equivalently, $(A - \lambda I)\mathbf{v} = 0$ (where I is the identity matrix), implying $\det(A - \lambda I) = 0$. This determinant can be expanded into a polynomial in λ, known as the *characteristic polynomial* of A. One common method for determining the eigenvalues of a small matrix is by finding the roots of its characteristic polynomial. However, a general polynomial of order $n > 4$ cannot be solved by a finite sequence of arithmetic operations and radicals. Therefore, many numerical iterative algorithms have been proposed [15] to solve the eigenvalue problem of high-rank square matrices, such as power method, inverse iteration, Jacobi method, etc. Among these, the shifted Hessenberg QR algorithm [16]–[18] is accepted as a practical solution and adopted in most applications to deal with general square matrices.

There are two phases in the practical QR algorithm, as described in (2). In the first phase, the original matrix A is re-

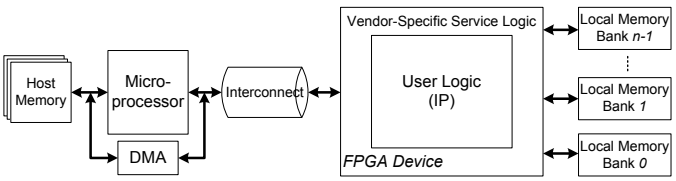

(a) General architecture of a reconfigurable computer

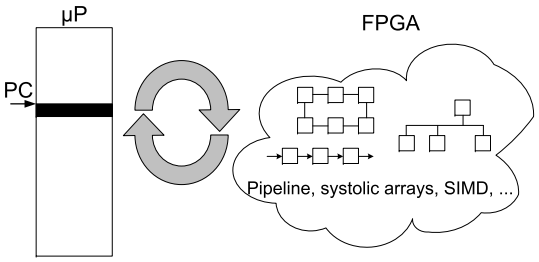

(b) Execution model

Fig. 1. Using FPGAs as coprocessors in general-purpose computing.

duced to the upper Hessenberg form H using the Householder transformation [19]. The second phase involves applying the implicit QR iteration with shifts on the unreduced Hessenberg matrix H until it converges to a triangular matrix, i.e., the Schur form S. The eigenvalues of a triangular matrix are listed on the diagonal, i.e., the $\otimes$s in (2), and the eigenvalue problem is solved once this form is achieved. If the corresponding eigenvectors are required, they can be calculated using Gaussian elimination and back substitution after the eigenvalues are available.

IV. HARDWARE IMPLEMENTATION OF THE RCW ALGORITHM

Both hardware platforms (e.g., FPGA and GPU) will be used as coprocessors to the CPU to accelerate the most numerically intensive part of the RCW algorithm, which is the eigenvalue calculation for the large matrices required in the RCWA design. Promising results are demonstrated to prove the efficiency of the hardware implementation compared with the software implementation of the same algorithm in C. The acceleration in computation time allows for the design and optimization of complex AR surfaces as numerous iterations can be run rapidly on hardware coprocessors.

A. Implementation on Altix RASC RC100 reconfigurable computer

Reconfigurable computers (RCs) are traditional computers extended with coprocessors based on reconfigurable hardware like FPGAs. These enhanced systems are capable of providing significant performance improvement for applications in many scientific and engineering domains, such as the electromagnetics [20], [21]. Due to the limited size of the internal block RAM memory, multiple SRAM modules are generally connected to the hardware coprocessor for data storage, such as the example shown in Figure 1(a).

The implementation of an application on a reconfigurable computer consists of a hardware part and a software part. The implementation on the hardware part requires the use of either hardware description languages (e.g., VHDL, Verilog) or high level languages, such as Impulse-C [22] or Mitrion-C [23], to carry out the design in hardware. Multiple techniques, e.g., pipelining and single instruction multiple data (SIMD), can be applied to take advantage of the hardware acceleration. Multiple dependent tasks in an application can form a pipeline so that the output of a producer can be forwarded to the input of a consumer directly. Take the circuit in Figure 3(a) as one example, multiple primitive operators form a pipeline to accomplish an advanced operation. Another typical technique, SIMD as shown in Figure 3(c), is to instantiate multiple identical processing elements (PEs) so that multiple data items can be processed in parallel. The theoretical performance of N identical PEs is N times of a single PE.

Since the hardware implementation depends on the available resources on the FPGA device (e.g., memory, built-in multipliers, slices), it might be necessary to distribute the hardware part into multiple FPGA configurations, each of which is called a *bitstream*. Once the bitstreams are available, they can be integrated into the software part, which is executed on the CPU. From the point of view of a software programmer, a bitstream can be treated as a software subroutine during the integration process in spite of the fact that the functionality is realized in hardware, as shown in Figure 1(b). The integration process always involves the use of vendor application programming interfaces (APIs).

In the following text, the numerically intensive part of the RCW algorithm, i.e., the eigenvalue solver, is described in terms of the mathematical approach used for the implementation. This discussion is followed by the details of the implementation of the eigenvalue algorithm on the Altix RASC RC100 reconfigurable computer along with a description of the system specifications and architecture of the platform.

1) The FPGA Platform: SGI's Altix RASC RC100 reconfigurable computer is a blade-based heterogeneous supercomputer in which NUMAlink™4 interconnect is used to connect different types of computing blades, as shown in Figure 2(a). Each blade itself is a homogeneous node consisting of the same type of processors, e.g., the CPU or the FPGA coprocessors. The Altix 450 at The Catholic University of America includes two CPU blades and one FPGA blade. The CPU used in the system is Intel Itanium 2 (1.66 GHz). The detailed architecture of a RASC RC100 FPGA blade is shown in Figure 2(b). There are two FPGA devices on a single RASC blade. Each FPGA device, Xilinx Virtex-4LX200, is equipped with 5 banks of SRAM for local data storage. The size of each SRAM bank is 8 MB. Every bank has separate 64-bit read and write ports directly connected to the FPGA device. Besides the local memory, each FPGA device is capable of communicating with CPU blades through

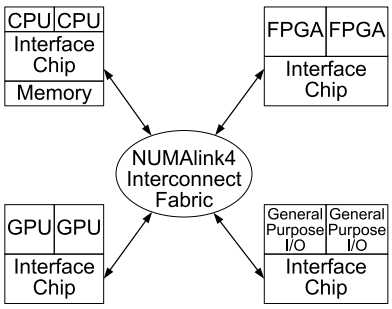

(a) Multi-paradigm computing

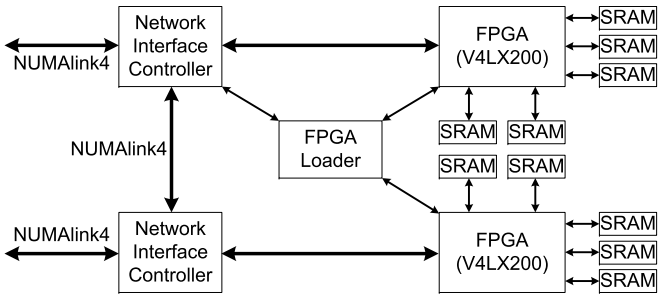

(b) RASC RC100 FPGA blade architecture

Fig. 2. Altix RASC RC100 reconfigurable computer.

NUMAlink™4 interconnect, achieving a theoretical 3.2 GB/s on both directions at the same time. Since the two FPGA devices have their separate network interface controller, their communication with other components in the RASC system is independent to each other. However, there is no direct communication channel between the two FPGA device on the same board. This limitation prevents an application from being implemented on two devices, i.e., part of an application on one device and part of the same application on the other device. In other words, the hardware part of an application can be only implemented on a single FPGA device.

There are several factors that can limit the problem size an application can deal with when it (or part of it) is implemented on FPGA device. The first one is the number of basic lookup tables (LUTs) or combined as slices on Xilinx FPGAs. The bigger an application is, the more hardware resource its implementation is going to take. The second one is the number of built-in multipliers. Many scientific and engineering applications involve the double precision floating-point operations, particularly multiplications. Basic LUTs can be used to construct double precision multipliers. However, a more economic way is to use the built-in multipliers so that LUTs can be used for other part of the application. The third limiting factor is the size and the bandwidth of the off-chip memory. The size of the memory will decide how much data (including source, intermediate and result data) can be stored. The bandwidth of the memory will decide the data processing parallelism the logic can achieve. In this work, it is mainly the

Algorithm 1: Hessenberg Reduction (Vector-based)

Input: A square complex matrix A with rank n
Output: The reduced Hessenberg matrix H

1.1 **for** k=*0* **to** $n-3$ **do**
1.2 $v_k = \textbf{House}(A_{k+1:n-1,k})$; /*Step 1: See Alg. 2*/
1.3 $A_{k+1:n-1,k:n-1} = A_{k+1:n-1,k:n-1} - 2v_k(v_k^* A_{k+1:n-1,k:n-1})$; /*Step 2: $P_k A_{k+1:n-1,k:n-1}$, $P_k = I - 2v_k v_k^*$*/
1.4 $A_{0:n-1,k+1:n-1} = A_{0:n-1,k+1:n-1} - 2(A_{0:n-1,k+1:n-1} v_k)v_k^*$; /*Step 3: $A_{0:n-1,k+1:n-1} P_k$*/

Algorithm 2: House(x)

Input: A complex vector x
Output: The Householder vector v

2.1 $\alpha = -e^{i\varphi}\|x\|$; /*$\varphi$ is the argument of x_1*/
2.2 $u = x - \alpha e_1 = x + e^{i\varphi}\|x\|e_1$; /*$e_1 = [1, 0, ..., 0]^T$*/
2.3 $v = \frac{u}{\|u\|}$;

size of the memory that decide the maximum problem size the application can deal with, as elaborated in the following text.

2) FPGA implementation of QR algorithm: The RCW algorithm in the most general sense creates a square matrix with complex entries. Both real part and imaginary part of a matrix entry are represented in double precision (64-bit) floating-point format. In the hardware implementation of QR eigenvalue algorithm on FPGA device, we combine the two physical local memory banks into a 128-bit wide logical memory bank so that each memory entry can store one complete matrix entry. Therefore, the real part and the imaginary part of a complex value can be accessed simultaneously.

As described in Section III-A, there are two phases in the QR algorithm. The first phase, i.e., the Hessenberg reduction, is completely implemented in one FPGA configuration. Part of the second phase in which the computation is close to the one in Hessenberg reduction is implemented in another separate FPGA configuration. Since the computation in both configurations is close, we focus on the description of Hessenberg reduction in this paper.

The first phase, Hessenberg reduction, is carried out by applying the Householder reflection for $n-2$ iterations (see Alg. 1), where n is the rank of the original matrix A. Each iteration comprises three steps, as shown in Table 2. Each step further includes multiple sub-steps. In our hardware design, Steps 1, 2, and 3 comprise 4, 3, and 3 sub-steps, respectively. All iterations, the steps in each iteration, and the sub-steps within every step have to be carried out sequentially due to the data dependency among them. More specifically, the 10 sub-steps are carried out in a sequence during the execution. The advantage of hardware implementation comes from the pipelined processing within each sub-step. For example, Step 1.1 involves multiplication, addition, accumulation, and square root operation to calculate the norm of a vector. In hardware

Table 2: Calculation breakdown of iteration k in Hessenberg reduction

Step	Sub-step	Calculation	Number of clock cycles for computation*	
1	1.1	$\|x\|$, $\|x_1\|$	$n-k-1$	$3k^2-9nk+6n^2-3n-2$
	1.2	$x_{1\_r}+\|x\|\cos\varphi$, $x_{1\_i}+\|x\|\sin\varphi$	1	
	1.3	$\|u\|$	$n-k-1$	
	1.4	$u/\|u\|$	$n-k-1$	
2	2.1	$m=v_k^* A_{k+1:n-1,k:n-1}$	$(n-k)(n-k-1)$	
	2.2	$N=v_k m$	$(n-k)(n-k-1)$	
	2.3	$A_{k+1:n-1,k:n-1}-2N$	$(n-k)(n-k-1)$	
3	3.1	$m'=A_{0:n-1,k+1:n-1}v_k$	$n(n-k-1)$	
	3.2	$N'=m'v_k^*$	$n(n-k-1)$	
	3.3	$A_{0:n-1,k+1:n-1}-2N'$	$n(n-k-1)$	

*Ignoring all latencies.

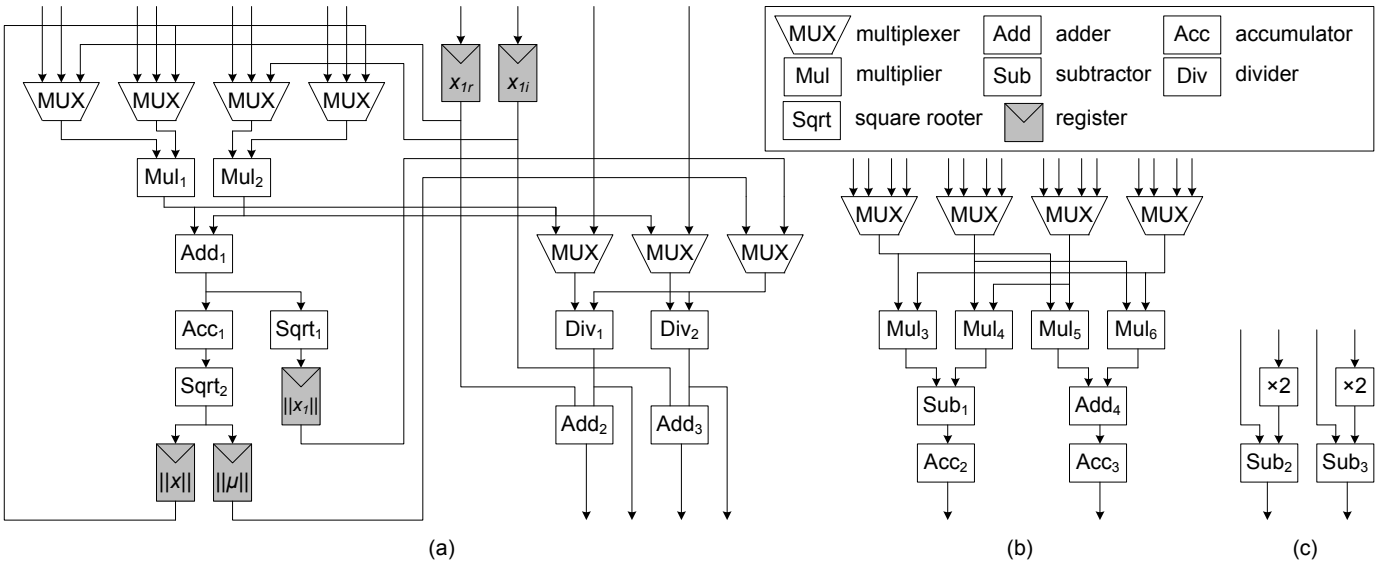

Fig. 3. The computing blocks in the hardware implementation: (a) the computing block used in Step 1; (b) the computing block used in Step 2.1, 2.2, 3.1, 3.2; (c) the computing block used in Step 2.3, 3.3. (*Note: (1) all inputs and outputs are connected to the local memory interface; (2) the control logic is not illustrated in the figure*).

implementation, these four operations are carried out in four operators, which are concatenated together to form a pipeline, as shown in Figure 3(a). These primitive operators are all fully pipelined in our design such that one new data item can be fed into the pipeline every clock cycle. Therefore, it will take roughly $n-k-1$ clock cycles to finish this sub-step (if we ignore all potential latencies). Table 2 lists the number of required clock cycles for each sub-step. By putting all iterations together, the total number of clock cycles required to reduce a matrix of rank n to its Hessenberg form can be computed as:

$$\sum_{k=0}^{n-3}(3k^2-9nk+6n^2-3n-2)=\frac{5}{2}n^3-\frac{9}{2}n-11. \quad (7)$$

The detailed hardware implementation of the computing blocks is illustrated in Figure 3. Since multiple steps have to be carried out sequentially, many basic computing units are re-used to reduce the resource cost. For example, the pipeline chain consisting of Mul_1, Mul_2, Add_1, Acc_1, and $Sqrt_2$ are re-used in Step 1.1 and Step 1.3 to compute $\|x\|$ and $\|\mu\|$, respectively. $\cos\varphi$ and $\sin\varphi$ are calculated on the fly by using division, i.e., $x_{1r}/\|x_1\|$ and $x_{1i}/\|x_1\|$. Therefore, the outputs of Step 1.2 correspond to the output of Add_2 (i.e., $x_{1r}+\|x\|\cdot x_{1r}/\|x_1\|$) and Add_3 (i.e., $x_{1i}+\|x\|\cdot x_{1i}/\|x_1\|$). The multiplication between matrix/vector and vector/vector in Step 2.1, 2.2, 3.1, and 3.2 is realized using the pipeline chain in Figure 3(b). Both the real part and the imaginary part of a complex entry are computed simultaneously. The control logic is not illustrated in Figure 3. It is mainly composed by three components, i.e., (1) a finite state machine whose statuses represent different steps and sub-steps, (2) the logic to generate correct read and write address for memory access, and (3) the logic to control the operations of the units in Figure 3.

The hardware implementation of Hessenberg reduction occupies 56,520 (63%) slices on the target FPGA device and runs at 100 MHz. The primitive operators, i.e., the double precision floating-point adder, multiplier, divider, are generated by using Xilinx CORE Generator. The accumulator is composed of adders and FIFOs. The hardware design is coded in Verilog, synthesized by Xilinx XST, placed and routed by Xilinx

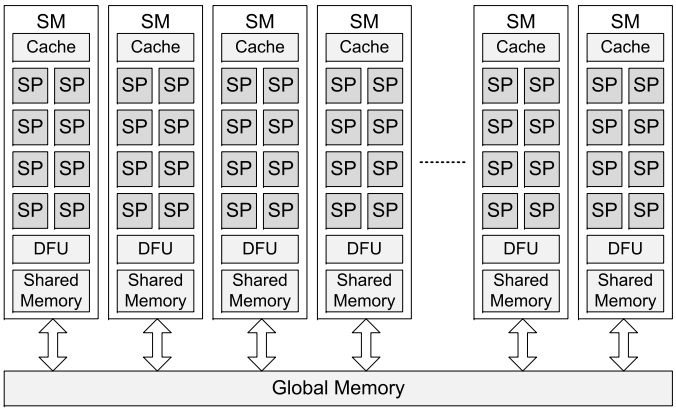

Fig. 4. The general architecture of an NVIDIA GT200 GPU (*SM: streaming multiprocessor, SP: streaming processor, DFU: double-precision floating-point unit*).

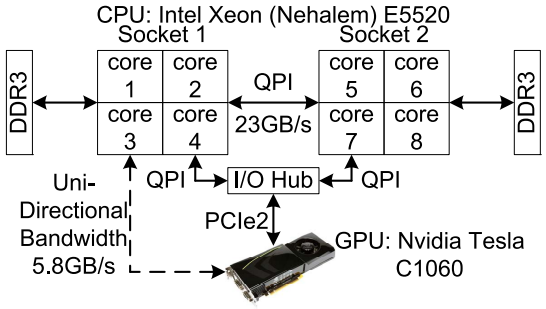

Fig. 5. The heterogeneous CPU-GPU board.

ISE 10.1. The operating frequency of the design is mainly limited by the control logic. The hardware design is capable of handling the matrix with a rank up to 480. The maximum size of the matrix is limited by the size of the off-chip memory in this case as a 480×480 complex matrix takes almost 8 MB to store its entries. The other off-chip memory is used to store the intermediate result in the execution. During the runtime, the rank of the object matrix is passed to the hardware design as a parameter through a register. Before the FPGA starts processing, the original matrix as well as its rank are transferred from the host to the FPGA. After the processing is finished, the upper Hessenberg matrix is transferred back to the host memory.

B. Implementation on NVIDIA GPUs

General-purpose computing on graphics processing units (GPGPU) is the technique of using GPUs to perform computation in applications traditionally handled by the microprocessors. GPUs are designed traditionally for graphics and thus are very restrictive in terms of operations and programming. Due to their nature, GPUs are only effective at tackling problems that can be solved using stream processing and the hardware can only be used in certain ways. More precisely, GPUs are efficient to process the independent elements belonging to a stream in a parallel fashion. Kernels are the functions that are applied to each element in the stream. Figure 4 illustrates a general architecture of an NVIDIA GT200 GPU consisting of many streaming processors (SPs).

We have implemented Alg. 1 on both NVIDIA Tesla C1060 and GeForce GTX 480 (Fermi) GPUs. The Tesla C1060 is installed on a dual-socket Intel Xeon workstation, as shown in Figure 5. The GTX 480 is installed on an Intel Core i7 workstation. On both workstations, GPU communicate with CPU through PCI Express 2 $\times$16 bus. Tesla C1060 (architecture code-named GT200) features 30 Streaming Multiprocessors, each of which is further composed of eight single precision floating-point CUDA streaming processors and one double precision floating-point unit, with 16KB on-chip storage called shared memory and 64KB of register windows for massive threading. The total 240 (single precision) + 30 (double precision) floating-point processors can achieve an observed peak performance of 78 GFLOPS for double precision operation. The Tesla GPU is equipped with 4 GB GDDR3 memory on board with the theoretical memory bandwidth of 102 GB/s. The uni-directional bandwidth of the PCI Express 2 bus on the platform is observed at 5.8 GB/s.

The latest GPU offered by NVIDIA is code-named as Fermi, which takes a significant leap forward in architecture highlighted by features such as improved double precision performance and configurable cache hierarchy. The model GTX 480 used in our experiments is composed of 15 newly designed streaming multiprocessors (SMs). Each SM features 32 CUDA streaming processors and is capable of 16 double precision fused multiply-add operations per clock, which is an 8$\times$ improvement over the GT200 architecture. Another key architectural difference is that Fermi has two instruction dispatch units and most instructions can be dual-issued, which is different from the HyperThreads used in the Intel Nehalem processors. Two HyperThreads within a single core of Nehalem processors share a single instruction fetch and decoding unit.

The GPU implementations are developed using CUDA [24]. The vector-based diagonal factorization is composed of a major outer loop that factorizes one column/row per step. Unfortunately, advanced features offered on the GPU such as asynchronized communication/computation and concurrently kernel execution cannot be used for such an algorithm, as dependency exists among the outer loops and all inner steps. Therefore the GPU implementation suffers from low occupancy for small problem sizes. In order to optimize the GPU implementation, firstly we managed to squeeze every inner computation step except the Householder generator (i.e., Step 1 in Table 2) into the GPU to keep the entire matrix remained in the GPU memory throughout the computation. In other words, the Hessenberg reduction is a CPU-GPU co-design on the hybrid platform as shown in Figure 5. Step 1 in Table 2 is carried out on CPU and the remaining two steps are executed on GPU. Fortunately the calculation of Step 1 only needs the transportation of one column (or part of a column) of a matrix. Therefore we managed to minimize the round trip communication overhead to approximately 5% of overall execution time. All kernels are further incrementally optimized

Table 3: Platform Characteristics

Criteria	Xeon (Nehalem)	Tesla C1060	GTX 480
Cores	4	240/30	480
Frequency (GHz)	2.26	1.3	1.4
Double Precision GFLOPs	36	78	672
Memory Bandwidth (GB/s)	25.6	102	177.4

through memory coalescing, using of shared memory and assigning more work per thread. The configurable L1 cache on the Fermi GPU introduces more design tradeoffs for users. In our experiments, for kernels with limited or no usage of shared memory, configuring the L1 to be 48KB can yield an approximately 10% improvement on GTX 480. Moreover, we found that the multi-dimensional threads and blocks configuration can also affect the cache performance, especially when the performance differences are examined on both GT200 and Fermi. We achieved the best performance mostly at the thread configuration of 32×8 for the Fermi GPU.

V. RESULTS

Due to the data dependency within the QR eigenvalue algorithm, it is found that the first phase, i.e., the Hessenberg reduction, is able to get significant performance improvement through hardware acceleration technologies. Therefore, we present the performance result of Hessenberg reduction on different platforms in this section. In order to demonstrate the benefit of FPGA and GPU implementations, we implemented Alg. 1 on two CPUs as reference, i.e., Intel Itanium 2 (1.66 GHz) on the RASC RC100 platform and Intel Xeon E5520 on the Tesla C1060 platform.

A. Performance comparison

For comparison of acceleration over pure software based implementations, we coded the Hessenberg reduction phase in C++ on two software platforms.

The first platform is the RASC RC100 workstation with Intel Itanium 2 at 1.66 GHz. The size of L1 cache and L2 cache of the microprocessor is 16KB and 256KB [25], respectively. The software implementation on Itanium 2 is a sequential and direct implementation of Alg. 1. This sequential implementation is handcoded in C++ and single-threaded.

The second platform is a dual-socket Intel Xeon (Nehalem) system, as shown in Figure 5. The CPU is clocked at 2.26GHz with 8MB shared L3 cache and 12GB DDR3 memory (total 24GB for the entire system). The theoretical peak double precision floating-point performance is 36 GFLOP/S for each CPU. We implemented both sequential and parallel versions on Xeon. The sequential implementation is same to the one on Itanium processor. The parallel version is parallelized using OpenMP [26]. The critical computing intensive paths are parallelized by multiple threads first then further vectorized by the compiler utilizing the SSE units per core. These optimizations are achieved by enabling compiler optimization flags in GCC, such as *-sse4.2 -mtune=core2*. Furthermore, in order to achieve better scalability on all eight cores of both CPUs, we manually optimized our OpenMP code for better data locality control and further applied *numactl* to

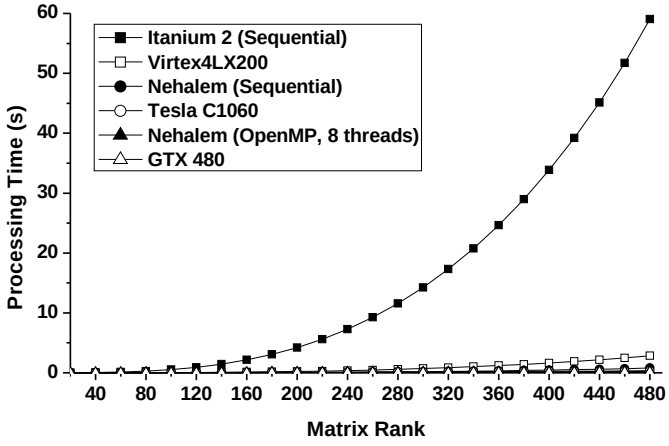

(a) Computation time

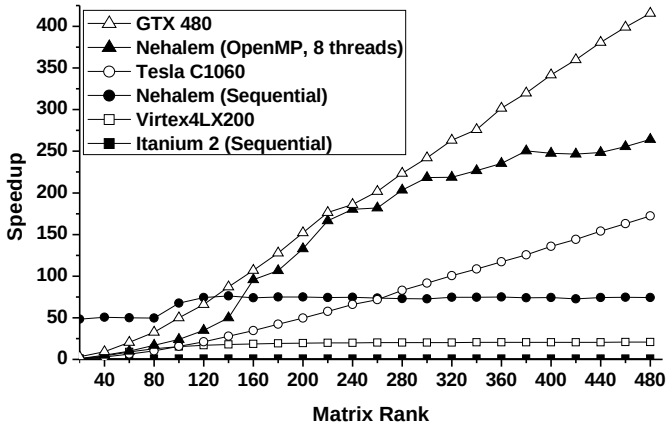

(b) Speedup against sequential implementation on Itanium 2

Fig. 6. Performance comparison of the vector-based Hessenberg reduction.

bind threads to physical CPU cores to avoid the NUMA penalty. Such an optimization significantly improves overall performance on two CPUs for up to 60%.

Overall, the vector-based Hessenberg reduction has been realized in 6 different implementations on three platforms as follows.

- The FPGA implementation;
- The Tesla C1060 GPU implementation;
- The GTX 480 GPU implementation;
- The sequential software implementation on Itanium 2;
- The sequential software implementation on Xeon E5520;
- The parallel software implementation of OpenMP.

We had another implementation by using Intel MKL library, which runs 8 threads on the two Xeon processors. However, the performance of the Intel MKL parallel implementation is close to the OpenMP implementation. Therefore, the performance result of MKL implementation is not included in this paper. The comparison among these 6 implementations

is illustrated in Figure 6, which includes both computation time and the speedup against the software implementation on Itanium 2. The computation time on both FPGA and GPU is the end-to-end time including data communication time and data processing time on the coprocessors. The FPGA configuration time is not counted, however.

From Figure 6(b), it can be found that the FPGA implementation is able to outperform the Itanium 2 by 20 folds. Both Virtex-4 and Intel Itanium 2 were technologies around Year 2005, and the FPGA implementation has the big advantage than the CPU when the device was just released to the market. However, the performance of the FPGA implementation lags behind the state-of-the-art microprocessor and the GPUs with a big margin. The inferior performance of FPGA is mainly due to three factors. (i) The FPGA device is running at a very low frequency, i.e., 100 MHz. If the FPGA device is running at the same speed as the microprocessor, their performance will tie. (ii) The direct implementation of Alg. 1 is a sequential process due to the data dependency. Although we have tried to parallelize the hardware implementation to the extreme, its performance is easily surpassed by modern multicore processors with improved design on cache and SSE when dealing with applications such as Hessenberg reduction. (iii) The 5 local memory banks on the current platform become the limiting factor to increase the parallelism in the hardware implementation. More memory banks are desired to achieve higher parallelism on FPGA device.

The state-of-the-art microprocessor used in the experiments, Intel Xeon processor, demonstrates a remarkable performance improvement than the Itanium 2. For example, the sequential implementation on Xeon outperforms the sequential implementation on Itanium 2 for 50 folds. Putting multiple cores in a single processor further improves its performance, which is contributed mainly by two factors. First, the SSE extension in modern processor provides the vector processing capability, which fits the computation pattern in the target application very well. Second, the target application is a streaming application in which the computation can be distributed onto multiple cores to parallelize the data processing. Due to the data distributing overhead, the benefit for using multiple cores can be achieved only when the problem size is big enough, e.g., the rank of the matrix reaches 150 in Fig 6(b).

It is evident that it will be beneficial to implement the application on GPU as the matrix rank increases. The Tesla implementation surpasses the sequential software implementation on Xeon at rank 260 and then approaches the parallel software implementation afterwards. Fermi consistently outperforms GT200 for approximately 4×. Two factors mainly contribute to the performance improvement on GPU architecture. The first one is the massive parallel computing capability provided by the hundreds of streaming processors. As the rank of the matrix increases, the occupancy of the streaming processors improves accordingly as well as the speedup. The second factor is the very high bandwidth provided by the graphics DDR memory. As shown in Table 3, the memory bandwidth on GPU is 7 times of the memory bandwidth on CPU. The high bandwidth is very beneficial when the data need to be frequently accessed from the memory.

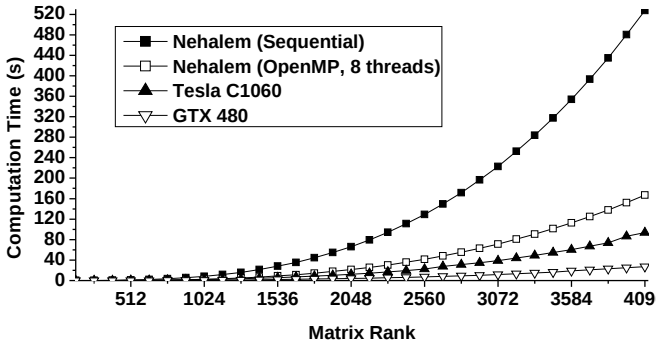

Fig. 7. Performance scalability of vector-based implementations of Hessenberg reduction.

B. Scalability

In the previous test, we limit the matrix rank at 480 because it is the biggest size the FPGA design can accommodate due to the size of the off-chip memory. In the meantime, it is clearly demonstrated that GPUs are capable of outperforming multicore CPUs as the matrix rank increases. In order to completely show the performance potential of GPUs, we compare them with the sequential and 8-thread x86 implementations on the Xeon platform (shown in Figure 5) with the matrix rank up to 4,096. By observing Figure 7, the implementation on Tesla C1060 is generally 2 times faster than the 8-thread Xeon implementation. The main reason has been described as above. The GTX 480 GPU outperforms all other versions consistently with a big margin. The Hessenberg reduction is a computation-intensive as well as communication-intensive problem. The abundant streaming processors and the high memory bandwidth on the Fermi architecture evidently give the advantage of GTX 480 compared with other technologies.

VI. CONCLUSION

Using FPGAs and GPUs as coprocessors to CPUs in parallel computing has been demonstrated in the context of an engineered material design, where the numerically intensive components of the RCW algorithm were implemented on these hardware acceleration technologies. The performance speedup on both coprocessors compared with software implementations on modern microprocessors are very impressive, proving both platforms are very suitable in scientific applications.

ACKNOWLEDGMENT

The authors would like to thank Lingyuan Wang with The George Washington University for the implementation of Hessenberg reduction on GPUs and Xeon.

REFERENCES

[1] D. H. Raguin and G. M. Morris, "Antireflection Structured Surfaces for the Infrared Spectral Region," *Applied Optics*, vol. 32, no. 7, pp. 1154–1167, 1993.

[2] P. Lalanne and J. Hugonin, "High-Order Effective-Medium Theory of Subwavelength Gratings in Classical Mounting: Application to Volume Holograms," *Journal of the Optical Society of America A*, vol. 15, no. 7, pp. 1843–1851, 1998.

[3] E. Noponen and J. Turunen, "Eigenmode Method for Electromagnetic Synthesis of Diffractive Elements with Three-Dimensional Profiles," *Journal of the Optical Society of America A*, vol. 11, no. 9, pp. 2494–2502, 1994.

[4] *Reconfigurable Application-Specific Computing User's Guide (007-4718-007)*, Silicon Graphics, Inc., Jan. 2008.

[5] T. Sterling, D. Becker, M. Warren, T. Cwik, J. Salmon, and B. Nitzberg, "An Assessment of Beowulf-Class Computing for NASA Requirements: Initial Findings from the First NASA Workshop on Beowulf-Class Clustered Computing," in *Proc. 1998 IEEE Aerospace Conference*, pp. 367–381, Mar. 1998.

[6] T. El-Ghazawi, E. El-Araby, M. Huang, K. Gaj, V. Kindratenko, and D. Buell, "The Promise of High-Performance Reconfigurable Computing," *IEEE Computer*, vol. 41, no. 2, pp. 78–85, Feb. 2008.

[7] A. Fournier and D. Fussell, "On the Power of the Frame Buffer," *ACM Transactions on Graphics*, vol. 7, no. 2, pp. 103–128, Apr. 1988.

[8] B. de Ruijsscher, G. N. Gaydadjiev, J. Lichtenauer, and E. Hendriks, "FPGA Accelerator for Real-Time Skin Segmentation," in *Proc. the 2006 IEEE/ACM/IFIP Workshop on Embedded Systems for Real Time Multimedia (ESTMED'06)*, pp. 93–97, 2006.

[9] J. Krüger and R. Westermann, "Linear Algebra Operators for GPU Implementation of Numerical Algorithms," in *Proc. International Conference on Computer Graphics and Interactive Techniques (ACM SIGGRAPH'03)*, pp. 908–916, 2003.

[10] L. Nyland, M. Harris, and J. Prins, "Fast N-body Simulation with CUDA," in *GPU Gems 3 (H. Nguyen: editor)*, Aug. 2007.

[11] Z. K. Baker and V. K. Prasanna, "Efficient Hardware Data Mining with the Apriori Algorithm on FPGAs," in *Proc. the 13th Annual IEEE Symposium on Field-Programmable Custom Computing Machines (FCCM'05)*, pp. 3–12, Apr. 2005.

[12] S. Che, J. Li, J. W. Sheaffer, K. Skadron, and J. Lach, "Accelerating Compute-Intensive Applications with GPUs and FPGAs," in *Proc. the 2008 Symposium on Application Specific Processors (SASP'08)*, pp. 101–107, 2008.

[13] M. G. Moharam, D. A. Pommet, E. B. Grann, and T. K. Gaylord, "Stable Implementation of the Rigourous Coupled-Wave Analysis for Surface Relief Gratings: Enhanced Transmittance Matrix Approach," *Journal of the Optical Society of America A*, vol. 12, no. 5, pp. 1077–1086, 1995.

[14] P. Lalanne, "Improved Formulation of the Coupled-Wave Method for Two-Dimensional Gratings," *Journal of the Optical Society of America A*, vol. 14, no. 7, pp. 1592–1598, 1997.

[15] J. W. Demmel, *Applied Numerical Linear Algebra*. Philadelphia, PA: Society for Industrical and Applied Mathematics (siam), 1997.

[16] J. G. F. Francis, "The QR Transformation, I," *The Computer Journal*, vol. 4, no. 3, pp. 265–271, 1961.

[17] J. G. F. Francis, "The QR Transformation, II," *The Computer Journal*, vol. 4, no. 4, pp. 332–345, 1962.

[18] V. N. Kublanovskaya, "On Some Algorithms for the Solution of the Complete Eigenvalue Problem," *USSR Computational Mathematics and Mathematical Physics*, vol. 1, no. 3, pp. 637–657, 1963.

[19] A. S. Householder, "Unitary Triangularization of a Nonsymmetric Matrix," *Journal of the ACM*, vol. 5, no. 4, pp. 339–342, Oct. 1958.

[20] O. Kilic, M. S. Mirotznik, and J. P. Durbano, "Application of FPGA Based FDTD Simulators to Rotman Lenses," in *Proc. 22nd ACES Conference*, 2006.

[21] J. P. Durbano, J. R. Humphrey, F. E. Ortiz, P. F. Curt, D. W. Prather, and M. S. Mirotznik, "Hardware Acceleration of the 3D Finite-Difference Time-Domain Method," in *Proc. IEEE AP-S International Symposium and USNC/URSI National Radio Science Meeting*, pp. 77–80, Jun. 2004.

[22] *Impulse C – http://www.impulsec.com*, Impulse Accelerated Technologies, Inc., 2009.

[23] *Mitrion C – http://www.mitrionics.com*, Mitrionics AB, 2009.

[24] *Nvidia CUDA Programming Guide 2.3.1*, Nvidia Corporation, Aug. 2009.

[25] *Dual-Core Update to the Intel Itanium 2 Processor Reference Manual*, Intel Corporation, Jan. 2006.

[26] *http://openmp.org*

Ozlem Kilic graduated from The George Washington University (1996) with a D.Sc. degree in Electrical Engineering. She is presently an Assistant Professor with The Catholic University of America. Before joining CUA, she worked at the U.S. Army Research Laboratories, Adelphi, MD and COMSAT Laboratories, Clarksburg, MD. She also holds the position of Senior Research Engineer for the Naval Surface Warfare Center (NSWC), Carderock Division. Her research areas include computational electromagnetics, hardware accelerated programming for scientific computing, antennas and propagation, and radiation and scattering problems from random media.

Miaoqing Huang is an Assistant Professor in the Department of Computer Science and Computer Engineering at University of Arkansas. His research interests include reconfigurable computing, high-performance computing architectures, cryptography, computer arithmetic, and cache design in Solid-State Drives. Huang received a B.S. degree in Electronics and Information Systems from Fudan University, China in 1998, and a Ph.D. degree in Computer Engineering from The George Washington University in 2009, respectively. He is a member of IEEE.

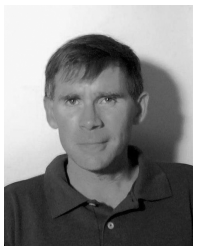

Charles Conner graduated from The Catholic University of America (Ph.D.) in 1999. He serves as a faculty member in the Electrical Engineering Department of the Capitol College, as well as an adjunct faculty at The Catholic University of America. He has been mainly working on various signal processing and computational problems for various government agencies. His specialty is digital signal processing and algorithm development.

Mark S. Mirotznik received the B.S.E.E. degree from Bradley University, Peoria, IL, in 1988 and the M.S.E.E. and Ph.D. degrees from the University of Pennsylvania, Philadelphia, in 1991 and 1992, respectively. He was a faculty member in the Department of Electrical Engineering at The Catholic University of America, Washington, DC until 2009. He is currently an Associate Professor and Director of Educational Outreach in the Department of Electrical and Computer Engineering at the University of Delaware, Newark DE. In addition to his academic positions, he is an associate editor of the Journal of Optical Engineering and also holds the position of Senior Research Engineer for the Naval Surface Warfare Center (NSWC), Carderock Division. His research interests include applied electromagnetics and photonics, computational electromagnetics, and bioelectromagnetics.

Diffraction of Obliquely Incident Plane Waves by an Impedance Wedge with Surface Impedances Being Equal to the Intrinsic Impedance of the Medium

Turgut İkiz and Mustafa K. Zateroğlu

Department of Electrical and Electronics Engineering
University of Cukurova, Adana, 01330, Turkey
tikiz@cu.edu.tr, mzateroglu@cu.edu.tr

Abstract ─ Diffraction of plane waves by an impedance wedge with surface impedances equal to the intrinsic impedance of surrounding medium is investigated for oblique incidence case. In the oblique incidence case, the scattering problem cannot be solved explicitly because of the resultant coupled system of functional equations unless the system is decoupled. Therefore under the assumed condition on wedge impedance, these functional equations are decoupled and the expression for the diffraction coefficient is derived as well as the diffracted fields.

Index Terms ─ Functional equations, impedance wedge, Maliuzhinets theorem, Sommerfeld integrals.

I. INTRODUCTION

In many practical applications, scatterers are partly wedge shaped metallic structures covered by dielectric materials or metallic structures with finite conductivity which can be simulated with impedance boundary conditions. Therefore, the problem of diffraction by an impedance wedge is investigated by a number of scientists and is very important for both civil and military applications.

Diffraction by an impedance wedge was first solved by Maliuzhinets for the normal incidence case [1]. In this solution, the total field was expressed by the integral of an unknown spectral function. The unknown spectral function was determined using the boundary conditions, the edge conditions, and the radiation condition. The fundamental contribution of the Maliuzhinets method is the reduction of the integral equation into a first order functional equation. But for the oblique incidence case, the problem cannot be solved explicitly, since the resultant equations form a coupled functional equations system.

The solutions for the problem under consideration are available only for some limited wedge opening angles and only under some assumption for the surface impedance of this wedge [2-22].

In this study, applying the Leontovich boundary conditions, a coupled differential equations system is derived for the z-components of the fields. Using the similarity transformation, the relevant matrices are diagonalized assuming that the surface impedance is equal to the free space impedance.

The solution for the Helmholtz equation is sought in the form of Sommerfeld integrals. In order to solve the Maliuzhinets functional equations, the Maliuzhinets theorem is applied to the Sommerfeld integrals. Solving the functional equations, the closed form solution is derived and the uniform asymptotic solution is obtained by applying the steepest descent path method to the Sommerfeld integrals. The numerical results are obtained for different wedge opening and incidence angles and they are shown in Figs. 3 through 7.

II. FORMULATION OF THE PROBLEM

The problem under consideration is a wedge with an opening angle of 2Φ, where the edge coincides with the z-axis. The direction of propagation of the incidence wave is specified by the angles β and ϕ_0 as shown in Fig. 1. The

incident field is determined by the z-components of the electromagnetic field.

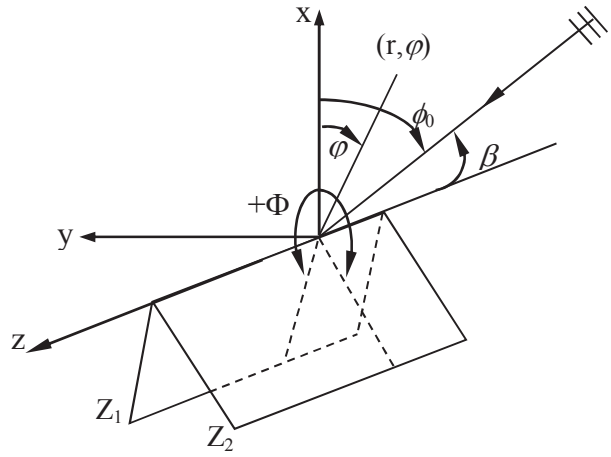

Fig. 1. The geometry of the problem.

Due to the invariance of both the wedge geometry and the impedance with respect to z, the problem can be reduced to a two dimensional problem and the z-components of the electric and magnetic field vectors of the incident wave can be represented as

$$\tilde{H}_z^i = H_z^i(r,\varphi)\exp(ik\cos\beta z), \quad (1)$$

$$\tilde{E}_z^i = E_z^i(r,\varphi)\exp(ik\cos\beta z), \quad (2)$$

where

$$H_z^i = H_0\exp\{-ikr\sin\beta\cos(\varphi-\varphi_0)\}, \quad (3)$$

and

$$E_z^i = E_0\exp\{-ikr\sin\beta\cos(\varphi-\varphi_0)\}. \quad (4)$$

Using the Maxwell's equations, the field components can be expressed in terms of z-components as follows:

$$H_r = \frac{1}{iZ_0k\sin^2\beta}\left(\frac{1}{r}\frac{\partial E_z}{\partial\varphi} - Z_0\cos\beta\frac{\partial H_z}{\partial r}\right), \quad (5)$$

and

$$E_r = \frac{i}{k\sin^2\beta}\left(\frac{Z_0}{r}\frac{\partial H_z}{\partial\varphi} + \cos\beta\frac{\partial E_z}{\partial r}\right), \quad (6)$$

where $k=\omega\sqrt{\varepsilon_0\mu_0}$ is the free space wave number and Z_0 is the free space impedance given by

$$Z_0 = \sqrt{\frac{\mu_0}{\varepsilon_0}}. \quad (7)$$

On the surfaces of the wedge, the Leontovich impedance boundary condition can be represented as

$$\vec{E} - (\hat{n}.\vec{E})\hat{n} = Z_{1,2}\hat{n}\times\vec{H}. \quad (8)$$

Applying boundary conditions result in a matrix equation system defined as

$$\frac{1}{r}\begin{bmatrix}\frac{\partial H_z}{\partial\varphi}\\ \frac{\partial E_z}{\partial\varphi}\end{bmatrix}\Bigg|_{S_j,\varphi_j} = (-1)^{j+1}ik\sin^2\beta A\begin{bmatrix}H_z\\ E_z\end{bmatrix}\Bigg|_{S_j} + \cos\beta B\begin{bmatrix}\frac{\partial H_z}{\partial r}\\ \frac{\partial E_z}{\partial r}\end{bmatrix}\Bigg|_{S_j}, \quad (9)$$

where sentence

$$A = \begin{bmatrix}\frac{Z_j}{Z_0} & 0\\ 0 & \frac{Z_0}{Z_j}\end{bmatrix}, \quad (10)$$

and

$$B = \begin{bmatrix}0 & -\frac{1}{Z_0}\\ Z_0 & 0\end{bmatrix}, \quad (11)$$

and j=1,2. To obtain the unknown, this coupled matrix system must be diagonalized. Applying similarity transformation to matrix B can produce a diagonal matrix system. To reach this aim the transformation matrix can first be written as

$$\begin{bmatrix}H_z\\ E_z\end{bmatrix} = P\begin{bmatrix}u\\ v\end{bmatrix}, \quad (12)$$

where P is the similarity transform of matrix B, and is defined as

$$P = \begin{bmatrix}P_{11} & P_{12}\\ P_{21} & P_{22}\end{bmatrix}. \quad (13)$$

After the necessary manipulations P can be rewritten as

$$P = \begin{bmatrix}i & \frac{1}{Z_0}\\ Z_0 & i\end{bmatrix}. \quad (14)$$

By using this similarity transform matrix, matrices A and B are diagonalized as follows

$$P^{-1}AP=\begin{bmatrix} \frac{1}{2}\left(\frac{Z_j}{Z_0}+\frac{Z_0}{Z_j}\right) & \frac{i}{2Z_0}\left(\frac{Z_0}{Z_j}-\frac{Z_j}{Z_0}\right) \\ i\frac{Z_0}{2}\left(\frac{Z_j}{Z_0}-\frac{Z_0}{Z_j}\right) & \frac{1}{2}\left(\frac{Z_j}{Z_0}+\frac{Z_0}{Z_j}\right) \end{bmatrix}, \quad (15)$$

and

$$P^{-1}BP=\begin{bmatrix} i & 0 \\ 0 & -i \end{bmatrix}. \quad (16)$$

Within equation (15) the diagonalization condition is observed as

$$\frac{Z_0}{Z_j}-\frac{Z_j}{Z_0}=0, \quad (17)$$

and finally the decoupled matrix system can be written as

$$\frac{1}{r}\begin{bmatrix} \frac{\partial u}{\partial \varphi} \\ \frac{\partial v}{\partial \varphi} \end{bmatrix}_{S_j} = \begin{bmatrix} 1 & 0 \\ 0 & 1 \end{bmatrix}(-1)^{j+1} ik\sin^2\beta \begin{bmatrix} u \\ v \end{bmatrix}_{S_j} + \cos\beta \begin{bmatrix} i & 0 \\ 0 & -i \end{bmatrix} \begin{bmatrix} \frac{\partial u}{\partial r} \\ \frac{\partial v}{\partial r} \end{bmatrix}_{S_j}. \quad (18)$$

The solutions for field components are sought in the form of Sommerfeld integrals as

$$(u,v)=\frac{1}{2\pi i}\int_{\gamma} f_j(\alpha+\varphi)e^{-ikr\sin\beta\cos\alpha}d\alpha, \quad (19)$$

where γ is the Sommerfeld double loops shown in Fig. 2, and α is the complex planes variable. The calculation of the unknown spectral functions represented by f_j is given in the section titled far field solution.

Application of the Malyuzhinets' theorem to the functions *u* and *v* gives the following equations for $\varphi=\pm\Phi$.

$$\left[\sin(\alpha-\theta)-(-1)^j\right]f_1(\alpha\pm\Phi) + \left[\sin(\alpha+\theta)+(-1)^j\right]f_1(-\alpha\pm\Phi)=C_1'\sin\alpha, \quad (20)$$

and

$$\left[\sin(\alpha+\theta)-(-1)^j\right]f_2(\alpha\pm\Phi) + \left[\sin(\alpha-\theta)+(-1)^j\right]f_2(-\alpha\pm\Phi)=C_2'\sin\alpha, \quad (21)$$

where $\theta=\cos^{-1}\left(\frac{1}{\sin\beta}\right)$.

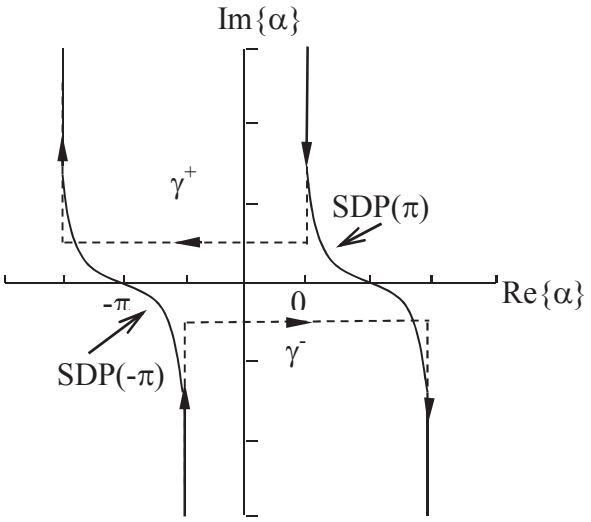

Fig. 2. The complex α plane with Sommerfeld double loops and the steepest descent paths SDP(-π) and SDP(π).

III. FAR FIELD SOLUTION

The homogeneous solutions $f_{10}(\alpha)$ and $f_{20}(\alpha)$ for the functional equations (20) and (21) can be represented in terms of χ_ϕ functions as follows

$$f_{10}(\alpha)=\frac{\chi_\phi^2\left(\alpha+\Phi+\theta+\frac{\pi}{2}\right)}{\chi_\phi^2\left(\alpha-\Phi+\theta-\frac{\pi}{2}\right)}\frac{\chi_\phi^2\left(\alpha-\Phi-\theta+\frac{\pi}{2}\right)}{\chi_\phi^2\left(\alpha+\Phi-\theta-\frac{\pi}{2}\right)}, \quad (22)$$

$$f_{20}(\alpha)=\frac{\chi_\phi^2\left(\alpha+\Phi-\theta+\frac{\pi}{2}\right)}{\chi_\phi^2\left(\alpha-\Phi-\theta-\frac{\pi}{2}\right)}\frac{\chi_\phi^2\left(\alpha-\Phi+\theta+\frac{\pi}{2}\right)}{\chi_\phi^2\left(\alpha+\Phi+\theta-\frac{\pi}{2}\right)}. \quad (23)$$

It is known that $\cos\left(\frac{\theta}{2}\right)=\frac{\chi_\phi(\theta+2\Phi)}{\chi_\phi(\theta-2\Phi)}$.

The functional equations for $f_j(\alpha)$ should be supplemented by an additional condition [13] namely $f_j(\alpha)-\frac{1}{\alpha-\phi_0}$ is regular in $|\mathrm{Re}\,\alpha|\le\Phi$. Then, the solution can be represented in the following form to satisfy the additional condition

$$f_j(\alpha) = f_{j0}(\alpha)\sigma_{\phi_0}(\alpha)\xi_j(\alpha). \quad (24)$$

Here a new function is defined as

$$F_{j0}(\alpha) = f_{j0}(\alpha)\sigma_{\phi_0}(\alpha). \quad (25)$$

New unknown spectral functions $\xi_j(\alpha)$ are introduced to facilitate the solution and $\sigma_{\phi_0}(\alpha)$ is defined as

$$\sigma_{\phi_0}(\alpha) = \frac{\mu\cos(\mu\phi_0)}{\sin(\mu\alpha)-\sin(\mu\phi_0)}, \quad (26)$$

where μ is equal to $\mu = \frac{\pi}{2\Phi}$ and $\xi_j(\alpha)$ has no poles and zeros in the strip $|\mathrm{Re}\,\alpha| \le \Phi$ .The function $\sigma_{\phi_0}(\alpha)$ satisfies the following relation

$$\sigma_{\phi_0}(\alpha \pm \Phi) = \sigma_{\phi_0}(-\alpha \pm \Phi). \quad (27)$$

The known functions $F_{j0}(\alpha)$ satisfy equation (20) and (21) as $f_{j0}(\alpha)$. Then, $\xi_j(\alpha)$ obey the simple functional equations where λ is wavelength sentence.

$$\xi_j(\alpha \pm \Phi) - \xi_j(-\alpha \pm \Phi) = 0. \quad (28)$$

Since the residue of f_j at $\alpha = \phi_0$ must give the incident field, the following can be written

$$\text{Res } F_{j0}(\alpha)\xi_j(\alpha)\big|_{\alpha=\phi_0} = 1, \quad (29)$$

where Res $f(\alpha)\big|_{\alpha=\alpha_0}$ is used for the residue of a function $f(\alpha)$ at a point α_0. It follows that

$$\xi_j(\alpha) = \frac{1}{f_{j0}(\phi_0)}. \quad (30)$$

So the solutions for the unknown spectral functions are given by

$$f_j(\alpha) = \frac{\sigma_{\phi_0}(\alpha) f_{j0}(\alpha)}{f_{j0}(\phi_0)}. \quad (31)$$

By substituting (31) into (19) and by evaluating the integral asymtoticly by the steepest descent method gives

$$U(r,\varphi) \sim \frac{e^{-i\frac{\pi}{2}} e^{i\frac{\pi}{4}} e^{-kr\sin\beta - i\frac{\pi}{4}}}{\sqrt{2\pi kr\sin\beta}}\left[f_1(\varphi-\pi) - f_1(\varphi+\pi)\right], \quad (32)$$

and

$$V(r,\varphi) \sim \frac{e^{-i\frac{\pi}{2}} e^{i\frac{\pi}{4}} e^{-kr\sin\beta - i\frac{\pi}{4}}}{\sqrt{2\pi kr\sin\beta}}\left[f_2(\varphi-\pi) - f_2(\varphi+\pi)\right]. \quad (33)$$

When inverse transformation is applied to (32) and (33), H_z and E_z are obtained as

$$\begin{bmatrix} H_z \\ E_z \end{bmatrix} = \begin{bmatrix} i & \frac{1}{Z_0} \\ Z_0 & i \end{bmatrix} \begin{bmatrix} u \\ v \end{bmatrix}. \quad (34)$$

H_z is also written as

$$H_z = iu + \frac{1}{Z_0}v. \quad (35)$$

More specifically

$$H_z(r,\varphi) = e^{-i\frac{\pi}{2}} e^{i\frac{\pi}{4}} \frac{e^{-kr\sin\beta - i\frac{\pi}{4}}}{\sqrt{2\pi kr\sin\beta}} \times \left\{ i\left[f_1(\varphi-\pi) - f_1(\varphi+\pi)\right] + \frac{1}{Z_0}\left[f_2(\varphi-\pi) - f_2(\varphi+\pi)\right]\right\} = \frac{e^{-kr\sin\beta}}{\sqrt{r}} D(\varphi), \quad (36)$$

where $D(\varphi)$ is the diffraction coefficient given as

$$D(\varphi) = \frac{e^{-i\frac{\pi}{4}}}{\sqrt{2\pi k\sin\beta}}\left\{ i\left[f_1(\varphi-\pi) - f_1(\varphi+\pi)\right] + \frac{1}{Z_0}\left[f_2(\varphi-\pi) - f_2(\varphi+\pi)\right]\right\}, \quad (37)$$

where $f_j(\alpha)$ is defined in (24) and the related functions $f_{10}(\alpha)$, $f_{20}(\alpha)$, $\sigma_{\phi 0}(\alpha)$, and $\xi_j(\alpha)$ are given in (22), (23), (26), and (30), respectively.

IV. NUMERICAL RESULTS

In this paper, diffraction of obliquely incident plane electromagnetic waves by impedance being equal to the intrinsic impedance of surrounding medium is considered. This study is the first to investigate this case. Therefore, we reduced the problem to the normal incidence case taking $\beta = 90^o$ to be able to compare our results with the known studies. In Figs. 3 through 5, it is obvious that our results and the results obtained by İkiz previously and by Büyükaksoy [17, 23] are very similar.

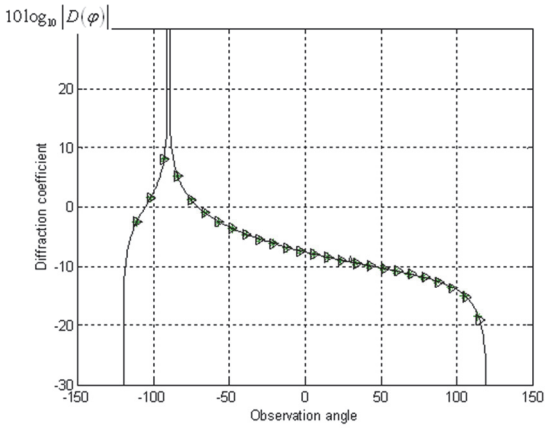

Fig. 3. Comparison of the results ($\Phi=120^o$, $\phi_o=30^o$). (*): results obtained previously by İkiz (▷): results obtained by İkiz in this study.

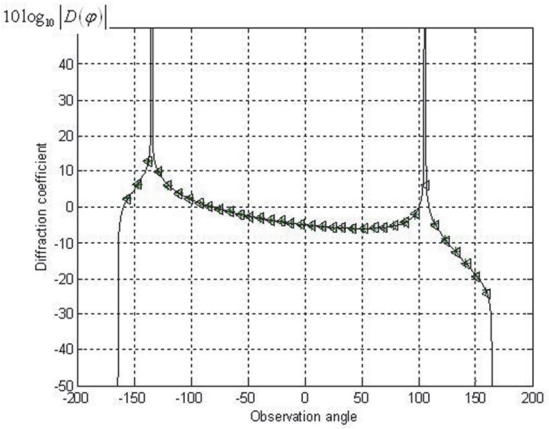

Fig. 4. Comparison of the the results ($\Phi=165^o$, $\phi_o=45^o$) (*): results obtained previously by İkiz (◁): results obtained by İkiz in this study.

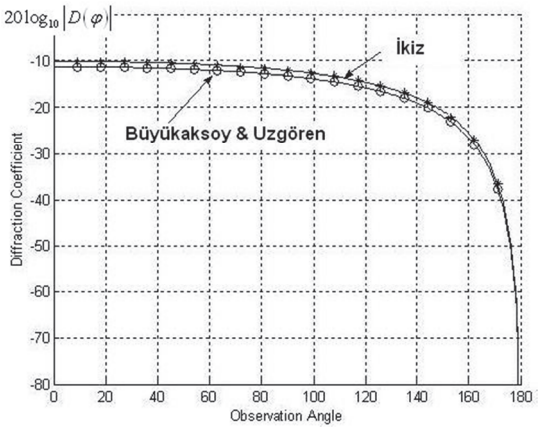

Fig. 5. Comparison of the results by Büyükaksoy & Uzgören(o) and by İkiz(*) $\Phi=180^o$.

In Figs. 6 and 7, we represent the diffraction coefficients for different values of incidence and wedge opening angles.

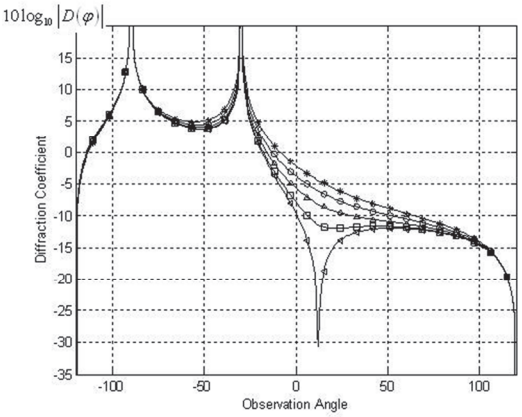

Fig. 6. Diffraction coefficient $10\log_{10}\left|D(\varphi)\right|$ versus observation angle with $\Phi=120^o$, $\phi_o=90^o$, $\beta=30^o$ (*), 45^o (o), 60^o.(▵), 75^o (□), 90^o (◁).

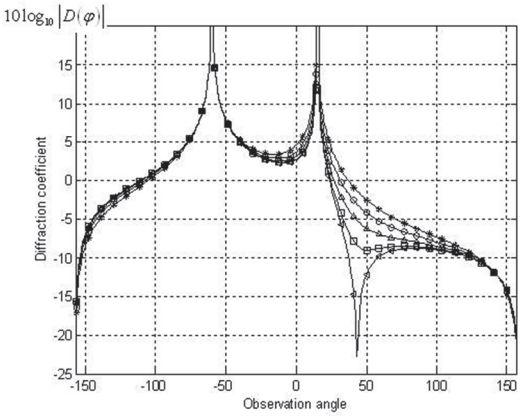

Fig. 7. Diffraction coefficient $10\log_{10}\left|D(\varphi)\right|$ versus observation angle with $\Phi=157{,}5^o$, $\phi_o=120^o$, $\beta=30^o$ (*), 45^o (o), 60^o.(▵), 75^o (□), 90^o (◁).

V. CONCLUSION

The wedge surface impedance being equal to the intrinsic impedance of the surrounding medium, not only presents a convenient mathematical problem, but it can also correspond to a practical structure especially when it is assumed that this condition can be satisfied by choosing the appropriate ε_r and μ_r values for any composite material. From a mathematical point of view, this problem should also be considered as a first step for solving a wedge scattering problem

with any surface impedance, with plane waves at any random incidence angle.

ACKNOWLEDGMENT

We would like to thank to M. A. Lyalinov for his suggestions.

REFERENCES

[1] G. D. Malyuzhinets, "Generalisation of the Reflection Method in the Theory of Diffraction of Sinusoidal Waves. Doctoral dissertation," P.N. Lebedev Phys. Inst. Acad. Sci. USSR, 1950.

[2] W. E. Williams, "Diffraction of an E-polarized Plane Wave by an Imperfectly Conducting Wedge," Proc. R. Soc. London A 252, pp. 376-393, 1959.

[3] T. B. A. Senior, "Diffraction by an Imperfectly Conducting Wedge," *Comm. Pure Appl. Math*., vol. 12, pp. 337-372, 1959.

[4] M. P. Sakharova and A. F. Filippov, "The Solution of a Nonstationary Problem of Diffraction by an Impedance Wedge in Tabulated Functions," *Zh. Vych. Matem. i Mat. Fiziki*, vol. 7, pp. 568-579, 1967.

[5] A. Mohsen, "On the Diffraction of an Arbitrary Wave by a Wedge," *Can. J. Phys.*, vol. 60, pp. 1686-1690, 1982.

[6] S.-Y. Kim, RA J.-W., and S.-Y. Shin, "Edge Diffraction by Dielectric Wedge of Arbitrary Angle," *Electronic Letters*, vol. 19, no. 20, pp. 851-853, 1983.

[7] A. Ciarkowski, J. Boersma, and R. Mittra, "Plane-Wave Diffraction by a Wedge-A Spectral Domain Approach," *IEEE Trans. on Antennas and Propagation*, vol. 32, no. 1, pp. 20-29, 1984.

[8] R. Tiberio, G. Pelosi, and G. Manara, "A Uniform GTD Formulation for the Diffraction by a Wedge with Impedance Faces," *IEEE Trans. on Antennas and Propagation*, vol. 33, no. 8, pp. 867-873, 1985.

[9] R. G. Rojas, "Electromagnetic Diffraction of an Obliquely Incident Plane Wave Field by a Wedge with Impedance Faces," *IEEE Trans. on Antennas and Propagation*, vol. 36, no. 7, pp. 956-970, 1988.

[10] R. Tiberio, G. Pelosi, G. Manara, and P. H. Pathak, "High-Frequency Scattering from a Wedge with Impedance Faces Illuminated by a Line Source, Part I: Diffraction," *IEEE Trans. on Antennas and Propagation*, vol. 37, no. 2, pp. 212-218, 1989.

[11] A. D. Rawlins, "Diffraction of an *E*-or *H*-polarized Plane Wave by a Right-Angle Wedge with Imperfectly Conducting Faces," *Q.JI Mech. Appl. Math*., 43, pt. 2, pp. 161-172, 1990.

[12] Y. Liu and R. Ciric, "Improved Formulas for the Diffraction by a Wedge," *Radio Science*, vol. 28, no. 5, pp. 859-863, 1993.

[13] A. V. Osipov and A. N. Norris, "The Malyuzhinets Theory for Scattering from Wedge Boundaries: A Review," *Wave Motion*, vol. 29, pp. 313-340, 1999.

[14] A. N. Norris and A. V. Osipov, "Far-Field Analysis of the Malyuzhinets Solution for Plane and Surface Waves Diffraction by an Impedance Wedge," *Wave Motion*, vol. 30, pp. 69-89, 1999.

[15] M. A. Lyalinov and N. Y. Zhu, "Diffraction of Skewly Incident Plane Wave by an Anisotropic Impedance Wedge- A Class of Exactly Solvable Cases," *Wave Motion*, vol. 30, pp. 275-288, 1999.

[16] A. D. Andeev, "On the Special Function of the Problem of Diffraction by a Wedge in an Anisotropic-Plasma," *Radio Tekhnika I Elektronika*, vol. 39, pp. 885–892, 1994.

[17] T. İkiz and F. Karaömerlioğlu, "Diffraction of Plane Waves by a Two-Impedance Wedge in Cold Plasma," *Journal of Electromagnetic Waves and Applications*, vol. 18, no.10, pp. 1361-1372, 2004.

[18] T. B. A. Senior, "Diffraction Tensros for Imperfectly Conducting Edges," *Radio Sci*., vol. 10, pp. 911-919, Oct. 1975.

[19] O. M. Bucci and G. Franceschetti, "Electromagnetic Scattering by a Half-Plane with Two Impedances," *Radio Sci*., vol. 11, pp. 49-59, Jan. 1976.

[20] V. G. Vaccaro, "Electromagnetic Diffraction from a Right-Angled Wedge with Soft Conditions on One Face," *Opt. Acta*, vol. 28, pp. 293-311, Mar. 1981.

[21] T. B. A. Senior and J. L. Volakis, "Scattering by an Imperfect Right-Angled Wedge," *IEEE Trans. Antennas and Propagation*, vol. 34, pp. 681-689, May 1986.

[22] J. L. Volakis, "A Uniform Geometrical Theory of Diffraction for an Imperfectly

Conducting Half-Plane," *IEEE Trans. Antennas and Propagation*, vol. AP-34, pp. 172-180, Feb. 1986.

[23] A. Büyükaksoy and G. Uzgören, "Kırınım Problemleri (Diffraction Problems)," *Gebze High Technology Istitute Publications*, ISBN 975-8316-03-6, 1999.

Turgut İkiz was born in Ereğli, Turkey on August 1, 1966. He received the B.S. degree in Electrical and Electronics Engineering from Middle East Technical University in 1989. He received the M.S. and Ph.D. degrees from Çukurova University in 1992 and 1998, respectively. His research interests are propagation and diffraction of electromagnetic waves. He is currently an Associate professor in Electromagnetics at Çukurova University.

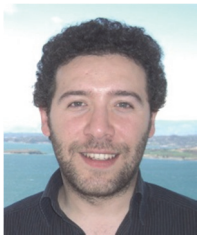

Mustafa Kemal Zateroğlu was born in İskenderun, Turkey on August 15, 1977. He received the B.S. degree in Electronics Engineering from Erciyes University in 1999. He received the M.S. degree in Electrical and Electronics Engineering from Çukurova University in 2002. He is expected to complete his Ph.D. study in 2011 at Çukurova University. His research interests are diffraction problems and numerical analysis of electromangetic waves, full wave solvers.

Equivalent Electromagnetic Currents on Infinite Stratified Homogeneous Bi-anisotropic Media Backed by A PEC Layer

Sen Tian[1], Zhuo Li[1, 2], Chang Qing Gu[1], and Dan Ping Ding[3]

[1] College of Electronic Information Engineering
Nanjing University of Aeronautics and Astronautics, Nanjing 210016, P. R. China

[2] State Key Laboratory of Millimeter Waves
Southeast University, Nanjing 210096, P. R. China

[3] Nanjing Panda Handa Company Limited
Nanjing 210002, P. R. China

Abstract - In this work, the equivalent electromagnetic (EM) currents on the surface of stratified homogeneous bi-anisotropic media backed by a perfect electric conductor (PEC) layer are derived and investigated. By using the representation of Maxwell's equations with a first-order state-vector differential equation, the tangential field components and the corresponding equivalent EM currents at the interface between the outmost bi-anisotropic media layer and the free space is derived analytically and can be easily degenerated into the single anisotropic and isotropic cases. This work is considered as a further step in the study of the EM characteristics of stratified complex media and the obtained results may provide a way for approximately fast calculation of the EM scattering from PEC targets coated by stratified homogeneous bi-anisotropic media. Simulation results are given to validate our analysis and conclusions.

Index Terms **–** Bi-anisotropic media, equivalent electromagnetic current, high frequency method, scattering.

I. INTRODUCTION

In modern warfare, stealth technology has been becoming one of the most important technologies for military targets. Besides shape stealth, coating is the most commonly used method. The equipped aircrafts and warships are usually coated with one-layer or multi-layer radar absorption materials (RAM), which are commonly anisotropic or bi-anisotropic. To obtain the scattering characteristics and the evaluation of these stealth targets, several full-wave methods have been employed, in which the finite-difference time-domain (FDTD) method [1-3], the couple dipole approximation method [4], the method of moments (MoM) [5], and the finite element method (FEM) are the most representative ones. However, these methods are not suitable for electrically large EM scattering problems owing to limited computational resources. Asymptotic methods, such as the physical optics (PO) method with its extension the physical theory of diffraction (PTD), the geometrical optics (GO) method with its extension the geometrical theory of diffraction (GTD), and the shooting and bouncing ray (SBR) method, can solve electrically large problems at the cost of losing precision since these approximate methods do not exactly capture the EM characteristics of complex media. Our work here concentrates on the hybridization of the full-wave and the asymptotic methods based on the generalized field equivalence principle. As we know, the PO method utilizes the induced PO currents on the surface of PEC objects to calculate the scattered field based on the high frequency approximation that the induced equivalent electric current $\bar{J}$ at a certain point is solely determined by the incident magnetic field $\bar{H}$ and the normal vector $\hat{n}$ at that point with the formula $\bar{J} = 2\hat{n} \times \bar{H}$. Another assumption is also made in this approximation that each illuminated point is regarded as an infinite plane without considering the curvature at that point. Thus, the mutual coupling of two arbitrary induced currents is not taken into consideration. This approximation is well suited for electrically large EM scattering problems. So in this work,

we inherit this approximation idea for the extraction of equivalent electric and magnetic currents on the surface of an infinite stratified homogeneous bi-anisotropic media backed by a PEC layer. These analytical equivalence currents give us an alternative solution for fast approximate estimation of the EM scattering from complex coated PEC targets through asymptotic methods.

In 1950, Abelès [6] provided a solution called characteristic matrix to solve the problem of EM wave propagation in isotropic stratified medium in a single direction. Later in the 1970s, Teitler and Henvis [7] applied Abelès's characteristic matrix method to the stratified anisotropic media. Then, Berreman [8] introduced a 4×4 matrix technique to solve the problem of reflection and transmission of EM waves in anisotropic material. Graglia [9] used integro-differential equations to solve the scattering problem in linear, lossy, anisotropic media. References [10] provided another approach that employs a first-order state-vector differential equation representation of Maxwell's equations and uses a 4×4 transition matrix relating the tangential field components at the input and output planes of the anisotropic region to represent the solution. References [11-13] provide several analytical methods to the propagation problem in stratified anisotropic media. All of the above works only considered the reflection and transmission of EM waves in the stratified anisotropic material.

In this paper, we focus on the equivalent EM currents extraction on the surface of anisotropic or bi-anisotropic media backed by a PEC layer, which can be employed in the estimation of EM scattering from electrically large PEC targets coated by stratified anisotropic or bi-anisotropic media. In Section II and III, the EM wave propagation in multiple layered infinite bi-anisotropic media is studied, in which the tangential EM components in bi-anisotropic material are derived from Maxwell's equation in the form of a 4×4 matrix. After imposing the boundary condition that the tangential EM components are continuous across the boundary of two different media and the tangential electric field is zero on the surface of the PEC layer, the relation of the tangential EM field components of the outmost and inmost layer of the stratified bi-anisotropic is obtained. Then the total tangential EM fields on the surface of the outmost anisotropic media layer are derived analytically and the equivalent EM currents on the surface of the outmost layer of bi-anisotropic are obtained. Finally, we show in Section III that these equivalent currents can be easily degenerated into the single anisotropic and isotropic cases. Simulation results are given in Section IV to validate our conclusions.

II. PROPAGATION EQUATION IN STRATIFIED BIANISOTROPIC MATERIAL

In this paper, the infinite stratified homogeneous bi-anisotropic coating is viewed as a one-dimensional issue. As shown in Fig.1, that a monochromatic plane wave is obliquely incident from free space to an infinite stratified homogeneous bi-anisotropic media backed with a PEC layer. Each layer is assumed to be infinite towards x and y directions. The position of each layer along the z direction is set as $z = d_n\,(n = 0,1,2\cdots,N)$.

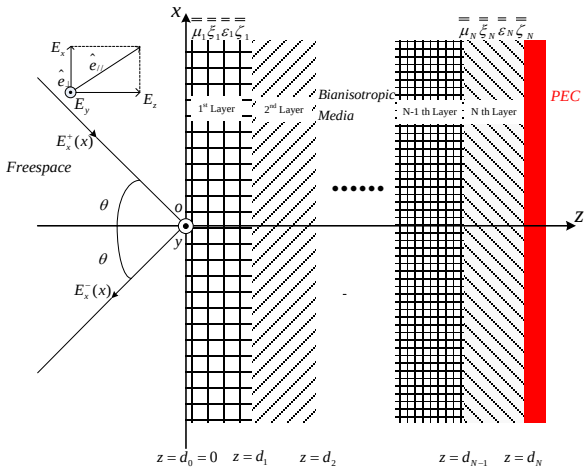

Fig. 1. A monochromatic plane wave is obliquely incident from free space to an infinite stratified homogeneous bi-anisotropic media backed with a PEC layer.

Imposing the phase matching condition in each layer, the *x*-component of wave vector k_n should be equal and denoted by k_x, in which the subscript n stands for the nth layer. Using the $e^{j\omega t}$ time convention, the phasor fields in the nth layer can be written in a separable product form as below

$$\begin{aligned}\vec{E}_n(x,z) &= \vec{E}_n(z)e^{-jk_x x},\\ \vec{H}_n(x,z) &= \vec{H}_n(z)e^{-jk_x x},\end{aligned} \tag{1}$$

where $k_x = k_0 \sin\theta$ is the *x*-component of k_0. k_0 is the incident wave number in free space and θ is

the incident angle. For bi-anisotropic materials, the source-free Maxwell's equations can be expressed as

$$\begin{aligned} -\nabla\times\vec{E}_n &= j\omega\bar{\bar{\mu}}_n\cdot\vec{H}_n + j\omega\bar{\bar{\varsigma}}_n\cdot\vec{E}_n, \\ \nabla\times\vec{H}_n &= j\omega\bar{\bar{\xi}}_n\cdot\vec{H}_n + j\omega\bar{\bar{\varepsilon}}_n\cdot\vec{E}_n, \end{aligned} \tag{2}$$

where $\bar{\bar{\varepsilon}}_n$, $\bar{\bar{\mu}}_n$ are the dyadic permittivity and permeability, $\bar{\bar{\varsigma}}_n$, $\bar{\bar{\xi}}_n$ are the dyadic magneto electric parameters as follows:

$$\bar{\bar{\varepsilon}}_n = \begin{bmatrix} \varepsilon_{n11} & \varepsilon_{n12} & \varepsilon_{n13} \\ \varepsilon_{n21} & \varepsilon_{n22} & \varepsilon_{n23} \\ \varepsilon_{n31} & \varepsilon_{n32} & \varepsilon_{n33} \end{bmatrix},$$

$$\bar{\bar{\mu}}_n = \begin{bmatrix} \mu_{n11} & \mu_{n12} & \mu_{n13} \\ \mu_{n21} & \mu_{n22} & \mu_{n23} \\ \mu_{n31} & \mu_{n32} & \mu_{n33} \end{bmatrix},$$

$$\bar{\bar{\varsigma}}_n = \begin{bmatrix} \varsigma_{n11} & \varsigma_{n12} & \varsigma_{n13} \\ \varsigma_{n21} & \varsigma_{n22} & \varsigma_{n23} \\ \varsigma_{n31} & \varsigma_{n32} & \varsigma_{n33} \end{bmatrix},$$

$$\bar{\bar{\xi}}_n = \begin{bmatrix} \xi_{n11} & \xi_{n12} & \xi_{n13} \\ \xi_{n21} & \xi_{n22} & \xi_{n23} \\ \xi_{n31} & \xi_{n32} & \xi_{n33} \end{bmatrix}. \tag{3}$$

Substituting Eq. (1) into Eq. (2) and canceling the common exponential factor, six first-order differential equations can be derived. By eliminating the *z*-component of the EM field, the above six equations can be reduced to four independent equations. If we define a state vector in terms of the transverse field components of $\vec{E}_n$ and $\vec{H}_n$

$$\Psi_n(z) = \begin{bmatrix} \Psi_n^{(1)}(z) \\ \Psi_n^{(2)}(z) \\ \Psi_n^{(3)}(z) \\ \Psi_n^{(4)}(z) \end{bmatrix} = \begin{bmatrix} E_{nx}(z) \\ E_{ny}(z) \\ H_{nx}(z) \\ H_{ny}(z) \end{bmatrix}, \tag{4}$$

the four independent first-order differential equations can be expressed as

$$\frac{d}{dz}\Psi_n(z) = \Gamma_n\cdot\Psi_n(z), \tag{5}$$

in which the complex elements of the 4×4 Γ matrix are given in Appendix(I).

The solutions of Eq. (5) have the form of non-uniform plane waves as follow

$$\Psi_n(z) = B_n E_n A_n, \tag{6}$$

where $E_n = Diag[e^{\lambda_{n1}z},\ e^{\lambda_{n2}z},\ e^{\lambda_{n3}z},\ e^{\lambda_{n4}z}]$, in which λ_{nj} (j=1,2,3,4) are the eigenvalues of the Γ_n matrix and can be easily found by solving the roots of the unitary complex quartic equation in Appendix (II). B_n is a 4×4 matrix with its elements $b_{nij} = \Delta_{nij}/\Delta_{n1j}$, ($i$, j=1, 2,3,4) see Δ_{nij} in the Appendix (III). In general anisotropic or bi-anisotropic case, λ_{nj} (j=1,2,3,4) are two pairs of conjugate complex roots, which represent the type I and type II waves going in the positive and negative *z* directions [19]. And the column vectors of B_n are the corresponding eigenvectors. In isotropic cases, λ_{nj} (j=1, 2, 3, 4) are two identical pairs of conjugate complex roots and B_n has four linearly independent eigenvectors. So, B_n is always reversible in any case. $A_n = \left[a_1^{(n)},\ a_2^{(n)},\ a_3^{(n)},\ a_4^{(n)}\right]^T$ is the unknown column vector to be determined, in which $a_i^{(n)}$ (i=1, 2, 3, 4) are the unknown coefficients of the tangential fields in the *n*th layer. It can be seen from Eq. (6) that once the A_n is known, the tangential components of EM wave in the *n*th layer can be evaluated analytically.

III. DERIVATION OF THE EM FIELDS AND EQUIVALENT CURRENTS ON THE SURFACE OF STRATIFIED BIANISOTROPIC MEDIA BACKED BY A PEC LAYER

Imposing the boundary condition at the interface between the *nth* and (n+1) th layer that the tangential EM fields are continuous $\Psi_n(z=d_n) = \Psi_{n+1}(z=d_n)$, the following matrix equations can be derived

$$\begin{aligned} B_n E_{Rn} A_n &= B_{(n+1)} E_{L(n+1)} A_{(n+1)}, \\ E_{L(n+1)}^{-1} B_{(n+1)}^{-1} B_n E_{Rn} A_n &= A_{(n+1)}, \end{aligned} \tag{7}$$

where

$$\begin{aligned} E_{Rn} &= Diag[e^{\lambda_{n1}d_n}, e^{\lambda_{n2}d_n}, e^{\lambda_{n3}d_n}, e^{\lambda_{n4}d_n}], \\ E_{Ln} &= Diag[e^{\lambda_{n1}d_{n-1}}, e^{\lambda_{n2}d_{n-1}}, e^{\lambda_{n3}d_{n-1}}, e^{\lambda_{n4}d_{n-1}}]. \end{aligned} \tag{8}$$

By using the boundary condition at N-1 interfaces

(from $z = d_1$ to $z = d_{n-1}$) repeatedly, the relation of the tangential electric fields between the outmost and inmost layers can be derived as

$$E_{LN}^{-1}B_N^{-1}B_{(N-1)}E_{R(N-1)}\cdots E_{L2}^{-1}B_2^{-1}B_1E_{R1}A_1 = A_N. \tag{9}$$

On the surface of the PEC layer, tangential electric fields are naturally set to zero that $B_{N/2}E_{RN}A_N = 0$, in which $B_{N/2}$ is a 2×4 matrix with the elements from the first two rows of matrix B_N. Thus, we can get $C \times A_1 = 0$, where

$$C = B_{N/2}E_{RN}E_{LN}^{-1}B_N^{-1}B_{(N-1)}E_{R(N-1)}\cdots E_{L2}^{-1}B_2^{-1}B_1E_{R1} \tag{10}$$

is a 2×4 matrix.

From Maxwell's equations, the transverse EM fields in the left half free space can be expressed as the sum of the incident wave and the reflected wave

$$\begin{aligned}
&E_x(x,z) = E_x^+(x)e^{-jk_z z} + E_x^-(x)e^{jk_z z},\\
&E_y(x,z) = E_y^+(x)e^{-jk_z z} + E_y^-(x)e^{jk_z z},\\
&H_x(x,z) = \eta_1[-E_y^+(x)e^{-jk_z z} + E_y^-(x)e^{jk_z z}],\\
&H_y(x,z) = \eta_2[E_x^+(x)e^{-jk_z z} - E_x^-(x)e^{jk_z z}],
\end{aligned} \tag{11}$$

where $E_x^+(x) = E_{x0}^+e^{-jk_x x}$, $E_y^+(x) = E_{y0}^+e^{-jk_x x}$ are the transverse electric fields of incident wave at $z = d_0 = 0$, which are known, and $E_x^-(x) = E_{x0}^-e^{jk_x x}$, $E_y^-(x) = E_{y0}^-e^{jk_x x}$ are the reflected electric fields, which are unknown. $k_z = k_0\cos\theta$ is the incident field wave propagation vector in the z direction. $\eta_1 = \cos\theta/\eta_0$, $\eta_2 = 1/(\eta_0\cos\theta)$, $\eta_0 = 120\pi\,\Omega$ is the wave impedance in free space. By using the boundary condition that the tangential electric fields must be continuous across the interface (z=0) of free space and the outmost layer of the stratified bi-anisotropic media, the following matrix can be obtained

$$\begin{aligned}
&B_1E_{L1}A_1 = [E_x(x,z=0), E_y(x,z=0),\\
&H_x(x,z=0), H_y(x,z=0)]^T.
\end{aligned} \tag{12}$$

Considering Eqs. (10 and 12) and through some matrix operations, the unknown $E_x^-(x)$ and $E_y^-(x)$ can be expressed as

$$\begin{bmatrix} a_1^{(1)}\\ a_2^{(1)}\\ a_3^{(1)}\\ a_4^{(1)}\\ E_x^-(x)\\ E_y^-(x)\end{bmatrix} = Q^{-1}\begin{bmatrix} E_x^+(x)\\ E_y^+(x)\\ -\eta_1E_y^+(x)\\ \eta_2E_x^+(x)\\ 0\\ 0\end{bmatrix},$$

$$Q = \begin{bmatrix} b_{111} & b_{112} & b_{113} & b_{114} & -1 & 0\\ b_{121} & b_{122} & b_{123} & b_{124} & 0 & -1\\ b_{131} & b_{132} & b_{133} & b_{134} & 0 & -\eta_1\\ b_{141} & b_{142} & b_{143} & b_{144} & \eta_2 & 0\\ c_{11} & c_{12} & c_{13} & c_{14} & 0 & 0\\ c_{21} & c_{22} & c_{23} & c_{24} & 0 & 0\end{bmatrix}, \tag{13}$$

and c_{ij} (i=1,2;j=1,2,3,4) are the elements of matrix C in Eq.(10).

Finally, the relation between the incident and reflected tangential electric fields can be simplified as

$$\begin{bmatrix} E_x^-(x)\\ E_y^-(x)\end{bmatrix} = \begin{bmatrix} s_{11} & s_{12}\\ s_{21} & s_{22}\end{bmatrix}\begin{bmatrix} E_x^+(x)\\ E_y^+(x)\end{bmatrix}, \tag{14}$$

where

$$\begin{aligned}
&s_{11} = (q_1 + \eta_2 q_2)/|Q|, \qquad s_{12} = (q_3 + \eta_1 q_4)/|Q|,\\
&s_{21} = (q_5 + \eta_2 q_6)/|Q|, \qquad s_{22} = (q_7 + \eta_1 q_8)/|Q|,
\end{aligned}$$

and $q_j\,(j = 1,2\cdots 8)$ can be found in Appendix (III).

So far the reflected tangential EM fields on the surface of the outmost layer are obtained, which can be added to the incident fields to obtain the total tangential EM fields on the surface of the outmost layer. Thus, the equivalent EM currents can be derived as follows:

$$\begin{aligned}
&\vec{J}_s = \hat{n}\times\vec{H}_{total}\,|_{z=0} = \hat{y}[-s_{21}E_x^+(x)\\
&+(1-s_{22})E_y^+(x)]\eta_1\\
&+\hat{x}[(1-s_{11})E_x^+(x) - s_{12}E_y^+(x)]\eta_2,\\
&\vec{J}_{ms} = \vec{E}_{total}\times\hat{n}\,|_{z=0} = \hat{y}[(1+s_{11})E_x^+(x)\\
&+s_{12}E_y^+(x)]\eta_1 - \hat{x}[s_{21}E_x^+(x)\\
&+(1+s_{22})E_y^+(x)]\eta_2.
\end{aligned} \tag{15}$$

Equation (15) can also be written in the following general forms

$$\vec{J}_s = \hat{e}_\perp[-s_{21}E^i_{//}\cos\theta + (1-s_{22})E^i_\perp]\frac{\cos\theta}{\eta_0}$$
$$+\hat{e}_\omega[(1-s_{11})E^i_{//} - \frac{s_{12}}{\cos\theta}E^i_\perp]\frac{1}{\eta_0}, \quad (16)$$
$$\vec{J}_{ms} = \hat{e}_\perp[(1+s_{11})E^i_{//}\cos\theta + s_{12}E^i_\perp]$$
$$-\hat{e}_\omega[s_{21}E^i_{//}\cos\theta + (1+s_{22})E^i_\perp],$$

where $\hat{\hat{e}}_\omega = n \times e_\perp$, $E^i_{//}$ and $E^i_\perp$ are the incident electric fields those are parallel and perpendicular to the incidence plane, respectively, as shown in Fig. 1. Observing Eq. (16), the relations between $\vec{J}_s$ and $\vec{J}_{ms}$ can be expressed as

$$\vec{J}_{ms} = -\eta_0 \hat{n} \times (\bar{\bar{Z}}_s \cdot \vec{J}_s), \quad (17)$$

where

$$\bar{\bar{Z}}_s = Z_\perp \hat{\hat{e}}_\perp \hat{\hat{e}}_\perp + Z_{//} e_\omega e_\omega \quad (18)$$

is the normalized dyadic surface impedance to the free space and

$$Z_\perp = \frac{(1+s_{22})E^i_\perp + s_{21}E^i_{//}\cos\theta}{[(1-s_{22})E^i_\perp - s_{21}E^i_{//}\cos\theta]\cos\theta},$$
$$Z_{//} = \frac{[(1+s_{11})E^i_{//}\cos\theta + s_{12}E^i_\perp]\cos\theta}{(1-s_{11})E^i_{//}\cos\theta - s_{12}E^i_\perp}. \quad (19)$$

We remark that Eq. (16) - Eq. (19) give the final results of the equivalent EM currents on the surface of stratified homogeneous bi-anisotropic media backed with a PEC layer, which can be degenerated into the single anisotropic and isotropic cases easily.

Now, we consider the single anisotropic case when the PEC layer is coated with stratified uniaxial or biaxial anisotropic material and the permittivity $\bar{\bar{\varepsilon}}_n$ and permeability $\bar{\bar{\mu}}_n$ are diagonal matrixes

$$\bar{\bar{\varepsilon}}_n = \varepsilon_0 \times Diag[\varepsilon^r_{n11}, \varepsilon^r_{n22}, \varepsilon^r_{n3}],$$
$$\bar{\bar{\mu}}_n = \mu_0 \times Diag[\mu^r_{n11}, \mu^r_{n22}, \mu^r_{n3}]. \quad (20)$$

In this case, the matrix B_n can be simplified as [17, 18]

$$B_n = \begin{bmatrix} 1 & 1 & 0 & 0 \\ 0 & 0 & 1 & 1 \\ 0 & 0 & \frac{\lambda_{n3}}{\Gamma_{n23}} & \frac{\lambda_{n4}}{\Gamma_{n23}} \\ \frac{\lambda_{n1}}{\Gamma_{n14}} & \frac{\lambda_{n2}}{\Gamma_{n14}} & 0 & 0 \end{bmatrix}, \quad (21)$$

where Γ_{nij} (i, j=1,2,3,4) is the element of matrix Γ_n in Eq. (5).

If there is only one anisotropic layer, the following expressions can be obtained that

$$s_{11} = (Z_{//} - \cos\theta)/(Z_{//} + \cos\theta),$$
$$s_{22} = (Z_\perp \cos\theta - 1)/(Z_\perp \cos\theta + 1), \quad (22)$$
$$s_{12} = s_{21} = 0,$$
$$Z_{//} = j\sqrt{\mu^r_{22}\varepsilon^r_{33} - \sin^2\theta}$$
$$\tan(k_0 d\sqrt{\mu^r_{22}\varepsilon^r_{11} - \varepsilon^r_{11}\sin^2\theta/\varepsilon^r_{33}})/\sqrt{\varepsilon^r_{11}\varepsilon^r_{33}},$$
$$Z_\perp = j\sqrt{\mu^r_{11}\mu^r_{33}}$$
$$\tan(k_0 d\sqrt{\mu^r_{11}\varepsilon^r_{22} - \mu^r_{11}\sin^2\theta/\mu^r_{33}})/\sqrt{\mu^r_{33}\varepsilon^r_{22} - \sin^2\theta}. \quad (23)$$

Then Eq. (16) can be simplified as

$$\vec{J}_s = \hat{e}_\perp T_\perp E^i_\perp/(\eta_0 Z_\perp) + (\hat{\hat{n}} \times e_\perp)T_{//}E^i_{//}/(\eta_0 Z_{//}),$$
$$\vec{J}_{ms} = \hat{\hat{e}}_\perp T_{//}E^i_{//} - (n \times e_\perp)T_\perp E^i_\perp, \quad (24)$$

where $T_{//} = 2Z_{//}\cos\theta/(Z_{//} + \cos\theta)$, and $T_\perp = 2Z_\perp \cos\theta/(Z_\perp \cos\theta + 1)$.

Comparing Eq. (24) with the Eq. (17) and Eq. (18) in [14], we can observe that our generalized form of equivalent EM currents can be degenerated into the single anisotropic case naturally. By comparing Eq. (24) with Eq. (12) and Eq. (13) in [15], we can see that our results can also be degenerated into the isotropic case easily. This equivalent EM current can be employed for RCS prediction of coated targets in free space and half space [16].

IV. VALIDATION AND SIMULATION RESULTS

In this section, several simulation results are given for validation of the deduced analytical equivalent EM currents $\vec{J}_s$ and $\vec{J}_{ms}$. We remark

that only the four *s* parameters ($s_{11,}s_{12,}s_{21,}s_{22}$) are calculated for comparison considering that the *s* parameters are identical to $\vec{J}_s$ and $\vec{J}_{ms}$ if the incident fields are known based on Eq. (15).

First, we consider a two-layered isotropic lossy media case and a two-layered anisotropic lossy media case. The parameters of isotropic lossy case is as follows

$$d_1 = 0.002m,$$
$$\overline{\overline{\varepsilon}}_1 = \varepsilon_0 \times Diag[15 - j4, 15 - j4, 15 - j4]$$
$$\overline{\overline{\mu}}_1 = \mu_0 \times Diag[2 - j1.2, 2 - j1.2, 2 - j1.2];$$
$$d_2 = 0.006m,$$
$$\overline{\overline{\varepsilon}}_2 = \varepsilon_0 \times Diag[4 - j0.8, 4 - j0.8, 4 - j0.8]$$
$$\overline{\overline{\mu}}_2 = \mu_0 \times Diag[1.5 - j0.4, 1.5 - j0.4, 1.5 - j0.4];$$

and the parameters of the uniaxial anisotropic lossy case is as follows, the frequency is 10 GHz

$$d_1 = 0.002m,$$
$$\overline{\overline{\varepsilon}}_1 = \varepsilon_0$$
$$\times Diag[10 - j2, 10 - j2, 29.39 - j0.94],$$
$$\overline{\overline{\mu}}_1 = \mu_0$$
$$\times Diag[2.24 - j1.68, 2.24 - j1.68, 3.52 - j16];$$
$$d_2 = 0.006m,$$
$$\overline{\overline{\varepsilon}}_2 = \varepsilon_0$$
$$\times Diag[25.59 - j3.89, 25.59 - j3.89, 8.19 - j1.30],$$
$$\overline{\overline{\mu}}_2 = \mu_0$$
$$\times Diag[2.16 - j1.68, 2.16 - j1.68, 1.39 - j0.56];$$

In both of these two cases $s_{12} = s_{21} = 0$. When the incident wave is TE wave, $E_x^+(x) = 0$, $E_y^-(x) = s_{22}E_y^+(x)$, when the incident wave is TM wave, $E_y^+(x) = 0$, $E_x^-(x) = s_{11}E_x^+(x)$, the simulation results of the modulus and phase of s_{11}, s_{22} changed with the incident angle θ are shown in Fig. 2 and Fig. 3 for comparison with HFSS. It is obvious that our results agree quite well with those of HFSS and the analytical calculation in this paper takes no time while the numerical results obtained by HFSS takes more than 5 minutes even calculating one incident angle.

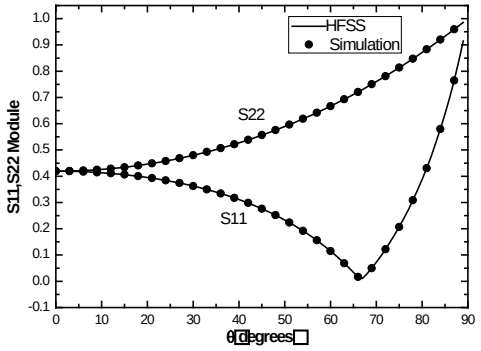

(a)

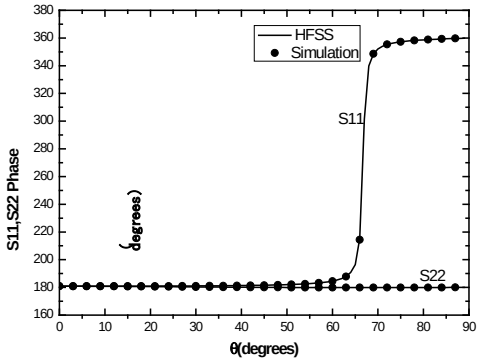

(b)

Fig. 2. Comparison of the *s* parameters (s_{11} and s_{22}) simulated in this paper with HFSS in the two layered lossy isotropic case. (a) Module and (b) phase.

Then, we consider a single layered bi-anisotropic case, the parameters are as follows, the frequency is 10 GHz,

$$d_1 = 0.006m,$$
$$\overline{\overline{\varepsilon}}_1 = \varepsilon_0 \times$$
$$Diag[25.59 - j1.68, 25.59 - j1.68, 8.19 - j1.30],$$
$$\overline{\overline{\mu}}_1 = \mu_0 \times$$
$$Diag[2.16 - j1.68, 2.16 - j1.68, 8.19 - j1.30],$$
$$\overline{\overline{\xi}}_1 = \sqrt{\varepsilon_0\mu_0} \times Diag[1.5 - j1.2, 1.5 - j1.2, 1 + j0.2],$$
$$\overline{\overline{\zeta}}_1 = \sqrt{\varepsilon_0\mu_0} \times Diag[1 - j0.8, 1 - j0.8, 1.1 - j0.5].$$

As shown in Fig. 4, s_{12} and s_{21} is not zero in this case for bi-anisotropic media is rotational, which causes cross polarization.

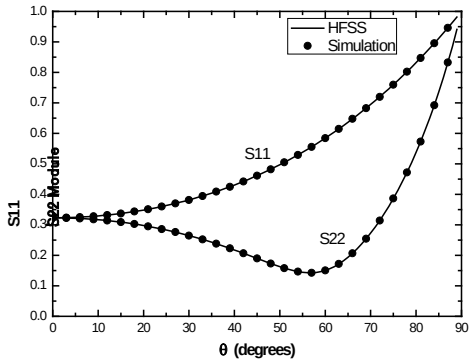

(a)

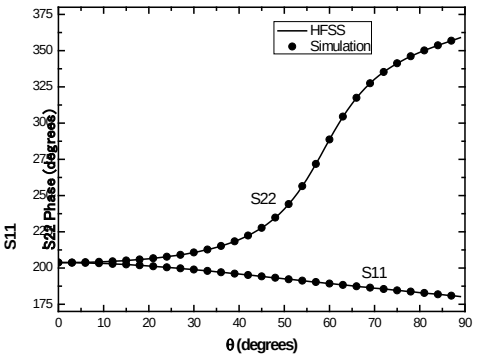

(b)

Fig. 3. Comparison of the *s* parameters (s_{11} and s_{22}) simulated in this paper with HFSS in the two layered lossy uniaxial anisotropic case. (a) Module and (b) phase.

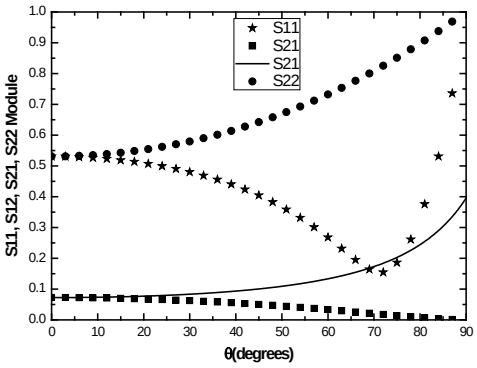

(a)

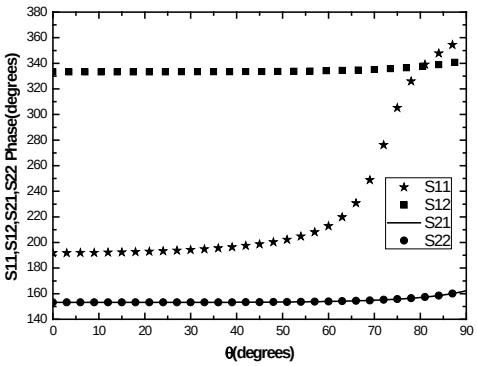

(b)

Fig. 4. The simulation results of the four s parameters (s_{11}, s_{12}, s_{21} and s_{22}) of the bi-anisotropic case. (a) Module and (b) phase.

V. CONCLUSIONS

In this work, the analytical expressions of equivalent EM currents on the surface of stratified homogeneous bi-anisotropic media backed by a PEC layer are derived, which can be degenerated into the single anisotropic and isotropic cases. Some simulation results are given to validate our conclusions. These equivalent currents are straight forward and very general for derivation and coding, which can be employed in the quick approximate estimation of EM scattering from electrically large PEC targets coated by stratified isotropic, anisotropic, or bi-anisotropic material.

VI. ACKNOWLEDGEMENT

The work is supported by the No. K201003 Foundation of State Key Laboratory of Millimeter Waves, Southeast University, P. R. China.

APPENDIX

APPENDIX (I)

$$\Gamma_{n11} = -j\omega\left(\begin{array}{l}\varsigma_{n21}+\varsigma_{n23}\dfrac{\xi_{n33}\varsigma_{n31}-\mu_{n33}\varepsilon_{n31}}{\mu_{n33}\varepsilon_{n33}-\xi_{n33}\varsigma_{n33}}\\ +\mu_{n23}\dfrac{\varepsilon_{n31}\varsigma_{n33}-\varsigma_{n31}\varepsilon_{n33}}{\mu_{n33}\varepsilon_{n33}-\xi_{n33}\varsigma_{n33}}\end{array}\right)$$

$$-jk_x\frac{\xi_{n33}\varsigma_{n31}-\mu_{n33}\varepsilon_{n31}}{\mu_{n33}\varepsilon_{n33}-\xi_{n33}\varsigma_{n33}}$$

$$\Gamma_{n12} =$$

$$-j\omega\left(\begin{array}{l}\varsigma_{n22}+\varsigma_{n23}\dfrac{\omega(\xi_{n33}\varsigma_{n32}-\mu_{n33}\varepsilon_{n32})-\xi_{n33}k_x}{\omega(\mu_{n33}\varepsilon_{n33}-\xi_{n33}\varsigma_{n33})}\\ +\mu_{n23}\dfrac{\omega(\varepsilon_{n32}\varsigma_{n33}-\varsigma_{n32}\varepsilon_{n33})+\varepsilon_{n33}k_x}{\omega(\mu_{n33}\varepsilon_{n33}-\xi_{n33}\varsigma_{n33})}\end{array}\right)$$

$$-jk_x\frac{\omega(\xi_{n33}\varsigma_{n32}-\mu_{n33}\varepsilon_{n32})-\xi_{n33}k_x}{\omega(\mu_{n33}\varepsilon_{n33}-\xi_{n33}\varsigma_{n33})}$$

$$\Gamma_{n13}=-j\omega\left(\begin{array}{l}\mu_{n21}+\mu_{n23}\dfrac{\varsigma_{n33}\xi_{n31}-\varepsilon_{n33}\mu_{n31}}{\mu_{n33}\varepsilon_{n33}-\xi_{n33}\varsigma_{n33}}\\ +\varsigma_{n23}\dfrac{\mu_{n31}\xi_{n33}-\xi_{n31}\mu_{n33}}{\mu_{n33}\varepsilon_{n33}-\xi_{n33}\varsigma_{n33}}\end{array}\right)$$

$$-jk_x\frac{\xi_{n33}\mu_{n31}-\mu_{n33}\xi_{n31}}{\mu_{n33}\varepsilon_{n33}-\xi_{n33}\varsigma_{n33}}$$

$$\Gamma_{n14}=$$

$$-j\omega\left(\begin{array}{l}\mu_{n22}+\mu_{n23}\dfrac{\omega(\varsigma_{n33}\xi_{n32}-\varepsilon_{n33}\mu_{n32})+\varsigma_{n33}k_x}{\omega(\mu_{n33}\varepsilon_{n33}-\xi_{n33}\varsigma_{n33})}\\ +\varsigma_{n23}\dfrac{\omega(\mu_{n32}\xi_{n33}-\xi_{n32}\mu_{n33})+\mu_{n33}k_x}{\omega(\mu_{n33}\varepsilon_{n33}-\xi_{n33}\varsigma_{n33})}\end{array}\right)$$

$$-jk_x\frac{\omega(\xi_{n33}\mu_{n32}-\mu_{n33}\xi_{n32})-\mu_{n33}k_x}{\omega(\mu_{n33}\varepsilon_{n33}-\xi_{n33}\varsigma_{n33})}$$

$$\Gamma_{n21}=j\omega\left(\begin{array}{l}\varsigma_{n11}+\varsigma_{n13}\dfrac{\xi_{n33}\varsigma_{n31}-\mu_{n33}\varepsilon_{n31}}{\mu_{n33}\varepsilon_{n33}-\xi_{n33}\varsigma_{n33}}\\ +\mu_{n13}\dfrac{\varepsilon_{n31}\varsigma_{n33}-\varsigma_{n31}\varepsilon_{n33}}{\mu_{n33}\varepsilon_{n33}-\xi_{n33}\varsigma_{n33}}\end{array}\right)$$

$$\Gamma_{n22}=$$

$$j\omega\left(\begin{array}{l}\varsigma_{n12}+\varsigma_{n13}\dfrac{\omega(\xi_{n33}\varsigma_{n32}-\mu_{n33}\varepsilon_{n32})-\xi_{n33}k_x}{\omega(\mu_{n33}\varepsilon_{n33}-\xi_{n33}\varsigma_{n33})}\\ +\mu_{n13}\dfrac{\omega(\varepsilon_{n32}\varsigma_{n33}-\varsigma_{n32}\varepsilon_{n33})+\varepsilon_{n33}k_x}{\omega(\mu_{n33}\varepsilon_{n33}-\xi_{n33}\varsigma_{n33})}\end{array}\right)$$

$$\Gamma_{n23}=j\omega\left(\begin{array}{l}\mu_{n11}+\mu_{n13}\dfrac{\mu_{n33}\varepsilon_{n31}-\varepsilon_{n33}\mu_{n31}}{\mu_{n33}\varepsilon_{n33}-\xi_{n33}\varsigma_{n33}}\\ +\varsigma_{n13}\dfrac{\mu_{n31}\xi_{n33}-\xi_{n31}\mu_{n33}}{\mu_{n33}\varepsilon_{n33}-\xi_{n33}\varsigma_{n33}}\end{array}\right)$$

$$\Gamma_{n24}=$$

$$j\omega\left(\begin{array}{l}\mu_{n12}+\mu_{n13}\dfrac{\omega(\varsigma_{n33}\xi_{n32}-\varepsilon_{n33}\mu_{n32})+\varsigma_{n33}k_x}{\omega(\mu_{n33}\varepsilon_{n33}-\xi_{n33}\varsigma_{n33})}\\ +\varsigma_{n13}\dfrac{\omega(\mu_{n32}\xi_{n33}-\mu_{n32}\xi_{n33})+\mu_{n33}k_x}{\omega(\mu_{n33}\varepsilon_{n33}-\xi_{n33}\varsigma_{n33})}\end{array}\right)$$

$$\Gamma_{n31}=j\omega\left(\begin{array}{l}\mu_{n21}+\mu_{n23}\dfrac{\xi_{n33}\varsigma_{n31}-\mu_{n33}\varepsilon_{n31}}{\mu_{n33}\varepsilon_{n33}-\xi_{n33}\varsigma_{n33}}\\ +\xi_{n23}\dfrac{\varepsilon_{n31}\varsigma_{n33}-\varsigma_{n31}\varepsilon_{n33}}{\mu_{n33}\varepsilon_{n33}-\xi_{n33}\varsigma_{n33}}\end{array}\right)$$

$$+jk_x\frac{\varepsilon_{n33}\varsigma_{n31}-\varsigma_{n33}\varepsilon_{n31}}{\mu_{n33}\varepsilon_{n33}-\xi_{n33}\varsigma_{n33}}$$

$$\Gamma_{n32}=$$

$$j\omega\left(\begin{array}{l}\varepsilon_{n22}+\varepsilon_{n23}\dfrac{\omega(\xi_{n33}\varsigma_{n32}-\mu_{n33}\varepsilon_{n32})-\xi_{n33}k_x}{\omega(\mu_{n33}\varepsilon_{n33}-\xi_{n33}\varsigma_{n33})}\\ +\xi_{n23}\dfrac{\omega(\varepsilon_{n32}\varsigma_{n33}-\varsigma_{n32}\varepsilon_{n33})-\varepsilon_{n33}k_x}{\omega(\mu_{n33}\varepsilon_{n33}-\xi_{n33}\varsigma_{n33})}\end{array}\right)$$

$$+jk_x\frac{\omega(\xi_{n33}\mu_{n32}-\mu_{n33}\xi_{n32})-\mu_{n33}k_x}{\omega(\mu_{n33}\varepsilon_{n33}-\xi_{n33}\varsigma_{n33})}$$

$$\Gamma_{n33}=j\omega\left(\begin{array}{l}\xi_{n21}+\xi_{n23}\dfrac{\varsigma_{n33}\xi_{n31}-\varepsilon_{n33}\mu_{n31}}{\mu_{n33}\varepsilon_{n33}-\xi_{n33}\varsigma_{n33}}\\ +\varepsilon_{n23}\dfrac{\mu_{n31}\xi_{n33}-\xi_{n31}\mu_{n33}}{\mu_{n33}\varepsilon_{n33}-\xi_{n33}\varsigma_{n33}}\end{array}\right)$$

$$+jk_x\frac{\varepsilon_{n33}\mu_{n31}-\varsigma_{n33}\xi_{n31}}{\mu_{n33}\varepsilon_{n33}-\xi_{n33}\varsigma_{n33}}$$

$$\Gamma_{n34}=$$

$$j\omega\left(\begin{array}{l}\xi_{n22}+\xi_{n23}\dfrac{\omega(\xi_{n32}\varsigma_{n33}-\mu_{n32}\varepsilon_{n33})+\varsigma_{n33}k_x}{\omega(\mu_{n33}\varepsilon_{n33}-\xi_{n33}\varsigma_{n33})}\\ +\varepsilon_{n23}\dfrac{\omega(\xi_{n33}\mu_{n32}-\xi_{n32}\mu_{n33})-\mu_{n33}k_x}{\omega(\mu_{n33}\varepsilon_{n33}-\xi_{n33}\varsigma_{n33})}\end{array}\right)$$

$$+jk_x\frac{\omega(\varepsilon_{n33}\mu_{n32}-\varsigma_{n33}\xi_{n32})-\varsigma_{n33}k_x}{\omega(\mu_{n33}\varepsilon_{n33}-\xi_{n33}\varsigma_{n33})}$$

$$\Gamma_{n41}=-j\omega\left(\begin{array}{l}\varepsilon_{n11}+\varepsilon_{n13}\dfrac{\xi_{n33}\varsigma_{n31}-\mu_{n33}\varepsilon_{n31}}{\mu_{n33}\varepsilon_{n33}-\xi_{n33}\varsigma_{n33}}\\ +\varepsilon_{n13}\dfrac{\varepsilon_{n31}\varsigma_{n33}-\varsigma_{n31}\varepsilon_{n33}}{\mu_{n33}\varepsilon_{n33}-\xi_{n33}\varsigma_{n33}}\end{array}\right)$$

$$\Gamma_{n42}=$$

$$-j\omega\left(\begin{array}{l}\varepsilon_{n12}+\varepsilon_{n13}\dfrac{\omega(\xi_{n33}\varsigma_{n32}-\mu_{n33}\varepsilon_{n32})-\xi_{n33}k_x}{\omega(\mu_{n33}\varepsilon_{n33}-\xi_{n33}\varsigma_{n33})}\\ +\xi_{n13}\dfrac{\omega(\varepsilon_{n32}\varsigma_{n33}-\varsigma_{n32}\varepsilon_{n33})+\varepsilon_{n33}k_x}{\omega(\mu_{n33}\varepsilon_{n33}-\xi_{n33}\varsigma_{n33})}\end{array}\right)$$

$$\Gamma_{n43} = -j\omega\begin{pmatrix}\xi_{n11}+\xi_{n13}\dfrac{\varsigma_{n33}\varepsilon_{n31}-\varepsilon_{n33}\mu_{n31}}{\mu_{n33}\varepsilon_{n33}-\xi_{n33}\varsigma_{n33}}\\ +\varepsilon_{n13}\dfrac{\mu_{n31}\xi_{n33}-\xi_{n31}\mu_{n33}}{\mu_{n33}\varepsilon_{n33}-\xi_{n33}\varsigma_{n33}}\end{pmatrix}$$

$$\Gamma_{n44} =$$

$$-j\omega\begin{pmatrix}\xi_{n12}+\xi_{n13}\dfrac{\omega(\varsigma_{n33}\xi_{n32}-\varepsilon_{n33}\mu_{n32})+\varsigma_{n33}k_x}{\omega(\mu_{n33}\varepsilon_{n33}-\xi_{n33}\varsigma_{n33})}\\ +\varepsilon_{n13}\dfrac{\omega(\mu_{n32}\xi_{n33}-\mu_{n33}\xi_{n32})-\mu_{n33}k_x}{\omega(\mu_{n33}\varepsilon_{n33}-\xi_{n33}\varsigma_{n33})}\end{pmatrix}$$

APPENDIX (II)

$$\lambda_n^4 - a_n\lambda_n^3 + b_n\lambda_n^2 + c_n\lambda_n + d_n = 0$$

$$a_n = \Gamma_{n11}+\Gamma_{n22}+\Gamma_{n33}+\Gamma_{n44}$$

$$b_n = \Gamma_{n11}\Gamma_{n44}-\Gamma_{n41}\Gamma_{n14}+\Gamma_{n22}\Gamma_{n44}$$
$$+\Gamma_{n33}\Gamma_{n44}-\Gamma_{n31}\Gamma_{n13}-\Gamma_{n42}\Gamma_{n24}+$$
$$\Gamma_{n22}\Gamma_{n11}+\Gamma_{n11}\Gamma_{n33}-\Gamma_{n32}\Gamma_{n23}+\Gamma_{n22}\Gamma_{n33}$$

$$c_n = \Gamma_{n32}\Gamma_{n23}\Gamma_{n44}+\Gamma_{n11}\Gamma_{n32}\Gamma_{n23}-\Gamma_{n11}\Gamma_{n22}\Gamma_{n33}$$
$$+\Gamma_{n41}\Gamma_{n22}\Gamma_{n14}+\Gamma_{n42}\Gamma_{n24}\Gamma_{n33}$$
$$+\Gamma_{n31}\Gamma_{n13}\Gamma_{n22}+\Gamma_{n31}\Gamma_{n13}\Gamma_{n44}$$
$$-\Gamma_{n11}\Gamma_{n22}\Gamma_{n44}-\Gamma_{n11}\Gamma_{n44}\Gamma_{n33}+\Gamma_{n11}\Gamma_{n42}\Gamma_{n24}$$
$$-\Gamma_{n22}\Gamma_{n33}\Gamma_{n44}-\Gamma_{n41}\Gamma_{n12}\Gamma_{n24}-\Gamma_{n42}\Gamma_{n23}\Gamma_{n34}$$
$$+\Gamma_{n41}\Gamma_{n14}\Gamma_{n33}-\Gamma_{n41}\Gamma_{n13}\Gamma_{n34}-\Gamma_{n31}\Gamma_{n12}\Gamma_{n23}$$

$$d_n = \Gamma_{n41}\Gamma_{n22}\Gamma_{n13}\Gamma_{n34}-\Gamma_{n41}\Gamma_{n22}\Gamma_{n14}\Gamma_{n33}$$
$$+\Gamma_{n11}\Gamma_{n22}\Gamma_{n33}\Gamma_{n44}-\Gamma_{n41}\Gamma_{n32}\Gamma_{n13}\Gamma_{n24}$$
$$+\Gamma_{n41}\Gamma_{n32}\Gamma_{n14}\Gamma_{n23}-\Gamma_{n31}\Gamma_{n13}\Gamma_{n22}\Gamma_{n44}$$
$$-\Gamma_{n11}\Gamma_{n32}\Gamma_{n23}\Gamma_{n44}+\Gamma_{n41}\Gamma_{n12}\Gamma_{n24}\Gamma_{n33}$$
$$+\Gamma_{n11}\Gamma_{n42}\Gamma_{n23}\Gamma_{n34}-\Gamma_{n11}\Gamma_{n42}\Gamma_{n24}\Gamma_{n33}$$
$$-\Gamma_{n41}\Gamma_{n12}\Gamma_{n23}\Gamma_{n34}+\Gamma_{n31}\Gamma_{n12}\Gamma_{n23}\Gamma_{n44}$$
$$+\Gamma_{n31}\Gamma_{n42}\Gamma_{n13}\Gamma_{n24}-\Gamma_{n31}\Gamma_{n42}\Gamma_{n14}\Gamma_{n23}$$

APPENDIX (III)

$$\Delta_{n1j} = \begin{vmatrix}\Gamma_{n12} & \Gamma_{n13} & \Gamma_{n14}\\ \Gamma_{n22}-\lambda_{n1} & \Gamma_{n23} & \Gamma_{n24}\\ \Gamma_{n32} & \Gamma_{n33}-\lambda_{n1} & \Gamma_{n34}\end{vmatrix},$$

$$\Delta_{n2j} = \begin{vmatrix}\lambda_{n2}-\Gamma_{n11} & \Gamma_{n13} & \Gamma_{n14}\\ -\Gamma_{n21} & \Gamma_{n23} & \Gamma_{n24}\\ -\Gamma_{n31} & \Gamma_{n33}-\lambda_{n2} & \Gamma_{n34}\end{vmatrix},$$

$$\Delta_{n3j} = \begin{vmatrix}\Gamma_{n12} & \lambda_{n3}-\Gamma_{n11} & \Gamma_{n14}\\ \Gamma_{n22}-\lambda_{n3} & -\Gamma_{n21} & \Gamma_{n24}\\ \Gamma_{n32} & -\Gamma_{n31} & \Gamma_{n34}\end{vmatrix},$$

$$\Delta_{n4j} = \begin{vmatrix}\Gamma_{n12} & \Gamma_{n13} & \lambda_{n4}-\Gamma_{n11}\\ \Gamma_{n22}-\lambda_{n4} & \Gamma_{n23} & -\Gamma_{n21}\\ \Gamma_{n32} & \Gamma_{n33}-\lambda_{n4} & -\Gamma_{n31}\end{vmatrix}.$$

APPENDIX (IV)

$$q_1 = \begin{vmatrix}b_{121} & b_{122} & b_{123} & b_{124} & -1\\ b_{131} & b_{132} & b_{133} & b_{134} & -\eta_1\\ b_{141} & b_{142} & b_{143} & b_{144} & 0\\ c_{11} & c_{12} & c_{13} & c_{14} & 0\\ c_{21} & c_{22} & c_{23} & c_{24} & 0\end{vmatrix},$$

$$q_2 = \begin{vmatrix}b_{111} & b_{112} & b_{113} & b_{114} & 0\\ b_{121} & b_{122} & b_{123} & b_{124} & -1\\ b_{131} & b_{132} & b_{133} & b_{134} & -\eta_1\\ c_{11} & c_{12} & c_{13} & c_{14} & 0\\ c_{21} & c_{22} & c_{23} & c_{24} & 0\end{vmatrix},$$

$$q_3 = -\begin{vmatrix}b_{111} & b_{112} & b_{113} & b_{114} & 0\\ b_{131} & b_{132} & b_{133} & b_{134} & -\eta_1\\ b_{141} & b_{142} & b_{143} & b_{144} & 0\\ c_{11} & c_{12} & c_{13} & c_{14} & 0\\ c_{21} & c_{22} & c_{23} & c_{24} & 0\end{vmatrix},$$

$$q_4 = \begin{vmatrix}b_{111} & b_{112} & b_{113} & b_{114} & 0\\ b_{121} & b_{122} & b_{123} & b_{124} & -1\\ b_{141} & b_{142} & b_{143} & b_{144} & 0\\ c_{11} & c_{12} & c_{13} & c_{14} & 0\\ c_{21} & c_{22} & c_{23} & c_{24} & 0\end{vmatrix},$$

$$q_5 = -\begin{vmatrix} b_{121} & b_{122} & b_{123} & b_{124} & 0 \\ b_{131} & b_{132} & b_{133} & b_{134} & 0 \\ b_{141} & b_{142} & b_{143} & b_{144} & \eta_2 \\ c_{11} & c_{12} & c_{13} & c_{14} & 0 \\ c_{21} & c_{22} & c_{23} & c_{24} & 0 \end{vmatrix},$$

$$q_6 = \begin{vmatrix} b_{111} & b_{112} & b_{113} & b_{114} & -1 \\ b_{121} & b_{122} & b_{123} & b_{124} & 0 \\ b_{131} & b_{132} & b_{133} & b_{134} & 0 \\ c_{11} & c_{12} & c_{13} & c_{14} & 0 \\ c_{21} & c_{22} & c_{23} & c_{24} & 0 \end{vmatrix},$$

$$q_7 = \begin{vmatrix} b_{111} & b_{112} & b_{113} & b_{114} & -1 \\ b_{131} & b_{132} & b_{133} & b_{134} & 0 \\ b_{141} & b_{142} & b_{143} & b_{144} & \eta_2 \\ c_{11} & c_{12} & c_{13} & c_{14} & 0 \\ c_{21} & c_{22} & c_{23} & c_{24} & 0 \end{vmatrix},$$

$$q_8 = \begin{vmatrix} b_{111} & b_{112} & b_{113} & b_{114} & -1 \\ b_{121} & b_{122} & b_{123} & b_{124} & 0 \\ b_{141} & b_{142} & b_{143} & b_{144} & \eta_2 \\ c_{11} & c_{12} & c_{13} & c_{14} & 0 \\ c_{21} & c_{22} & c_{23} & c_{24} & 0 \end{vmatrix}.$$

REFERENCES

[1] A. Taflove and M. E. Brodwin, "Numerical Solution of Steady-State Electromagnetic Scattering Problems using the Time-Dependent Maxwell's Equations," *IEEE Transaction on Microwave Theory Technology*, MTT-23, pp. 623-630, 1975.

[2] A. Taflove and K. R. Umashankar, "Radar Cross Section of General Three-Dimensional Scatters," *IEEE Transaction Electromagnetic Compatibility*, MTT-23, pp. 623-630, 1975.

[3] J. Schneider and S. Hudson, "The Finite-Difference Time-Domain Method Applied to Anisotropic Material," *IEEE Transaction on Antennas and Propagation*, vol. 41, no. 7, pp. 994-999, 1993.

[4] V. V. Varadan, A. Lakhtakia, and V. K. Varadan, "Scattering by Three-Dimensional Anisotropic Scatters," *IEEE Transaction on Antennas and Propagation*, vol. 37 no. 6, pp. 800-802, 1989.

[5] R. D. Graglia, P. L. E. Uslenghi, and R. S. Zich, "Moment Method with Isoparametric Elements for Three-Dimensional Anisotropic Scatters," *Proceedings of the IEEE*, vol. 77, no. 5, pp. 750-760, 1989.

[6] F. Abelès, Ann Phy. (Paris) vol. 5, pp. 596-640, 1950.

[7] S. Teitler and B. W. Henvis, "Refraction in Stratified, Anisotropic Media," *J. Opt. Soc. Am.* vol. 60, no. 6, pp. 830-834, June 1970.

[8] D. W. Berreman, "Optics in Stratified and Anisotropic Media: 4×4 Matrix Formulation," *J. Opt. Soc. Am.* vol. 62, no. 4, pp. 502-510, Apr. 1972.

[9] R. D. Graglia and P. L. E. Uslenghi, "Electromagnetic Scattering from Anisotropic Materials, Part I: General Theory," *IEEE Trans.Ant.Progat.*, vol. AP-32, no. 8, pp. 867-869, Aug. 1984.

[10] M. A. Morgan, "Electromagnetic Scattering by Stratified Inhomogeneous Anisotropic Media," *IEEE Transaction on Antennas and Propagation*, vol. AP-35, no. 2, pp. 191-197, 1987.

[11] L. M. Barkovskii and G. N. Borzdov, "Electromagnetic Wave in Absorbing Plane-Layered Anisotropic and Gyrotropic Media," *J. App. Spectrosc.*, vol. 23, no. 1, pp. 985-991, Sept. 1976.

[12] L. M. Barkovskii and G. N. Borzdov, "Reflection of Electromagnetic Waves from Layered Continuously Inhomogeneous Anisotropic Media: Multiple Reflection Method," *Opt. Spectosc. (USSR)*, vol. 45, no. 4, pp. 701-705, 1978.

[13] L. M. Barkovskii, "Construction of Input Wave Impedance of Layered Anisotropic Media by the Direct Tensor Method," *Sov. Phys. Crystallogr*, vol. 23, no. 6 pp. 647-650.

[14] P. K. Huang and H. C. Yin, "Equivalent Currents on an Anisotropic Material Backed by a Metal Surface and their Relation," *Journal of Systems Engineering and Electronics*, vol. 11, no. 4, pp. 1-10, 2000.

[15] P. Corona, "Backscattering by Loaded and Unloaded Dihedral Corners," *IEEE Transaction on Antennas and Propagation*, vol. 35, no. 10, pp. 1148-1153, 1987.

[16] X. F. Li, Y. J. Xie, R. Yang, and Y. Y. Wang, "High-Frequency Analysis of Scattering from Complex Targets in Half Space," *Applied*

Computational Electromagnetic Society (ACES) Journal, vol. 25, no. 5, pp. 433-443, 2010.

[17] L. Zhao, Y. Zuo, and Y. J. Feng, "Electromagnetic Wave Reflection of Anisotropic Media with a Metallic Substrate," *Chinese Journal of Radio Science,* vol. 24, no. 5, pp. 804-807, 2009.

[18] H. P. Guo, G. X. Liu, H. C. Yin, and P. K. Huang, "Analytical Expression of Equivalent Currents on Stratified Anisotropic Material Backed by Metal Surface," *Chinese Journal of Radio Science*. vol. 17, no. 6, pp. 605-608, 2002.

[19] W. C. Chew, *Wave and Fields in Inhomogeneous Media,* IEEE Press, 2nd, New York, 1995.

FEKO-Based Method for Electromagnetic Simulation of Carcass Wires Embedded in Vehicle Tires

Nguyen Quoc Dinh[1], Takashi Teranishi[1], Naobumi Michishita[1], Yoshihide Yamada[1], and Koji Nakatani[2]

[1] Department of Electrical and Electronic Engineering, National Defense Academy
1-10-20 Hashirimizu, Yokosuka, Kanagawa 239-8686, Japan
g47098@nda.ac.jp, naobumi@nda.ac.jp, yyamada@nda.ac.jp

[2] The Yokohama Rubber Co., Ltd.
2-1 Oiwake, Hiratsuka, Kanagawa 254-8601, Japan
k.nakatani@mta.yrc.co.jp

Abstract ─ In a tire pressure monitoring system in which a pressure censor and a transmit antenna are contained in a tire, electromagnetic simulations of radiations from carcass embedded tires are requested. However, it is difficult to accurately determine these shielding effects.

In this study, methods for performing accurate electromagnetic simulation by adopting the MoM scheme are determined. In the study of the electric fields inside a tire, calculated results are compared with the theoretical distributions in a coaxial cylindrical resonator. In the case of a dense carcass arrangement, simulation results are in good agreement with theoretical results. In the study of electric fields penetrating carcass wires, the results of the MoM scheme are compared with those obtained using the finite element method (FEM). The adequate mesh size of the tire rubber in the MoM scheme for which the accuracy of the simulation results is guaranteed is established. Finally, electromagnetic simulations of an actual carcass tire model are performed.

Index Terms ─ Carcass tire, method of moment, normal-mode helical antenna, tire pressure monitoring system, tire rubber.

I. INTRODUCTION

In order to ensure safety in cars, tire pressure monitoring systems (TPMSs) have been introduced in the USA and Europe [1]. In Japan, the AIRwatch system for passenger cars has been developed [2, 3] by The Yokohama Rubber Co., Ltd. However, in the case of large vehicles, tires are reinforced by carcass wires. In such cases, the transmission of radio waves becomes very difficult. Therefore, a small normal-mode helical antenna (NMHA) that has a high antenna gain was developed [4]. In order to develop an efficient TPMS for carcass tires, the electric field distributions inside the tire and the radiation characteristics need to be determined by performing electromagnetic simulation. However, the structure of a tire rubber with densely embedded carcass wires is difficult to simulate in method of moment (MoM) simulations. Although, the NECBSC code seems effective [5], authors selected the FEKO simulator because of the excellent ability of simulations for large scale objects.

In this study, the accuracy of the simulation of the effects of carcass wires in tire rubber is determined by comparing simulation results with exact values. In section II, an outline of the TPMS, a simulation model of a carcass tire, and the electric characteristics of the NMHA are summarized. In section III, the accuracies of the simulation of the shielding effects of carcass wires are discussed by adopting the theoretical electric fields in a coaxial cylindrical resonator as an exact reference. In section IV, the accuracies of MoM simulations of the effects of tire rubber on electric field distributions are discussed by comparing MoM results with the accurate results obtained by using the finite element method (FEM). In section V, simulation results for an actual carcass tire model are shown. The computational costs of simulation, electric field

distributions around a tire, and radiation characteristics from a tire are presented.

II. OBJECTIVE SYSTEM AND SIMULATION MODEL

The AIRwatch system is illustrated in Fig. 1 [3]. Transmitters connected to tire pressure sensors are mounted on the wheels. A receiver unit is placed on the dashboard. A receiving antenna (film antenna) is attached to the windshield. Each of the sensors modulates continuous waves of 315 MHz with air pressure data using a frequency shift keying (FSK) scheme. The modulated waves are radiated from a transmit antenna in the sensor. The receiving antenna collects all the transmitted waves. The pressure levels are indicated on the receiver unit.

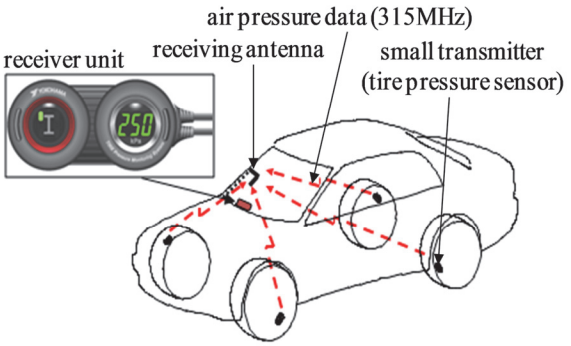

Fig. 1. The AIRwatch system.

The structure of the carcass tire to be analyzed and the position of the antenna in the tire are shown in Fig. 2. In an actual tire, a dense-mesh reinforcing structure called a tire belt is embedded in the tread of the tire. In the simulation, the model has a thin metal plate instead. Moreover, tires of large-sized vehicles are equipped with thin wires, called carcass, to reinforce the radial directions. The antenna inside the tire is almost enclosed by metal structures. The area within the broken lines corresponds to the tire model of Fig. 11, which is used to study the rubber effects.

Figure 3 shows the NMHA, which is used as the transmitting antenna [4]. This antenna is well known for having an electric current source (I) and a magnetic current source (J), as indicated in the figure. The magnetic current source achieves efficient radiations in a metal proximity use. Radiated electric field components from the magnetic and electric current sources are indicated by E_J and E_I, respectively. In order to contain this antenna inside a transmitter box, antenna size of 12.5 mm (0.01 wavelengths) diameter is determined. Since the input impedance becomes very small, a tap structure has been added to the NMHA in order to achieve impedance matching at 50 Ω.

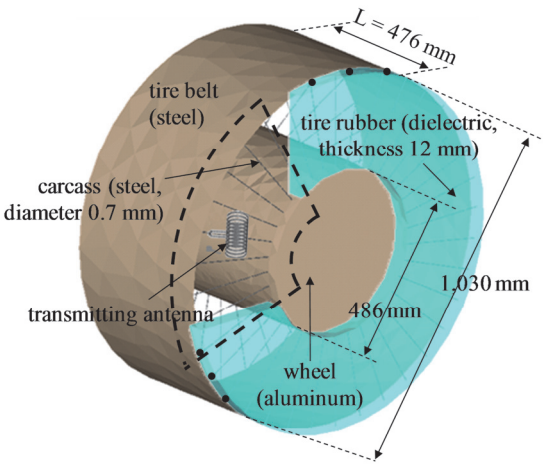

Fig. 2. Structure of a carcass tire.

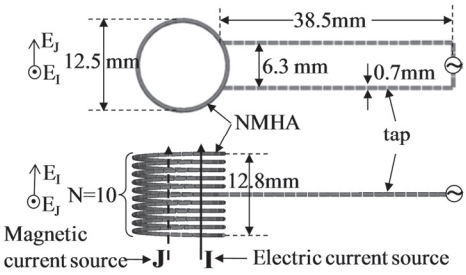

Fig. 3. Structure of a NMHA.

Radiation characteristics of the NMHA on a small metal plate are shown in Fig. 4. The tap is positioned opposite the metal plate. The E_J component becomes dominant. Antenna gain of -12.3 dBd (relative value to the half wave length dipole antenna) is achieved. A rather high antenna efficiency is achieved.

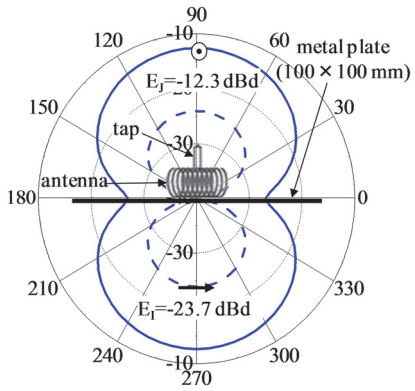

Fig. 4. Radiation characteristics of a NMHA.

III. SHIELDING EFFECTS BY CARCASS WIRES

A. Electric fields inside a tire

By taking into account the tire structure of Fig. 2, electric fields inside a tire are determined by metallic boundary conditions of a tire belt, wheel, and carcass [6]. Moreover, the tire rubber will affect the field distributions. In this section, affects of carcass are mainly investigated as the first step. Therefore, the rubbers are removed in the calculations. In order to evaluate the accuracy of the determined effects of carcass wires, the electric fields inside the tire were compared with that of a coaxial cylindrical resonator of a similar size to the tire. The structure shown in Fig. 2 is employed as the tire model in the simulation. The MoM code of FEKO is used. The structure of the cylindrical resonator is shown in Fig. 5. The outer and inner cylinders and the two side plates are all made of metals. In the sizes of actual tires, electric fields characterized by TEM and TE_{111} modes are dominant inside the coaxial cylinders. In particular, the TEM mode is the simplest because it only has radial electric field vectors. On the other hand, the TE_{111} mode has complex electric field vectors of radial and circumferential components. To determine if the simulation is adequate, it is appropriate to use the TEM mode. The resonance frequency of the TEM mode is given by the following equation.

$$L = s\lambda_0 / 2, \qquad (1)$$

where s is the mode variable. When s = 1, L = 475.8 mm gives a resonance frequency of 315 MHz.

A detailed view of the theoretical electric field distributions in the TEM mode is shown in Fig. 6. Here, R_1 = 515.0 mm and R_2 = 242.8 mm were used. In Fig. 6(a), all the electric field vectors are directed toward the radial directions. In Fig. 6(b), the electric fields vanish at the side plates. The electric field distributions inside the carcass tire are shown in Figs. 7 and 8. Figures 7 and 8 correspond to 288 and 36 carcass wires, respectively. In Fig. 7(a), the electric field vectors agree well with those in Fig. 6(a). In Fig. 7(b), the electric fields are confined to the inside of the tire. As for field intensities indicated beside the tire, electric fields on carcass wires become almost zero. This distribution agrees well with that in Fig. 6(b). Therefore, in this carcass number, carcass wires function like a complete shielding wall, which is the same as the side plate in Fig. 6.

In Fig. 8(a), deformations of the electric field vectors are observed. In Fig. 8(b), expansion of the electric fields outside the tire is observed. In electric field intensities indicated beside the tire, intensities on the carcass wire do not vanish. Electrical field distributions in the case of sparse carcasses seem reasonable.

In conclusion, the simulation results inside the carcass tire are considered adequate.

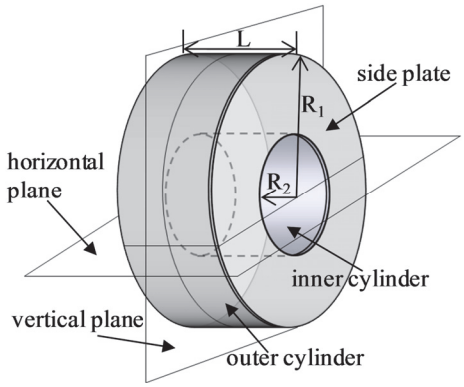

Fig. 5. Structure of a coaxial cylindrical resonator.

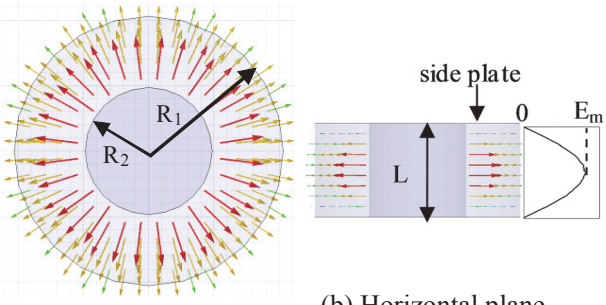

(a) Vertical plane. (b) Horizontal plane.

Fig. 6. Theoretical electric field distributions in the TEM mode.

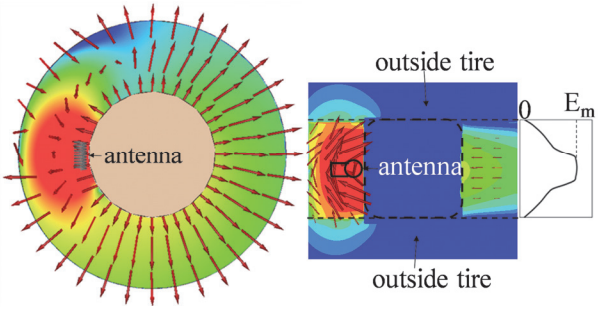

(a) Vertical plane. (b) Horizontal plane.

Fig. 7. Electric field distributions inside the tire (carcass wires: 288).

B. Radiation from a tire

The tire rubber is excluded from the structure shown in Fig. 2, and this structure is employed as the tire model in the simulation [6]. The MoM

code of FEKO is used. Radiation characteristics from a tire are shown in Fig. 9. In Fig. 9(a), a tire without carcass is shown. The electric fields in the TEM mode radiate through the apertures of the tire. The main beams exist in the direction of the Y axis. The maximum power becomes -4.2 dBd. In the direction of the X axis, a fairly strong beam is observed. Figure 9(b) shows a case where the number of carcass wires is 288. The main beam decreases by 32.5 dB. Figure 9(c) shows a case where the number of carcass wires is 36. The main beam decreases by 14.4 dB. Because the main beams in Figs. 9 (a), (b), and (c) are directed toward the Y axis, the powers at the receiving antenna, as depicted in Fig. 1, will deviate in accordance with the tire rotation. Actually, the severe fading caused by surrounding reflections is taken into account in the system design. The level deviation based on tire rotations will be taken into account as one of the fading factors. Antenna input impedances in the case of Fig. 9 are shown in Fig. 10. It is clarified that input impedances are not influenced by the presence of carcass wires.

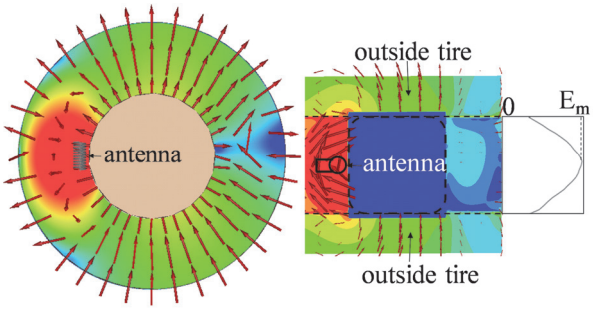

(a) Vertical plane. (b) Horizontal plane.

Fig. 8. Electric field distributions inside the tire (carcass wires: 36).

IV. SIMULATION METHOD OF A DIELECTRIC PLATE WITH EMBEDDED CARCASS WIRES

As for the structure of a dielectric plate with carcass wires inside, there were no study examples in FEKO simulation. Therefore, it is very important to ensure that the simulation is accurate. In order to investigate the fundamental effect of rubber, the effect on the electric field penetrations through carcass wires are considered. When the model shown in Fig. 2 is used in the calculation, the calculation load is very high. The simplified model shown in Fig. 11 that corresponds to the area within the broken lines in Fig. 2 is constructed. As for the radiator, a very small dipole antenna placed inside tire is employed for ease of calculation. This antenna is oriented in order to produce the E_J field component of Fig. 4 (parallel to the carcass wire). In accordance with the parallel electric field vectors, carcass wires are arranged in parallel wires of separations s. The observation planes are set perpendicular to the carcass wires. In order to eliminate the effects of edge currents, rather large values were selected for the sizes of the tire belt and wheel.

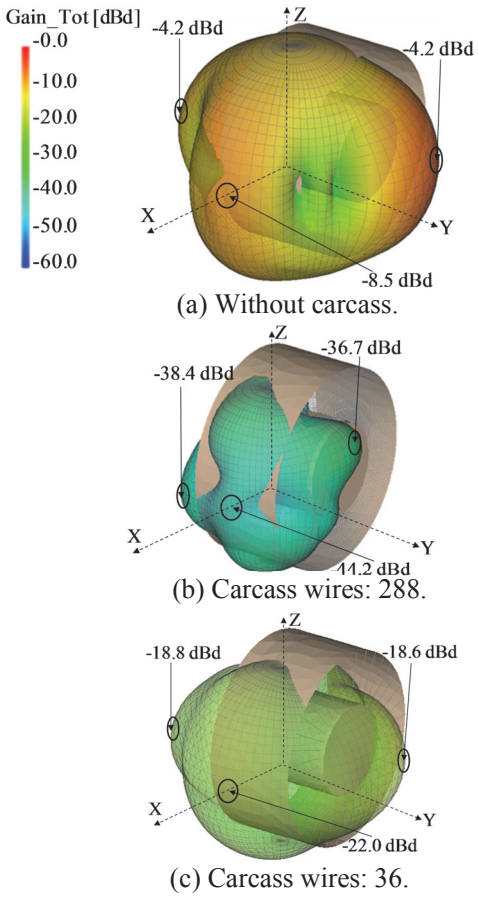

(a) Without carcass.

(b) Carcass wires: 288.

(c) Carcass wires: 36.

Fig. 9. Radiation characteristics from a tire (without rubber).

To assess the adequacy of the calculations, results obtained with MoM are compared with those obtained via FEM. Usually, the FEM results were considered to be the correct results. Comparisons of results are summarized in Table 1.

Firstly, the shielding effects of carcass wires are clearly shown by the HFSS simulation results. In the case where rubber was removed, electric fields passing through spaces between the wires gradually fade toward the outside. This result agrees very well with the physical behavior of parallel wires. Therefore, the HFSS result can be

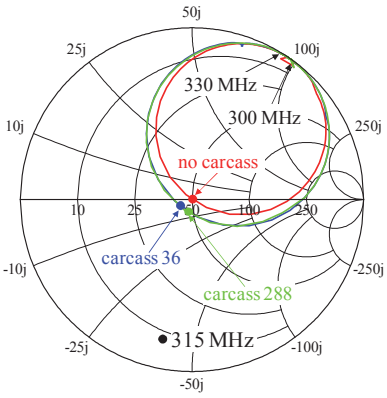

Fig. 10. Input impedance of the NMHA.

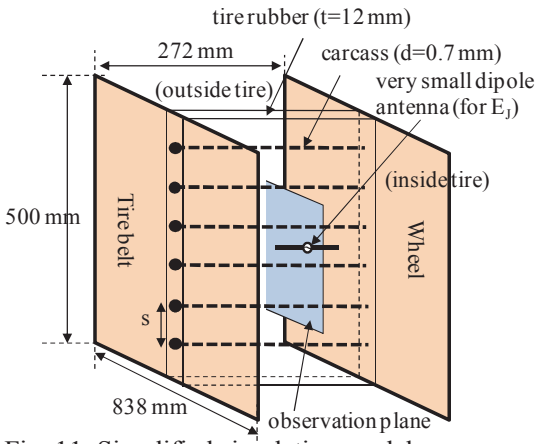

Fig. 11. Simplified simulation model.

Table 1: Electric field distributions in the observation plane

		Electric intensity distribution (dBV/m)	Computation costs
FEM (HFSS)	Without rubber	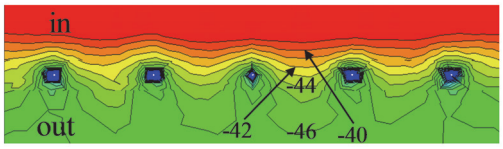	memory: 3.5 GB time: 1631 sec element size of air space between carcasses : λ/75
	With rubber (thickness= 12 mm, ε_r = 10.91 tanδ = 0.14)	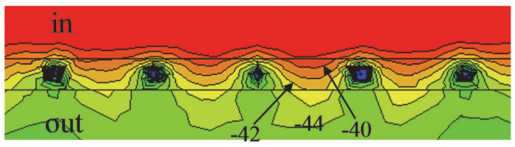	memory: 3.3 GB time: 1634 sec element size of rubber : λ/75
FEM (FEKO)	With rubber (thickness=12 mm, ε_r = 10.91 tanδ = 0.14)	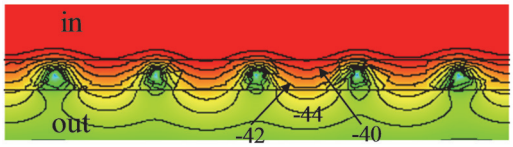	memory: 6.8 GB time: 18,889 sec element size of rubber : λ/75
MoM (FEKO)	rubber mesh size : λ/25	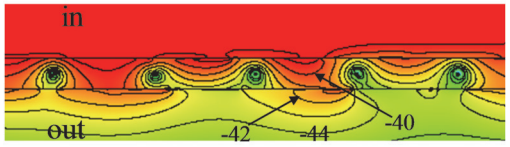	memory: 0.2 GB time: 4481 sec unknown: 4240 cell number: 2000
	rubber mesh size : λ/50	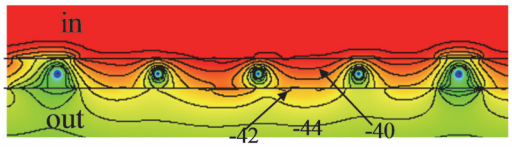	memory: 1.5 GB time: 7868 sec unknown: 10,079 cell number: 4156
	rubber mesh size : λ/75	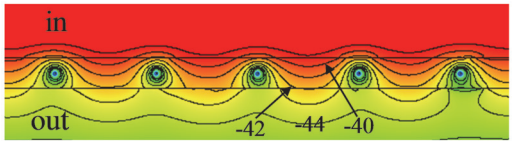	memory: 5.0 GB time: 16,696 sec unknown: 18,374 cell number: 6999

considered adequate. In the case where rubber was retained, electric field penetrations into the carcass wires seem to be enhanced. The electric field intensities at the outside increase by about 1 dB compared to their counterparts when rubber was removed. As a reference, the FEM result by FEKO is also obtained. Almost the same result to HFSS is achieved. On the basis of good agreement of FEM results by HFSS and FEKO, it is concluded that the FEM simulations are correct.

To assess the calculation accuracy of MoM, mesh sizes of the dielectric plate (tire rubber) are changed. In the FEKO simulation, the surface equivalent principle (SEP) algorithm is applied to dielectric plate calculations. In the case of mesh size λ/25, irregular electric field distributions are observed. For mesh size λ/75, almost regular electric field distributions are achieved. Data on electric field intensities are in good agreement with the results of HFSS. Therefore, it is concluded that accurate results can be achieved with a mesh size of λ/75.

V. SIMULATION RESULTS OF AN ACTUAL CARCASS TIRE

A. Fundamental data

As the example of an actual carcass tire, the structure of Fig. 2 is employed. Simulation parameters are summarized in Table 2. The most important parameter is mesh size. In particular, finding out the adequate mesh forms for tire rubbers requires a lot of thought. The result is shown in Fig. 12. Mesh configurations of the tire rubber are matched to the shapes of the spacing of wires. In circumferential directions, three small-sized meshes are used. In radial directions, rather large mesh sizes are selected. In this case, the number of wires used is 36. The wire spacing in the inner and outer rims are 42 and 90 mm, respectively. Observation planes indicated by A and B are oriented perpendicular to the wires.

Mesh sizes of the tire rubber are shown in Table 2. At the inner rim, mesh size λ/67 is selected. The unknown number becomes 17,644. Calculation time of more than 2 hours is needed. In this case, the number of carcass is only 36. In the actual tire, because a large number of carcass wires are used, a more efficient simulation method is required.

Electric field distribution at observation points A and B are shown in Fig. 13. In Fig. 13(a), electric fields outside the tire are suppressed by about 5 dB. In Fig. 13(b), electric field suppressions become 3 dB. In accordance with s increase, suppressions become small. These results are physically appropriate. Therefore, these calculated results are reliable.

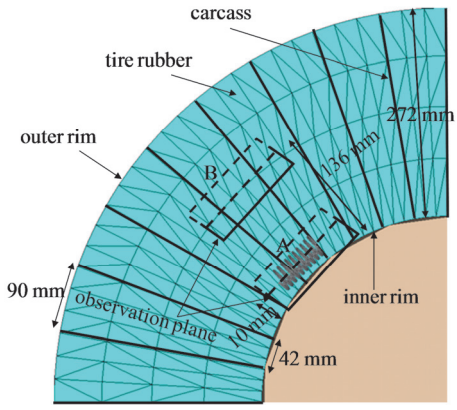

Fig. 12. Mesh configuration of tire rubber.

Table 2: Simulation parameters

CPU clock	Intel® Xeon® CPU 3.00 GHz		
memory	16.0 GB RAM		
simulator	FEKO (MoM)		
Frequency	315 MHz		
mesh sizes	Antenna		λ/600
	wheel	near antenna	λ/100
		other	λ/10
	tire belt		λ/10
	carcass (number, 36)		λ/15
	rubber (SEP method)	radial direction	λ/14
		inner rim	λ/67
		outer rim	λ/32
total mesh number	7,496		
unknown	17,644		
memory usage	2.33 Gbytes		
calculation time	7,571 seconds (2.1 hours)		

B. Electric wave characteristics

Electric field distributions and a radiation characteristic of a carcass tire are calculated. The electric fields inside the tire are shown in Fig. 14. These planes are just 1 mm inside the rubber inner surface. Electric fields with the rubber as shown in Fig. 14(b) become larger compared to those in Fig. 14(a). As for directions of electric field vectors, almost the same directions are achieved in strong field regions. However, small

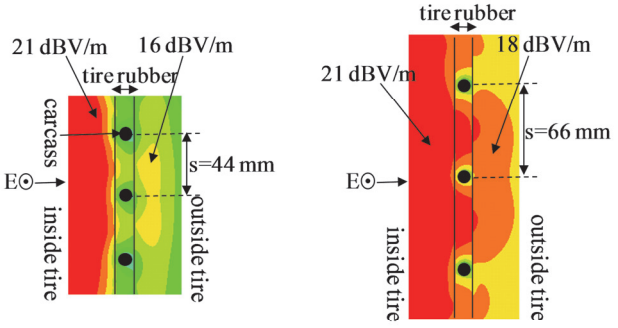

(a) Plane A. (b) Plane B.

Fig. 13. Electric fields at observation planes.

changes of vector directions are produced in weak field regions by the presence of the tire rubber. Next, electric fields in the cross-sectional planes of the tire are shown in Fig. 15. In comparing Fig. 15(a) and (b), the electric fields spilling over to the outside of a tire are increased as a rubber effect. Finally, the radiation power levels of a carcass tire are shown in Fig. 16. The highest levels appear in the side of the tire, reaching a value of -15.6 dBd. This level is 3 dB larger than the result shown in Fig. 9(c). As a conclusion, the presence of rubber increases the electric fields inside a tire and the radiation levels from a tire. By taking into account that a tire rubber is a lossy material, the increase in radiation level is surprising.

VI. Conclusions

The accuracies of the simulation of electric fields in a carcass tire using the MoM scheme of FEKO are determined. The important contributions of this study are as follows:

1) The electric fields inside a tire are compared with those of a coaxial cylindrical resonator chosen as theoretical references.
2) FEM- and MoM-based methods for determining the effect of wires embedded in a dielectric plate are investigated.
3) The adequate mesh sizes of the tire rubber in MoM are determined.
4) Adequate mesh configurations of the tire rubber between carcass wires are developed.
5) By using an actual carcass tire model, the electric fields inside a tire and the characteristics of radiation from a tire are established.

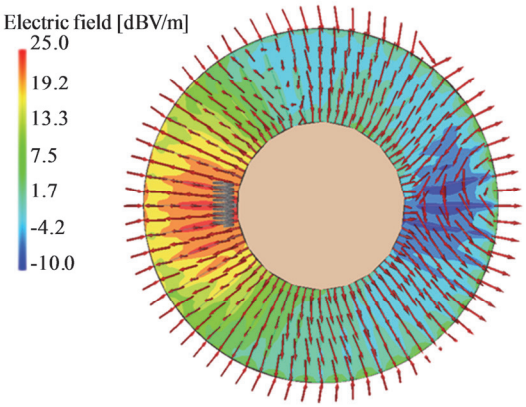

(a) Without rubber.

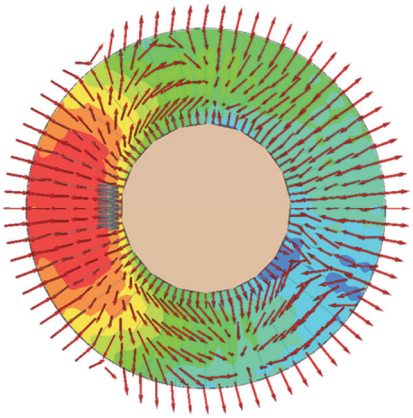

(b) With rubber.

Fig. 14. Electric field distributions inside the tire.

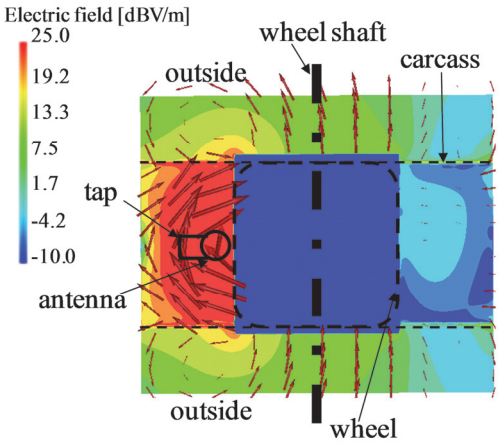

(a) Without rubber.

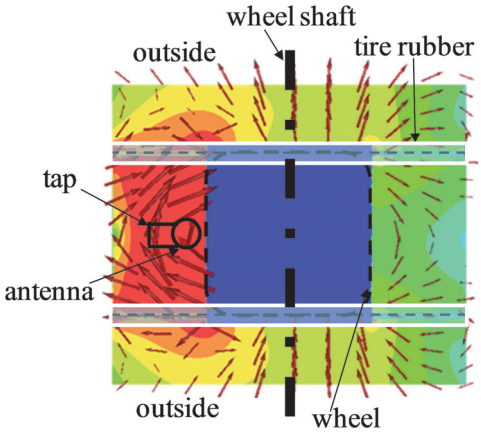

(b) With rubber.

Fig. 15. Electric field distributions in the cross-sectional planes.

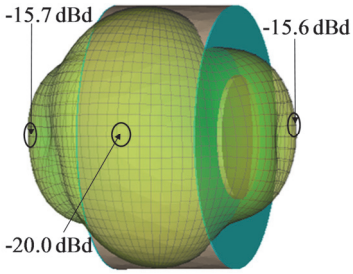

Fig. 16. Radiation pattern.

REFERENCES

[1] http://www.nhtsa.dot.gov/cars/rules/rulings/TPMSfinalrule.6/TPMSfinalrule.6.html

[2] http://www.yrc-pressroom.jp/html/200510717tr001.html

[3] K. Tanoshita, K. Nakatani, and Y. Yamada, "Electric Field Simulations Around a Car of the Tire Pressure Monitoring System," *IEICE Trans. Commun.*, vol. E90-B, no. 9, pp. 2416-2422, 2007.

[4] N. Q. Dinh, N. Michishita, Y. Yamada, and K. Nakatani, "Development of a Very Small Normal Mode Helical Antenna for the Tire Pressure Sensor of TPMS," *ISAP2008*, pp. 186-190, Oct. 2008.

[5] S. D. Walker and D. Chatterjee, "Study of Exact and High-Frequency Code Solvers for Applications to a Conformal Dipole Array," *Applied Computational Electromagnetic Society (ACES) Journal*, vol. 24, no. 6, pp. 550-558, 2009.

[6] N. Q. Dinh, T. Teranishi, N. Michishita, Y. Yamada, and K. Nakatani, "Electromagnetic Simulation Method of a Vehicle Tire Equipped with Carcass," *Applied Computational Electromagnetic Society (ACES) Conference*, session 5, Apr. 2010.

A Redundant Loop Basis for Closed Structures with Application to MR Basis

J. J. Ding [1, 2], R. S. Chen [1], J. Zhu [1], Z. H. Fan [1] and D. Z. Ding [1]

[1]Department of Electronic Engineering
Nanjing University of Science and Technology, Nanjing, 210094, China

[2]Antenna & Servo System Department
The 54th Research Institute of CETC, Shijiazhuang, 050081, China
draksea@yahoo.com, eerschen@mail.njust.edu.cn, zhujian82gogo@hotmail.com,
zhfan@mail.njust.edu.cn, dzding@mail.njust.edu.cn

Abstract ─ A redundant loop basis is proposed and applied as the solenoidal part of the recently developed multiresolution (MR) basis for closed surfaces at low frequencies. By keeping all loop basis functions, the "symmetry" of the MR solenoidal basis can be maintained for closed surfaces. As a consequence, the convergence of iterative solvers for the expanded MR basis can be effectively improved by using the redundant loop basis without disturbing the accuracy of results. Since the expanded MR basis functions are linear combinations of standard Rao-Wilton-Glisson (RWG) functions, it can be applied to the existing MoM codes easily. The positive behavior of redundant loop basis on MR basis for closed surfaces is analyzed and discussed in detail in this paper. Numerical results demonstrate that the expanded MR basis performs better than the original MR basis and has significant advantages over the traditional loop-tree basis for 3D electromagnetic scattering of closed structures in the low frequency range.

Index Terms ─ Electromagnetic scattering, low frequency, method of moments (MoM), multiresolution techniques.

I. INTRODUCTION

The method of moments (MoM) solution of the electric field integral equation (EFIE) is always preferred for analysis of 3D electromagnetic scattering problems [1]. However, the EFIE suffers from the low-frequency breakdown problem when using the well known Rao – Wilton–Glisson (RWG) basis [2], which is associated with the poorly-conditioned MoM matrix when the frequency tends to zero. As a consequence, the MoM matrix is hard to get convergence and even not solvable with iterative solvers. The solution to prevent the low-frequency breakdown problem is to extract the solenoidal part of the current [3-10], thus the loop-tree/star basis is proposed for this purpose. The multiresolution (MR) basis developed in recent years provides a more effective basis than the loop-tree/star basis [11-14]. More recently, an alternative MR basis was proposed for analysis of low-frequency problems [15, 16]. Compared with the MR basis in [11-14], the MR basis in [15, 16] can be constructed much easier and provides more direct physical meanings.

A simple and direct way of generating the solenoidal MR basis is taking the loop basis in the loop-tree/star basis as the solenoidal MR basis [12]. In the loop basis, each loop basis function corresponds to an interior vertex of surfaces. However, the loop basis is "asymmetry" for closed surfaces, since one loop associated to one arbitrary vertex must be eliminated. As pointed in [14], this "asymmetry" of loop basis for closed surfaces will cause the bad conditioning of the corresponding MoM matrix. To remedy the shortcoming of the loop basis, a novel, symmetrical solenoidal basis was proposed in [14]. The proposed solenoidal

basis is generated by applying the singular value decomposition (SVD) to local small "charge" matrices and it generates a well-conditioned MoM matrix. Alternatively, we propose a simple way to improve the conditioning of the loop basis for closed surfaces, i.e. taking a redundant loop basis as the solenoidal part of the MR basis. By keeping all loop basis functions, the "symmetry" of loop basis is kept. Also, as pointed in [18] that the redundant loop basis gives more freedom for the solution of flux to converge. Therefore, the application of the redundant loop basis to MR basis gives better convergence.

II. MULTIRESOLUTION BASIS

Due to the fact that MR basis possesses some degree of Fourier spectral resolution, the condition number of the corresponding MoM matrix can be drastically reduced with a diagonal preconditioning [17]. Therefore, MR basis has significant advantage than the classical loop-tree/star basis for analysis of low-frequency problems. Since the improvement of the MR basis in [15, 16] for closed surfaces is mainly concerned in this paper, the essential concepts of the MR basis are briefly described in this section.

A. Generalized mesh and generalized RWG basis

As proposed in [12], the generalized mesh and generalized RWG (gRWG) basis is the two basic concepts in generating the MR basis. The MR basis functions are constructed on the hierarchical generalized meshes and generated as the linear combinations of the gRWG basis functions. The hierarchical generalized meshes are generated via a grouping algorithm (e.g. a sophisticated algorithm in [13]) and starts from the level-0 mesh, i.e. the input triangular mesh. In the subsequent procedure of the grouping algorithm, each cell of level-l (l≥1) mesh is constructed by grouping about four near cells of level-(l-1) mesh. Finally, the mesh of the highest level is decided by the size of its cells, i.e. the size of the cells should be smaller than the wavelength of the incident EM wave. An example of four levels of hierarchical generalized meshes generated by the grouping algorithm is depicted in Fig. 1. The gRWG basis functions of each level are defined on the mesh of the corresponding level. Similar to the RWG basis function, each gRWG basis function of level-l mesh is defined on a pair of cells of level-l. Denoting a gRWG basis function of level-l with $\vec{R}_i^l(\vec{r})$, the divergence of the gRWG basis function is given as

$$\nabla_s \cdot \vec{R}_i^l(\vec{r}) = \begin{cases} \ell_i^l / A_{+,i}^l & \vec{r} \in C_{+,i}^l \\ -\ell_i^l / A_{-,i}^l & \vec{r} \in C_{-,i}^l \\ 0 & \text{otherwise,} \end{cases} \quad (1)$$

where $A_{+,i}^l$ and $A_{-,i}^l$ are the area of the two adjacent cells $C_{+,i}^l$ and $C_{-,i}^l$, and ℓ_i^l is the common side of the two cells.

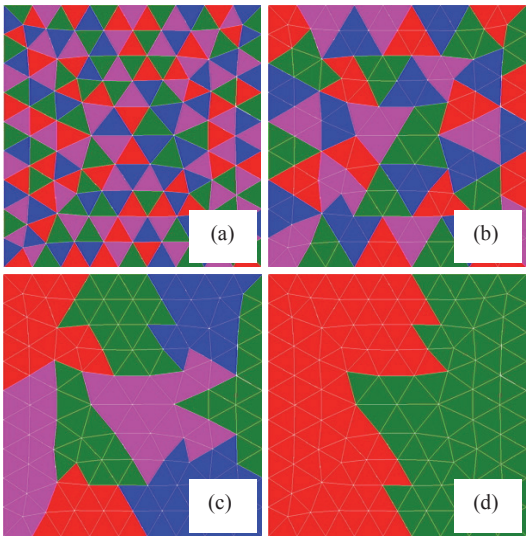

Fig. 1. An example of four levels hierarchical generalized meshes. (a) Level-0 mesh, (b) level-1 mesh, (c) level-2 mesh, (d) level-3 mesh.

B. Generation of MR basis

The MR basis is split into the solenoidal and nonsolenoidal parts. The solenoidal and nonsolenoidal functions of the MR basis span the same space as for the loop-tree/star basis. For a general 3-D surface, the number of solenoidal functions N_S and the number of nonsolenoidal functions N_X of the MR basis are given by [12, 16]

$$N_S = V_{\text{int}} + N_\Gamma - 1, \quad (2)$$

$$N_X = F - 1, \quad (3)$$

where V_{int}, N_Γ, F denote the number of internal vertices, separated boundary contours, and triangular faces, respectively. Obviously, the number of the solenoidal functions equals the number of the vertices minus one for closed surfaces.

1). Solenoidal Basis

A simple way of constructing the solenoidal part of the MR basis is taking the traditional loop basis as the solenoidal basis, since a non-hierarchical loop basis suffices to obtain well conditioned MoM matrices for low-frequency problems [12]. However, one loop basis function should be eliminated for closed surfaces according to (2).

2). Nonsolenoidal Basis

The nonsolenoidal part of MR basis is a hierarchical basis constructed on the hierarchical meshes. The nonsolenoidal basis first proposed in [12] is constructed via a rank-revealing QR decomposition. However, this approach requires the cells of the structure to be finally grouped into a single big cell. As a consequence, the regularizing property of the MR basis may be destroyed. To remedy this problem, a different approach is proposed in [13, 14], where the nonsolenoidal basis is constructed using SVD on small charge matrices and the cells of the highest level are smaller than the working wavelength. Nevertheless, the above approaches in generating of the MR basis rely on the indirect mathematical operations. Alternatively, a nonsolenoidal basis can be much easier to construct and comprehend in theory as proposed in [15, 16].

The generation of the nonsolenoidal functions of the highest level (level-L) is different from the functions of the other levels. Similar to the generation of the tree basis in the classical loop-tree basis, the nonsolenoidal functions of level-L are generated by connecting all the cells of level-L mesh in a tree. An example of the level-L nonsolenoidal functions is shown in Fig. 2 (a), in which the nonsolenoidal functions are depicted with bold black lines. The nonsolenoidal functions of level-l (l<L) are the union of the functions constructed on the trees in all the level-(l+1) cells. An example of the nonsolenoidal functions of level-l is shown in Fig. 2 (b).

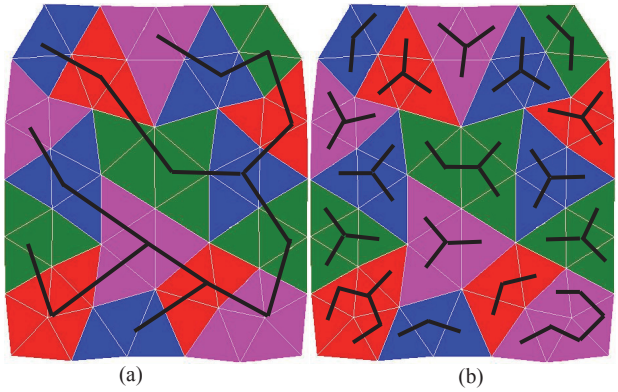

Fig. 2. Examples of the nonsolenoidal functions. (a) the level-L nonsolenoidal functions, (b) the level-l (l<L) nonsolenoidal functions.

III. REDUNDANT LOOP BASIS

Although the MR basis in [12, 15] is very effective for analysis of low-frequency problems, the "asymmetry" is still remained in the solenoidal part of the MR basis for closed surfaces. To maintain the "symmetry" of the solenoidal MR basis, all loop basis functions are proposed to be kept in the solenoidal MR basis, i.e. no solenoidal MR basis function associated to the interior vertex of closed surfaces need to be eliminated. As a result, the conditioning of the MoM matrix of the expanded MR basis can be improved. The redundant loop basis' property and its application to MR basis are investigated in this section.

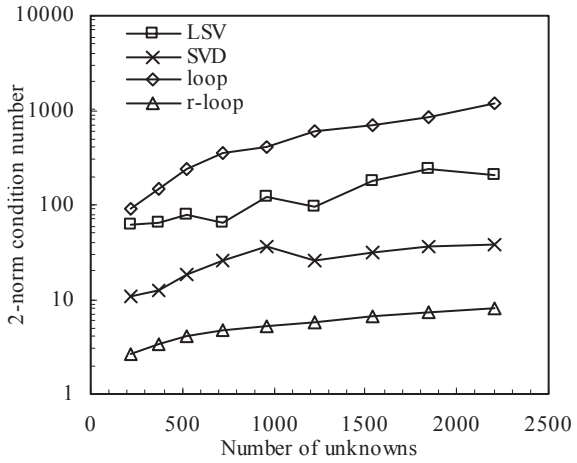

Fig. 3. The 2-norm condition number of MoM submatrices of a metallic sphere (radius = 1 m) discretized with different number of unknowns using different solenoidal bases at 1 MHz.

A. Property of redundant loop basis

Firstly, the 2-norm condition number of MoM solenoidal submatrix of different solenoidal bases with different discretization density is analyzed. As an example, the 2-norm condition number of MoM submatrices (after diagonal preconditioning) of a metallic sphere with a radius of 1 m discretized with the number of unknowns from about 200 to 2200 at the frequency of 1MHz is shown in Fig. 3. The LSV and SVD depicted in Fig. 3 represent the solenoidal bases generated from local SVD and SVD operations on charge matrices, respectively [14]. The 2-norm condition number of the redundant loop basis (denoted with r-loop in Fig. 3) is stated as the ratio of the largest singular value to the smallest nonzero singular value here. It can be found from Fig. 3 that the 2-norm condition number increases very fast as the number of unknowns increases for loop basis, while it performs more stable for the other solenoidal bases. The same phenomenon of the above solenoidal bases (except the redundant loop basis) is reported in [14], where the worse behavior of loop basis is explained. It is very interesting to be observed from Fig. 3 that the 2-norm condition number of the redundant loop basis is even smaller than that of SVD solenoidal basis. It is reasonable, since SVD solenoidal basis functions are not really orthogonal to each other although their divergences do.

To give a more direct illustration of the performance for the above solenoidal bases, Fig. 4 gives the eigenvalue distribution of MoM solenoidal submatrices (after diagonal preconditioning) in the case of the sphere discretized with 216 unknowns. It can be found from Fig. 4 (a) that the eigenvalues of SVD solenoidal basis are more closely clustered than that of LSV solenoidal basis, which indicates the MoM submatrix of SVD solenoidal basis has better conditioning than that of LSV solenoidal basis. By comparing Fig. 4 (a) and (b), it can be found that the eigenvalues of loop basis are more closely clustered than that of SVD solenoidal basis except there is an eigenvalue very close to zero. The eigenvalue of loop basis closest to zero is supposed to be the origin of the worse condition number for the matrix of loop basis compared with that of SVD solenoidal basis. Luckily, the redundant loop basis removes this eigenvalue to zero. As a result, the conditioning of the MoM solenoidal submatrix can be greatly improved. An explanation of the relation between the eigenvalue distribution of a matrix and the convergence of iterative solvers in solving the matrix can be found in [19].

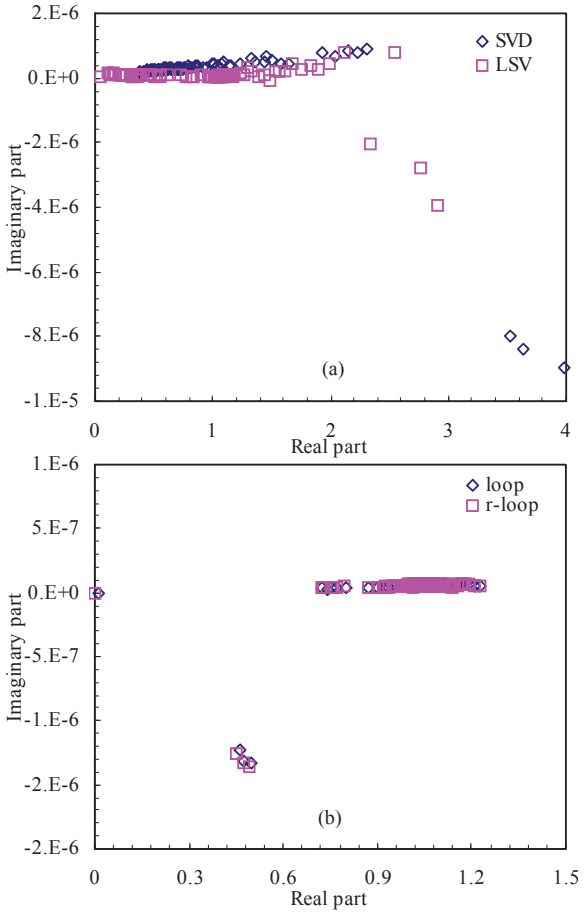

Fig. 4. The eigenvalue distribution of MoM solenoidal submatrices of the sphere discretized with 216 unknowns using different solenoidal bases at 1 MHz. (a) SVD and LSV solenoidal bases, (b) loop and redundant loop bases.

From the above discussion for the property of the redundant loop basis, it can be concluded that the redundant loop basis can remove the eigenvalue of its corresponding MoM submatrix closest to zero to zero and hence to form a well-conditioned MoM submatrix.

B. Application of redundant loop basis to MR basis

It has been discussed in Section II-B that the MR basis can take loop basis as its solenoidal part.

In order to improve the conditioning of the MoM matrix of the MR basis for closed structures, the redundant loop basis is proposed to be taken as the solenoidal part of the MR basis. To demonstrate the performance of the redundant loop basis in MR basis, it is compared with the MR bases which take the other solenoidal bases as their solenoidal part. Also, the application of the redundant loop basis in the MR basis is compared with its application in loop-tree basis.

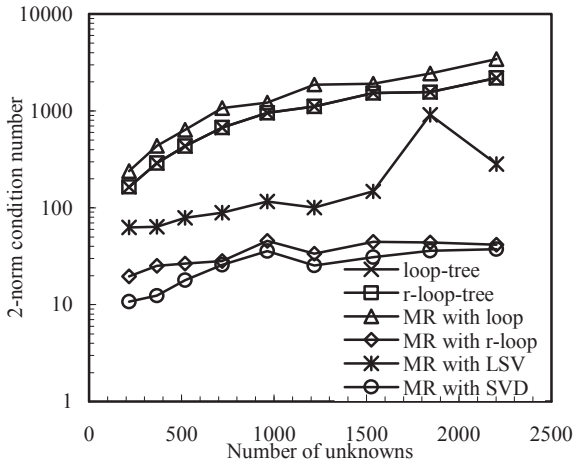

Fig. 5. The 2-norm condition number of MoM matrices of the sphere discretized with a different number of unknowns using different bases at 1 MHz.

Firstly, the 2-norm condition number of the MoM matrices of MR bases with different solenoidal parts and the loop-tree bases with loop or redundant loop solenoidal part is analyzed. The 2-norm condition number of the MoM matrices of these bases in the example of the sphere described above is depicted in Fig. 5. It can be observed from Fig. 5 that the 2-norm condition number of the MR basis with redundant loop solenoidal part is much lower than that of the MR basis with loop solenoidal part, while the 2-norm condition number of the loop-tree basis with loop solenoidal part (denoted with loop-tree in Fig. 5) is almost equal to that of the loop-tree basis with redundant loop solenoidal part (denoted with r-loop-tree in Fig. 5). It can also be observed from Fig. 5 that the 2-norm condition number of the MR basis with LSV solenoidal part is lower than the loop-tree basis and the MR basis with SVD solenoidal part is lower than the MR basis with LSV solenoidal part. However, the SVD solenoidal basis is generated by the SVD operations on the large charge matrix formed from all unknowns, which is prohibitive for a large number of unknowns due to the huge computational cost.

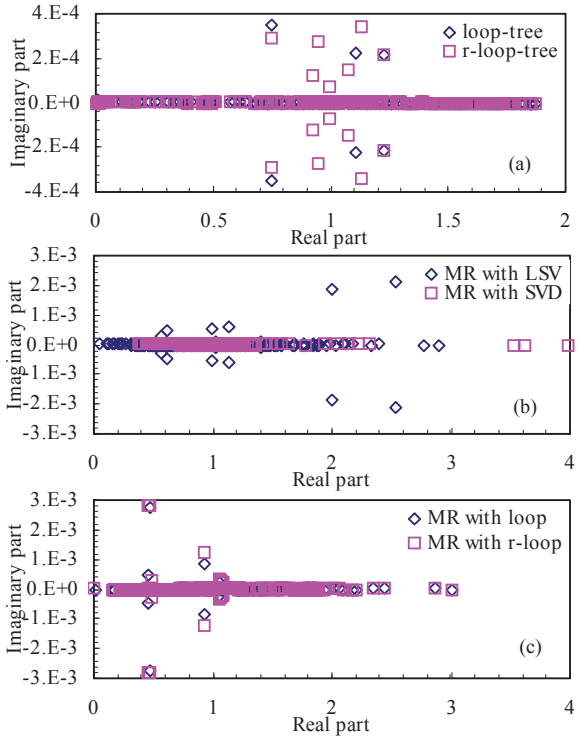

Fig. 6. The eigenvalue distribution of MoM matrices of the sphere discretized with 216 unknowns using different bases at 1 MHz. (a) Loop-tree bases with loop or redundant loop solenoidal part, (b) MR bases with LSV or SVD solenoidal part, (c) MR bases with loop or redundant loop solenoidal part.

Since the convergence behavior of iterative solvers in solving a MoM matrix is mainly determined by the eigenvalue distribution of the MoM matrix, the eigenvalue distribution of MoM matrices of the above bases are investigated. An example of the eigenvalue distribution of MoM matrices (after diagonal preconditioning) of the sphere discretized with 216 unknowns using different bases at the frequency of 1 MHz is shown in Fig. 6. It can be observed from Fig. 6 (a) (see also Fig. 9 (a) for a block) that there are a lot of eigenvalues of the loop-tree bases close to zero, which explains why it has trivial effect on the conditioning of the corresponding MoM matrix by

taking the redundant loop basis as the solenoidal part of the loop-tree basis. By comparing Fig. 6 (a) with Fig. 6 (b) and (c), it can be found that the number of eigenvalues of the loop-tree bases nearby zero is much larger than that of the MR bases, which explains why the conditioning of the MoM matrices of the loop-tree bases is worse than that of MR bases. It can be observed from Fig. 6 (b) that the eigenvalues of the MR basis with SVD solenoidal part is more closely clustered than that of the MR basis with LSV solenoidal part, which explains why the MoM matrix of the MR basis with SVD solenoidal part has a well condition number. It can be observed from Fig. 6 (c) (see also Fig. 9 (b) for a block) that the eigenvalues of the MR bases with loop or redundant loop solenoidal part are well distributed except there is a eigenvalue of the MR basis with loop solenoidal part very close to zero. Also, the smallest eigenvalue whose absolute value is about 1.3×10^{-2} is removed to zero by taking the redundant loop basis as the solenoidal part of the MR basis. Namely, the smallest eigenvalue is replaced by the previous second smallest eigenvalue whose value is about 0.15 by keeping the redundant loop basis in MR basis. As a result, the ratio of the absolute values of the largest eigenvalue to the smallest non-zero eigenvalue is improved which explains why the redundant loop basis can improve the conditioning of the MoM matrix of the MR basis effectively.

From the discussion given above, it can be concluded that the application of redundant loop basis in MR basis can improve conditioning of the MoM matrix of MR basis effectively, while it has trivial effect on the conditioning of the MoM matrix of loop-tree basis.

C. Solvability of expanded MR basis with iterative solvers

A similar phenomenon has been reported in [18], where a redundant volume loop basis is used to speed up the convergence of solutions in solving the volume integral equation and a proof is given to validate that the MoM matrix of the redundant volume loop basis can still be solved with an iterative solver without losing accuracy. The proof of the solvability of the MoM matrix of the expanded MR basis, which taking the redundant loop basis as its solenoidal part, can also be proved similarly. Alternatively, it can be proved easily by using a theorem in [19].

The expanded MR basis functions can be represented by the RWG basis functions via a basis-changing matrix $[T]$

$$\left[\vec{f}_{MR}\right]=[T]^{T}\left[\vec{R}^{0}\right], \tag{4}$$

where the number of RWG basis functions and MR basis functions is N and N+1 respectively, and the matrix $[T]$ is a row full-rank matrix. Then the corresponding MoM matrix equation can be written as

$$[Z_{MR}]\cdot[I_{MR}]=[b_{MR}], \tag{5}$$

where $[b_{MR}]=[T]^{T}\cdot[b]$, $[I]=[T]\cdot[I_{MR}]$, and $[Z_{MR}]=[T]^{T}\cdot[Z]\cdot[T]$ in which $[Z]$ is a full rank matrix formed from the RWG basis. It can be concluded that $[b_{MR}]$ belongs to the range space of $[Z_{MR}]$, since the rank of matrix $[Z_{MR}]$ and $[Z]$ is equal and $[T]$ is a row full-rank matrix. It has been pointed out in [19] that a square linear system $Ax = b$ has a Krylov solution if and only if b belongs to the range space of A. Therefore, the MoM matrix of the expanded MR basis can still be solved by Krylov iterative solvers. The bistatic RCS of a sphere (radius = 1 m) discretized with 3009 unknowns at 1 MHz is taken as an example and shown in Fig. 7. It can be found from Fig. 7 that a good agreement is obtained between the exact Mie series and the expanded MR basis.

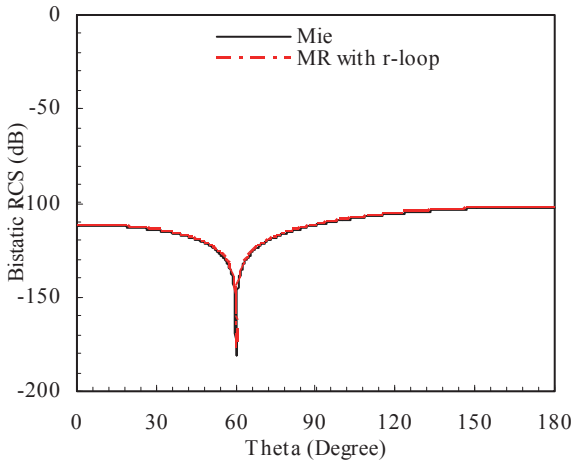

Fig. 7. Bistatic RCS of a sphere (radius = 1 m) discretized with 3009 unknowns at 1 MHz with the exact Mie series and the expanded MR basis with redundant loop solenoidal part.

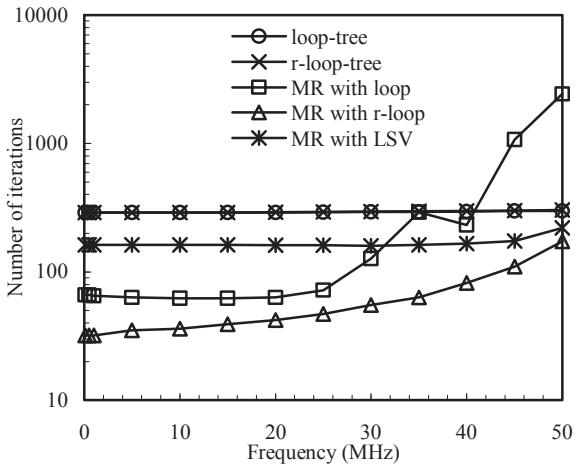

Fig. 8. The convergence behavior of GMRES(30) as a function of frequency for a block using the loop-tree bases and MR bases.

IV. NUMERICAL RESULTS

To validate the performance of the redundant loop basis applied in the MR basis, two examples will be analyzed in this section. The restarted GMRES(30) algorithm was chosen as the iterative solver. The examples were simulated in double precision with a relative residual of 10^{-5}. All the results with different bases were obtained after applying a diagonal preconditioning to the MoM matrix.

The first example is a metallic block (1m×1m×1m) with 1998 unknowns. The convergence behavior of GMRES(30) for the block using the loop-tree and MR bases over a frequency range of 0.1-50 MHz is shown in Fig. 8. It can be found from Fig. 8 that the redundant loop basis can further improve the performance of the MR basis while it has trivial effect on the loop-tree basis. Also, the LSV solenoidal basis performs more stable than the loop basis for the MR basis. However, the LSV solenoidal basis doesn't perform as well as the redundant loop basis as shown in Fig. 8. The eigenvalue distribution of MoM matrices of the block using the above bases at 20 MHz is shown in Fig. 9. It can also be observed from Fig. 9 that the eigenvalue closest to zero is removed to zero by taking the redundant loop basis as the solenoidal part for both loop-tree basis and MR basis. However, there is only one eigenvalue very close to zero for MR basis which explains why the redundant loop basis can improve conditioning of the MoM matrix of the MR basis effectively.

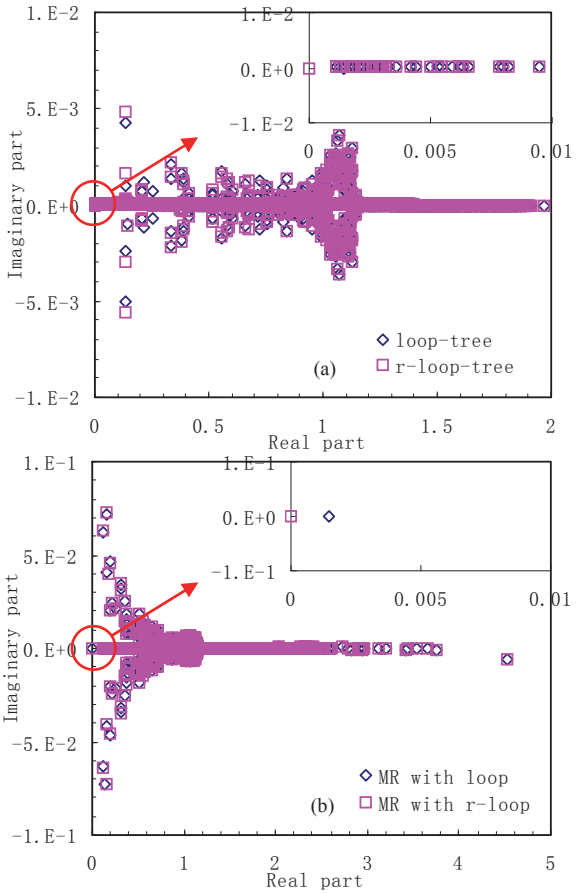

Fig. 9. The eigenvalue distribution of MoM matrices of a block using different bases at 20 MHz. (a) Loop-tree bases with loop or redundant loop solenoidal part, (b) MR bases with loop or redundant loop solenoidal part.

The second example is a more complex metallic plane model, whose length, width, and height is given by 9.3 m, 12.1 m, and 2.2 m, respectively. As shown in Fig. 10, the airplane model is nonuniformly discretized with 5034 unknowns. The number of iterations of the GMRES(30) using the above bases over a frequency range of 0.1-16 MHz is shown in Fig. 10. Obviously, the results of Fig. 10 also indicates that the redundant loop basis has significant advantage over the loop basis for MR basis. Also, the LSV solenoidal basis performs much better than the loop basis for the MR basis.

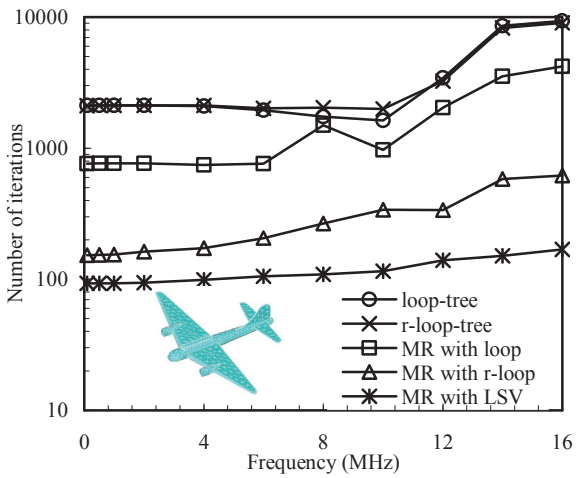

Fig. 10. The convergence behavior of GMRES(30) as a function of frequency for a metallic airplane model using the loop-tree bases and MR bases.

V. CONCLUSION

A redundant loop basis generated by simply keeping all loop functions is applied in MR basis to improve the convergence of MR basis for closed structures. The properties of the MoM matrices using the loop-tree and MR bases which take the loop or redundant loop basis as their solenoidal part are analyzed. It is found that the eigenvalue of the MoM matrix of the MR basis closest to zero is removed to zero by using the redundant loop basis, i.e. keeping the redundant loop basis moves the smallest eigenvalue to zero. As a consequence, the expanded MR basis taking the redundant loop basis as its solenoidal part has significant advantage than the MR basis with the loop basis in convergence for iterative solvers for closed surfaces at the low frequency range.

REFERENCES

[1] R. F. Harrington, *Field Computations by Moment Methods*, MacMillan, New York, 1968.

[2] S. Rao, D. Wilton, and A. Glisson, "Electromagnetic Scattering by Surfaces of Arbitrary Shape," *IEEE Trans. Antennas Propagat.*, vol. 30, pp. 409–418, May 1982.

[3] D. R. Wilton and A. W. Glisson, "On Improving the Electric Field Integral Equation at Low Frequencies," in *Proc. URSI Radio Science Meeting Dig.*, Los Angeles, CA, p. 24, June 1981.

[4] J. Mautz and R. F. Hanington, "An E-Field Solution for a Conducting Surface Small or Comparable to the Wavelength," *IEEE Trans. Antennas Propagat.*, vol. AP-32, no. 4, pp. 330-339, April 1984.

[5] M. Burton and S. Kashyap, "A Study of a Recent Moment-Method Algorithm that is Accurate to Very Low Frequencies," *Applied Computational Electromagnetic Society (ACES) Journal*, vol. 10, no. 3, pp. 58–68, Nov. 1995.

[6] W. L. Wu, A. Glisson, and D. Kajfez, "A Study of Two Numerical Solution Procedures for the Electric Field Integral Equation at Low Frequency," *Applied Computational Electromagnetic Society (ACES) Journal*, vol. 10, no. 3, pp. 69–80, Nov. 1995.

[7] G. Vecchi, "Loop-Star Decomposition of Basis Functions in the Discretization of the EFIE," *IEEE Trans. Antennas Propagat.*, vol. 47, no. 2, pp. 339–346, Feb. 1999.

[8] J. S. Zhao and W. C. Chew, "Integral Equation Solution of Maxwell's Equations from Zero Frequency to Microwave Frequency," *IEEE Trans. Antennas Propagat.*, vol. 48, pp. 1635–1645, Oct. 2000.

[9] J. F. Lee, R. Lee, and R. J. Burkholder, "Loop Star Basis Functions and a Robust Precodnitioner for EFIE Scattering Problems," *IEEE Trans. Antennas Propagat.*, vol. 51, pp. 1855–1863, Aug. 2003.

[10] T. F. Eibert, "Iterative-Solver Convergence for Loop-Star and Loop-Tree Decomposition in Method-of-Moments Solutions of the Electric-Field Integral Equation," *IEEE Antennas Propag. Mag.*, vol. 46, pp. 80–85, Jun. 2004.

[11] F. P. Andriulli, F. Vipiana, and G. Vecchi, "Enhanced Multiresolution Basis for the MoM Analysis of 3D Structures," in *Proc. IEEE Int. Symp. Antennas Propagat.*, pp. 5612–5615, Honolulu, HI, Jun. 2007.

[12] F. P. Andriulli, F. Vipiana, and G. Vecchi, "Hierarchical Bases for Non-Hierarchic 3-D Triangular Meshes," *IEEE Trans. Antennas Propagat.*, vol. 56, pp. 2288–2297, Aug. 2008.

[13] F. Vipiana, F. P. Andriulli, and G. Vecchi, "Two-Tier Non-Simplex Grid Hierarchic Basis for General 3D Meshes," *Waves in Random and Complex Media*, vol. 19, no. 1, pp. 126–146, Feb. 2009.

[14] F. Vipiana, and G. Vecchi, "A Novel, Symmetrical Solenoidal Basis for the MoM

Analysis of Closed Surfaces," *IEEE Trans. Antennas Propagat.*, vol. 57, no. 4, pp. 1294-1299, April 2009.

[15] J. J. Ding, R. S. Chen, J. Zhu, Z. H. Fan, and D. Z. Ding, "A Multiresolution Basis for Analysis of Scattering Problems," in *2010 International Conference on Microwave and Millimeter Wave Technology*, Chengdu, pp. 607-609, May 2010.

[16] J. J. Ding, J. Zhu, R. S. Chen, Z. H. Fan, and K. W. Leung, "An Alternative Multiresolution Basis in EFIE for Analysis of Low-Frequency Problems," *Applied Computational Electromagnetic Society (ACES) Journal*, vol. 26, no. 1, pp. 26-36, Jan. 2011.

[17] F. Vipiana, P. Pirinoli, and G. Vecchi, "Spectral Properties of the EFIE-MoM Matrix for Dense Meshes with Different Types of Bases," *IEEE Trans. Antennas Propagat.*, vol. 55, no. 11, pp. 3229–3238, Nov. 2007.

[18] M. K. Li and W. C. Chew, "Applying Divergence-Free Condition in Solving the Volume Integral Equation," *Progress In Electromagnetics Research*, PIER 57, pp. 311-333, 2006.

[19] I. C. F. Ipsen and C. D. Meyer, "The Idea Behind Krylov Methods," *Amer. Math. Monthly*, vol. 105, no. 10, pp. 889–899, Dec. 1998.

An Effective Technique for Enhancing Anti-Interference Performance of Adaptive Virtual Antenna Array

[1]Wenxing Li, [1]Yipeng Li, [1]Lili Guo, and [2]Wenhua Yu

[1]College of Information and Communication Engineering
Harbin Engineering University, Harbin 150001, China

[2]Electromagnetic Communication Lab
The Pennsylvania State University, University Park, PA 16802

Abstract - In this paper**,** we proposed an effective technique to enhance the anti-interference performance of the adaptive antenna arrays. The null depth in the direction of interferers determines the anti-interference performance of an adaptive antenna array. However, the null depth generated by the conventional **v**irtual **a**rray **t**ransformation (VAT) algorithm is usually not sufficient. By introducing the interference direction information into the transformation matrix, we can effectively improve the level of null depth; in turn, the **an**ti-interference performance of the adaptive antenna arrays is significantly enhanced. The numerical experiments are employed to validate the proposed approach.

Index Terms - Beam forming**,** null depth**,** SINR transformation matrix**, *v***irtual array**.**

I. INTRODUCTION

Generally speaking, the number of interference signals processed by an antenna array should be less than the degrees of system freedom [1, 2]. In the practical applications, the size and number of array elements are finite; however, frequently the number of interferers is much larger than the number of array elements. Obviously, some of the interferers will not be effectively inhibited when the number of interferers exceeds the degrees of system freedom. Friedlander [3] has proposed a virtual array transformation (VAT) method that the number of virtual array elements can be increased to be more than the degrees of system freedom so that all the interferers can be processed.

When Friedlander's method is used in the beam forming of an adaptive antenna array, the null depth is relatively shallow compared to the real antenna array. Consequently, the output signal to interference and noise ratio (SINR) will be decreased; in turn, it is not suitable for the applications that require the higher communication quality. The existing improvement techniques with regarding to the VAT performance [4-6] are concentrated on the applications in the estimation of interference arriving direction. Shubair *et al*. combined the least mean mixed norm (LMMN) algorithm and initialization using sample matrix inversion (SMI) to control the error norms and offer the extra degrees of freedom [7]. In order to achieve the better virtual array performance, the influence generated by the transformation area selection on the beam forming is analyzed in the literature [8]. The literature [9] proposed a method to transform an arbitrary shaped array into a virtual uniform linear array (ULA) and then suppress multiple coherent interferences through the spatial smoothing technique.

Based on the conventional VAT beam forming algorithm, an improved VAT method is presented in this paper, which can be effectively applied to raise the inhibition gain by improving the null depth. By projecting the transformation matrix on the interference space that enhances the interference components in the virtual covariance matrix, a higher interference inhibition gain can be achieved.

II. VIRTUAL ARRAY TRANSFORMATION THEORY

Considering an array with N elements [10], when M far field narrow band signals are incident on an antenna array, the received data $\mathbf{X}$ can be expressed as follows:

$$\mathbf{X} = \mathbf{A}\mathbf{S}(t) + \mathbf{N}(t), \tag{1}$$

where $\mathbf{S}(t)=[s_1(t),s_2(t),\cdots,s_M(t)]^T$ is a vector containing the complex signal envelops of M narrow-band signal sources. $(\bullet)^T$ denotes the matrix transposition. $\mathbf{N}(t)=[n_1(t),n_2(t),\cdots,n_N(t)]^T$ is a vector of zero-mean spatially white sensor noise of variance σ_n^2. $\mathbf{A}=[\mathbf{a}(\theta_1),\mathbf{a}(\theta_2),\cdots\mathbf{a}(\theta_M)]$ is an array manifold vector, where $\mathbf{a}(\theta_k),(k=1,2\cdots,M)$ represents a steering vector in the θ_k direction.

If an antenna array with N elements is uniform and linear, we have:

$$\mathbf{a}(\theta_k)=[1,e^{-j\frac{2\pi d}{\lambda}\sin\theta_k},\cdots,e^{-j(N-1)\frac{2\pi d}{\lambda}\sin\theta_k}]^T, \quad (2)$$

where d is the space between two adjacent elements. If both the signal and noise are linearly independent, the data covariance can be represented as:

$$\mathbf{R}=E\left\{\mathbf{X}(t)\mathbf{X}^H(t)\right\}=\mathbf{A}\mathbf{R}_s\mathbf{A}^H+\sigma_n^2\mathbf{I}, \quad (3)$$

where $E(\bullet)$ denotes the mathematical expectation. $\mathbf{R}_s=E\left\{\mathrm{S}(t)\mathrm{S}^H(t)\right\}$ represents the autocorrelation matrix of signal complex envelops. σ_n^2 is the noise power. $\mathbf{I}$ is the unit matrix, and $(\bullet)^H$ denotes the matrix conjugate transposition. The array covariance matrix is estimated using the finite snap data $\mathbf{X}(i)$:

$$\hat{\mathbf{R}}=\frac{1}{K}\sum_{i=1}^{K}\mathbf{X}(i)\mathbf{X}^H(i),$$

where K is the snap number. In the array interpolation operation, the real array manifold is transformed on a preliminary specified virtual array manifold over a given angular sector Θ, namely, an interpolation matrix $\mathbf{B}$ is designed to satisfy:

$$\mathbf{B}\mathbf{a}(\theta)\approx\bar{\mathbf{a}}(\theta),\forall\theta\in\Theta, \quad (4)$$

where $\mathbf{a}(\theta)$ and $\bar{\mathbf{a}}(\theta)$ are $N\times1$ and $\bar{N}\times1$ steering vectors of the real and virtual arrays, respectively; $\bar{N}$ is the number of virtual elements; virtual array manifold $\bar{\mathbf{a}}(\theta)$ corresponds to a uniform linear array (ULA).

The computation of interpolation matrix $\mathbf{B}$ is carried out by choosing k representative directions $\theta_1,\theta_2,\cdots,\theta_k$ from the interpolation sector Θ, and minimizing the sum of quadratic interpolation errors in these directions:

$$F(\mathbf{B})=\sum_{i=1}^{k}\left\|\mathbf{B}\mathbf{a}(\theta_i)-\bar{\mathbf{a}}(\theta_i)\right\|^2=\left\|\mathbf{B}\mathbf{A}-\bar{\mathbf{A}}\right\|_F, \quad (5)$$

where $\mathbf{A}$ and $\bar{\mathbf{A}}$ are the real and virtual array manifold vector matrixes, respectively; and $\|\ \|_F$ denotes the *Frobenius* mold. The optimal minimum variance obtained from (5) is:

$$\mathbf{B}=\bar{\mathbf{A}}\mathbf{A}^H(\mathbf{A}\mathbf{A}^H)^{-1}. \quad (6)$$

After transformation, the covariance of virtual array becomes:

$$\bar{\mathbf{R}}=\mathbf{B}\mathbf{R}\mathbf{B}^H. \quad (7)$$

Through the noise-prewhitening process [3], the optimal weight can be obtained by using the minimum variance distortionless response method:

$$\mathbf{W}_{opt}=\alpha\bar{\mathbf{R}}^{-1}\bar{\mathbf{a}}(\theta_0), \quad (8)$$

where $\bar{\mathbf{a}}(\theta_0)$ represents a virtual array steering vector in the desired signal direction; and the coefficient $\alpha=\left[\bar{\mathbf{a}}^H(\theta_0)\bar{\mathbf{R}}^{-1}\bar{\mathbf{a}}(\theta_0)\right]^{-1}$.

III. NULL DEEPENING TECHNIQUE

Compared to the real array with the same parameters, the null depth formed by a virtual array in the Friedlander's VAT method is relatively shallow. To improve the null depth, we project the transformation matrix $\mathbf{B}$ on the interference space, and thus, the constraint information of the interference direction can be imported into the transformation matrix to enhance the interference components in the sampling covariance matrix. The detailed procedure is described as follows:

If the interference directions are $\theta_1,\theta_2,\cdots,\theta_{M'}$ and the number of interferers is M', the virtual array steering vector in the interferer directions $\bar{\mathbf{a}}(\theta_1),\bar{\mathbf{a}}(\theta_2),\cdots,\bar{\mathbf{a}}(\theta_{M'})$ can be calculated. Define a projection matrix $\mathbf{C}$ as:

$$\mathbf{C}=\left(\sum_{i=1}^{M'}\bar{\mathbf{a}}(\theta_i)\bar{\mathbf{a}}^H(\theta_i)\right)^H. \quad (9)$$

Projecting the transformation matrix on the interference space, we have:

$$\bar{\mathbf{B}}=\mathbf{C}\mathbf{B}. \quad (10)$$

Now the covariance matrix of virtual array becomes:

$$\tilde{\bar{\mathbf{R}}}=\bar{\mathbf{B}}\mathbf{R}\bar{\mathbf{B}}^H=\mathbf{C}\mathbf{B}\mathbf{R}\mathbf{B}^H\mathbf{C}^H=\mathbf{C}\bar{\mathbf{R}}\mathbf{C}^H. \quad (11)$$

After the mathematical operations, the information of the interference direction has already been involved in the transformed virtual covariance matrix $\tilde{\bar{\mathbf{R}}}$, and the interference components is strengthened.

IV. THEORETICAL ANALYSIS

According to Schmidt's orthogonal subspace resolution theory, using the eigenvalue decomposition from (7) $\bar{\mathbf{R}}$ can be expressed as [11]:

$$\bar{\mathbf{R}} = \bar{\mathbf{U}}\bar{\mathbf{\Sigma}}\bar{\mathbf{U}}^H, \tag{12}$$

where $\bar{\mathbf{U}}$ is an eigenvector vector of covariance matrix $\bar{\mathbf{R}}$, the diagonal matrix $\bar{\mathbf{\Sigma}}$ constituted by the corresponding eigenvalues is:

$$\bar{\mathbf{\Sigma}} = \begin{bmatrix} \bar{\lambda}_1 & & & \\ & \bar{\lambda}_2 & & \\ & & \ddots & \\ & & & \bar{\lambda}_{\bar{N}} \end{bmatrix}. \tag{13}$$

If a virtual array with $\bar{N}$ elements is ULA, the steering directions can be written as:

$$\bar{\mathbf{a}}(\theta_i) = [1, e^{-j\frac{2\pi\bar{d}}{\lambda}\sin\theta_i}, \cdots, e^{-j(\bar{N}-1)\frac{2\pi\bar{d}}{\lambda}\sin\theta_i}]^T, \tag{14}$$

where $\bar{d}$ is the space between two adjacent elements. We have:

$$\bar{\mathbf{a}}(\theta_i)\bar{\mathbf{a}}^H(\theta_i) = \begin{bmatrix} 1 \\ e^{-j\frac{2\pi\bar{d}}{\lambda}\sin\theta_i} \\ \vdots \\ e^{-j(\bar{N}-1)\frac{2\pi\bar{d}}{\lambda}\sin\theta_i} \end{bmatrix} \cdot [1, e^{-j\frac{2\pi\bar{d}}{\lambda}\sin\theta_i}, \cdots, e^{-j(\bar{N}-1)\frac{2\pi\bar{d}}{\lambda}\sin\theta_i}].$$

$$= \begin{bmatrix} 1 & e^{-j\frac{2\pi\bar{d}}{\lambda}\sin\theta_i} & \cdots & e^{-j(\bar{N}-1)\frac{2\pi\bar{d}}{\lambda}\sin\theta_i} \\ e^{-j\frac{2\pi\bar{d}}{\lambda}\sin\theta_i} & e^{-j\cdot 2\cdot\frac{2\pi\bar{d}}{\lambda}\sin\theta_i} & \cdots & e^{-j(\bar{N}-1+1)\frac{2\pi\bar{d}}{\lambda}\sin\theta_i} \\ \vdots & \vdots & \cdots & \vdots \\ e^{-j(\bar{N}-1)\frac{2\pi\bar{d}}{\lambda}\sin\theta_i} & e^{-j(\bar{N}-1+1)\frac{2\pi\bar{d}}{\lambda}\sin\theta_i} & \cdots & e^{-j\cdot 2\cdot(\bar{N}-1)\frac{2\pi\bar{d}}{\lambda}\sin\theta_i} \end{bmatrix}. \tag{15}$$

Substitute (15) into (9), we can obtain the expression of projection matrix $\mathbf{C}$:

$$\mathbf{C} = \left(\sum_{i=1}^{M'} \bar{\mathbf{a}}(\theta_i)\bar{\mathbf{a}}^H(\theta_i)\right)^H = \left(\sum_{i=1}^{M'} \begin{bmatrix} 1 & e^{-j\frac{2\pi\bar{d}}{\lambda}\sin\theta_i} & \cdots & e^{-j(\bar{N}-1)\frac{2\pi\bar{d}}{\lambda}\sin\theta_i} \\ e^{-j\frac{2\pi\bar{d}}{\lambda}\sin\theta_i} & e^{-j\cdot 2\cdot\frac{2\pi\bar{d}}{\lambda}\sin\theta_i} & \cdots & e^{-j(\bar{N}-1+1)\frac{2\pi\bar{d}}{\lambda}\sin\theta_i} \\ \vdots & \vdots & \cdots & \vdots \\ e^{-j(\bar{N}-1)\frac{2\pi\bar{d}}{\lambda}\sin\theta_i} & e^{-j(\bar{N}-1+1)\frac{2\pi\bar{d}}{\lambda}\sin\theta_i} & \cdots & e^{-j\cdot 2\cdot(\bar{N}-1)\frac{2\pi\bar{d}}{\lambda}\sin\theta_i} \end{bmatrix}\right)^H. \tag{16}$$

Substitute (12) and (13) into (11), then we have:

$$\tilde{\bar{\mathbf{R}}} = \mathbf{C}\bar{\mathbf{R}}\mathbf{C}^H = \mathbf{C}\bullet\left(\bar{\mathbf{U}}\bar{\mathbf{\Sigma}}\bar{\mathbf{U}}^H\right)\bullet\mathbf{C}^H = \mathbf{C}\bullet\left(\bar{\mathbf{U}}\bullet\begin{bmatrix} \bar{\lambda}_1 & & & \\ & \bar{\lambda}_2 & & \\ & & \ddots & \\ & & & \bar{\lambda}_{\bar{N}} \end{bmatrix}\bullet\bar{\mathbf{U}}^H\right)\bullet\mathbf{C}^H. \tag{17}$$

Substitute $\mathbf{C}$ into (17), $\tilde{\bar{\mathbf{R}}}$ can be expressed as:

$$\tilde{\mathbf{R}}=\left(\sum_{i=1}^{M'}\begin{bmatrix} 1 & e^{-j\frac{2\pi\bar{d}}{\lambda}\sin\theta_i} & \cdots & e^{-j(\bar{N}-1)\frac{2\pi\bar{d}}{\lambda}\sin\theta_i} \\ e^{-j\frac{2\pi\bar{d}}{\lambda}\sin\theta_i} & e^{-j\cdot2\cdot\frac{2\pi\bar{d}}{\lambda}\sin\theta_i} & \cdots & e^{-j(\bar{N}-1+1)\frac{2\pi\bar{d}}{\lambda}\sin\theta_i} \\ \vdots & \vdots & \cdots & \vdots \\ e^{-j(\bar{N}-1)\frac{2\pi\bar{d}}{\lambda}\sin\theta_i} & e^{-j(\bar{N}-1+1)\frac{2\pi\bar{d}}{\lambda}\sin\theta_i} & \cdots & e^{-j\cdot2\cdot(\bar{N}-1)\frac{2\pi\bar{d}}{\lambda}\sin\theta_i} \end{bmatrix}\right)^H \bullet \left(\bar{\mathbf{U}}\bullet\begin{bmatrix}\bar{\lambda}_1 & & & \\ & \bar{\lambda}_2 & & \\ & & \ddots & \\ & & & \bar{\lambda}_{\bar{N}}\end{bmatrix}\bullet\bar{\mathbf{U}}^H\right)\bullet$$
$$\left(\sum_{i=1}^{M'}\begin{bmatrix} 1 & e^{-j\frac{2\pi\bar{d}}{\lambda}\sin\theta_i} & \cdots & e^{-j(\bar{N}-1)\frac{2\pi\bar{d}}{\lambda}\sin\theta_i} \\ e^{-j\frac{2\pi\bar{d}}{\lambda}\sin\theta_i} & e^{-j\cdot2\cdot\frac{2\pi\bar{d}}{\lambda}\sin\theta_i} & \cdots & e^{-j(\bar{N}-1+1)\frac{2\pi\bar{d}}{\lambda}\sin\theta_i} \\ \vdots & \vdots & \cdots & \vdots \\ e^{-j(\bar{N}-1)\frac{2\pi\bar{d}}{\lambda}\sin\theta_i} & e^{-j(\bar{N}-1+1)\frac{2\pi\bar{d}}{\lambda}\sin\theta_i} & \cdots & e^{-j\cdot2\cdot(\bar{N}-1)\frac{2\pi\bar{d}}{\lambda}\sin\theta_i} \end{bmatrix}\right), \tag{18}$$

(18) can be further simplified as:

$$\tilde{\mathbf{R}}=\tilde{\mathbf{U}}\bullet\begin{bmatrix} M'^2\cdot\bar{\lambda}_1 & & & \\ & \left(1+e^{-j\cdot2\cdot\frac{2\pi\bar{d}}{\lambda}\sin\theta_1}+\cdots+e^{-j\cdot2\cdot\frac{2\pi\bar{d}}{\lambda}\sin\theta_{M'}}\right)^2\cdot\bar{\lambda}_2 & & \\ & & \ddots & \\ & & & \left(1+e^{-j\cdot2\cdot(\bar{N}-1)\cdot\frac{2\pi\bar{d}}{\lambda}\sin\theta_1}+\cdots+e^{-j\cdot2\cdot(\bar{N}-1)\cdot\frac{2\pi\bar{d}}{\lambda}\sin\theta_{M'}}\right)^2\cdot\bar{\lambda}_{\bar{N}}\end{bmatrix}\bullet\tilde{\mathbf{U}}^H,$$
$$=\tilde{\mathbf{U}}\bullet\tilde{\boldsymbol{\Sigma}}\bullet\tilde{\mathbf{U}}^H$$
$$=\tilde{\mathbf{U}}\bullet\begin{bmatrix}\tilde{\bar{\lambda}}_1 & & & \\ & \tilde{\bar{\lambda}}_2 & & \\ & & \ddots & \\ & & & \tilde{\bar{\lambda}}_{\bar{N}}\end{bmatrix}\bullet\tilde{\mathbf{U}}^H, \tag{19}$$

where $\tilde{\bar{\mathbf{U}}}$ is the eigenvector matrix corresponding to $\tilde{\bar{\mathbf{R}}}$, $\tilde{\bar{\boldsymbol{\Sigma}}}=\begin{bmatrix}\tilde{\bar{\lambda}}_1 & & & \\ & \tilde{\bar{\lambda}}_2 & & \\ & & \ddots & \\ & & & \tilde{\bar{\lambda}}_{\bar{N}}\end{bmatrix}$ is the diagonal matrix constituted by the eigenvalues of $\tilde{\bar{\mathbf{R}}}$. From (19) it is obviously observed:

$$\tilde{\bar{\lambda}}_i>\bar{\lambda}_i, i=1,2,\cdots,\bar{N}. \tag{20}$$

The eigenvalues of the covariance matrix obtained by using the improved VAT algorithm are bigger than those obtained from the conventional VAT algorithm.

Next, we briefly introduce the minimum variance distortionless response (MVDR) beam forming method [12]. In the direction of the desired signal, the gain is constrained to be 1, and the array output power is ensured to be minimum, namely, the interference and noise will generate the minimum output power. Applied to the virtual array, the weight vector of the MVDR beam forming is the solution to the following problem:

$$\mathbf{W}_{MVDR}=\arg\min_{\mathbf{W}^H\bar{\mathbf{a}}(\theta_0)=1}E\left[\left|\mathbf{W}^H\bar{\mathbf{X}}(k)\right|^2\right]$$
$$=\arg\min_{\mathbf{W}^H\bar{\mathbf{a}}(\theta_0)=1}\mathbf{W}^H\tilde{\bar{\mathbf{R}}}\mathbf{W}, \tag{21}$$

where the $\arg\min_{\mathbf{W}^H\bar{\mathbf{a}}(\theta_0)=1}[\ ]$ represents the optimal solution which can minimize the function value in $[\ ]$ and satisfy the equality $\mathbf{W}^H\bar{\mathbf{a}}(\theta_0)=1$. The *arg* represents an inverse function. It can be solved using Lagrangian multiplier method:

$$\mathbf{W}_{MVDR} = \frac{\tilde{\tilde{\mathbf{R}}}^{-1}\bar{\mathbf{a}}(\theta_0)}{\bar{\mathbf{a}}^H(\theta_0)\tilde{\tilde{\mathbf{R}}}^{-1}\bar{\mathbf{a}}(\theta_0)},$$

which is equivalent to (8). The characteristic of the MVDR method in the desired signal direction is that the gain is restrained to be 1 and the simultaneously array output power is ensured to be minimum. The higher the interference power in array is, the stronger it's inhibited in these directions. By introducing the constraint information of the interference direction into the transformation matrix **B** in the improved VAT algorithm, the new eigenvalues of the covariance matrix become bigger, and the signal components corresponding to them are strengthened. Therefore, in these directions the inhibition gains will increase by the the MVDR method, namely, the null depths will be deeper as showed in the beam pattern.

V. SIMULATION VERIFICATION

The original array with 5 elements is uniform and linear, and the element space is λ. The expected signal illumines from the 0° direction. The signal to noise ratio is *SNR*=0dB. Three independent interferers come from -60°, -40°, and 50° directions, respectively. The signal to interference ratio is $SIR = -40dB$. The virtual array with 8 elements is uniform and linear, and the element space is $\lambda/2$. The virtual transformation area is [-65°, 55°]. The step-size is 0.1°. The number of snapshots is 200. Figure 1 shows the gain comparison obtained by using the MVDR beam forming through the real array method, the conventional and improved VAT algorithms. Figure 2 shows the eigenvalue comparison of covariance matrix obtained using three methods. Figure 3 shows the comparison of output SINR obtained by three methods.

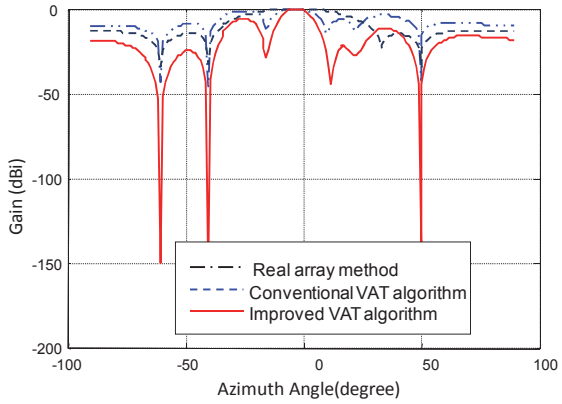

Fig. 1. Beam patterns using the different methods.

It is observed from Figures 1 to 3 that when the number of independent interferers is not larger than the number of the array elements, the nulls of the beam forming using the real array, conventional VAT, and the improved VAT algorithm are generated precisely in the interferer directions, and the main lobe is pointed to the desired signal direction. The inhibition gain using the real array and conventional VAT algorithms is about -35 dBi and -45 dBi, respectively. However, the inhibition gain using the proposed algorithm can reach up to -150 dBi. The eigenvalue of the covariance matrix has been significantly improved in the proposed method. Similarly, the output SINR has been significantly improved as well in the proposed method.

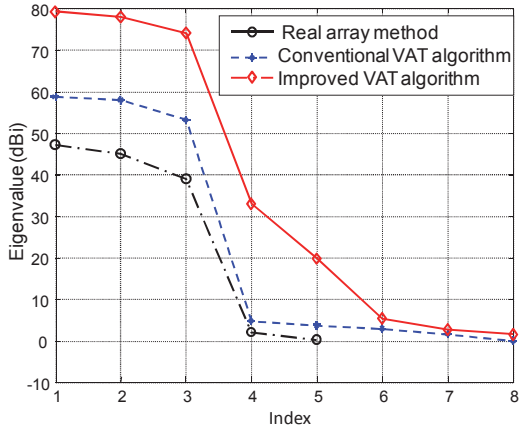

Fig. 2. Eigenvalues of the covariance matrix in the different methods.

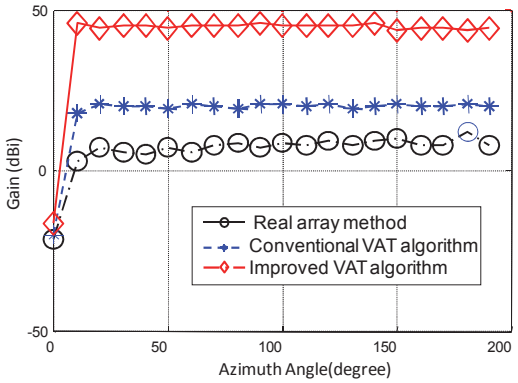

Fig. 3. Output SINR using the different methods.

Next, we use an example to validate the proposed method, in which the original array with 5 elements and space λ between the adjacent elements is uniform and linear. The desired signal incidence comes in the 0° direction. The signal to noise ratio is $SNR = 0dB$ and five independent interferers come in -60°, -40°, 20°, 50°, and 70° directions, respectively. The signal to interference ratio is $SIR = -40dB$. The virtual array with 8 elements and space $\lambda/2$ between the adjacent elements is uniform and linear. The virtual transformation area is [-65°, 75°] and the step size is 0.1°. The number of snapshots is 200. Figure 4 shows the comparison of the MVDR beam forming using the different methods. Figure 5 shows the eigenvalue comparison of the covariance matrix using the three methods. Figure 6 shows the comparison of output SINR using three methods.

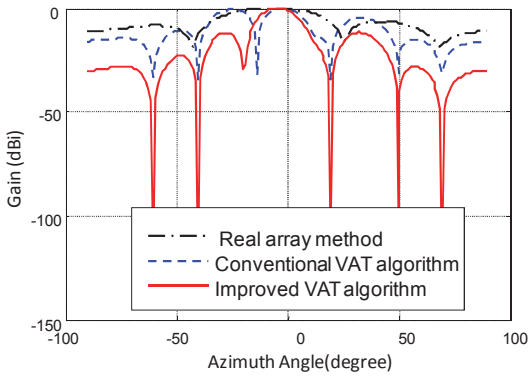

Fig. 4. Beam forming of five independent interferers using the different methods.

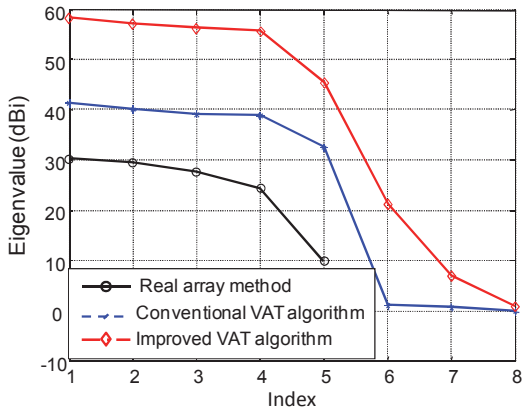

Fig. 5. Eigenvalues of five independent interferers using the different methods.

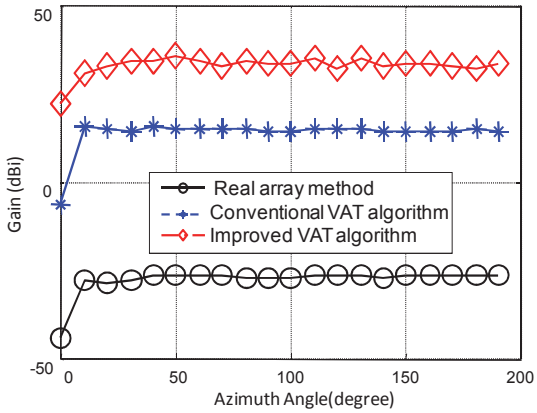

Fig. 6. Output SINR of five independent interferers using the different methods.

It is observed from Figs. 4 to 6 that when the number of interferers exceeds the freedom of original array, the nulls in the real array method cannot be generated in these interference directions. The virtual array with 8 elements cannot process all the interferers, but the nulls precisely point to these interferers. The inhibition gain using the conventional and proposed VAT algorithms is about -30 dB -120 dB, respectively. The eigenvalue of the improved algorithm has significantly improved, as well as the SINR.

VI. CONCLUSIONS

An improved VAT method has been presented in this paper, compared with the conventional approach; the null performance of beam forming is significantly improved. The nulls pointing to interference directions can be more steadily generated, and interference inhibition gains are much better and ensure a higher output SINR. Compared to

the conventional algorithm, the proposed method only needs one more matrix multiplication operation.

REFERENCES

[1] M. Zatman, "Degree of Freedom Architectures for Large Adaptive Arrays," *Conference Record of the Asilomar Conference on Signals, Systems and Computers*, vol. 1, pp. 109-112, 1999.

[2] R. Games and R. Williams, "Performance Analysis of a Concurrent Adaptive Least-Squares Sidelobe Cancellation System with Excess Degrees of Freedom," *IEEE APS Int Symp Dig*., vol. 1, pp. 86-89, 1991.

[3] B. Friedlander, "The Root-Music Algorithm for Direction Finding with Interpolated Arrays," *Signal Processing*, vol. 30, no. 1, pp. 15-29, 1993.

[4] P. Hyberg, M. Jansson, and B. Ottersten, "Array Interpolation and Bias Reduction," *Signal Processing*, vol. 52, no. 10, pp. 2711-2720, 2004.

[5] M. Gavish and A. Weiss, "Direction Finding Using Esprit with Interpolated Arrays," *IEEE transactions on Signal Processing*, vol. 39, no. 6, pp. 1473-1478, 1991.

[6] M. Pesavento, A. Gershman, and Z. Luo. "Robust Array Interpolation Using Second Order Cone Programming," *IEEE Signal Processing Lett*, vol. 9, no. 1, pp. 8-11, 2002.

[7] R. Shubair, S. Jimaa, and A. Omar, "Robust Adaptive Beamforming Using Least Mean Mixed Norm Algorithm," *Applied Computational Electromagnetic Society (ACES) Journal*, vol. 23, no. 3, pp. 262-269, 2008.

[8] S. Baowei, "Robust Adaptive Beam Forming Via Array Transformation," *IEEE AP-S International Symposium on Antennas and Propagation*, DC, USA, vol. 1B, pp. 331-334, 2005.

[9] T. Lee and T. Lin, "Adaptive Beam Forming with Interpolated Arrays for Multiple Coherent Interferers," *Signal Processing*, vol. 57, no. 2, pp. 177-194, 1997.

[10] K. Reddy and V. Reddy, "Analysis of Interpolated Arrays with Spatial Smoothing," *Signal Processing*, vol. 54, no. 3, pp. 261-272, 1996.

[11] R. Schmidt, "Multiple Emitter Location and Signal Parameter Estimation," *IEEE Trans on Antennas and propagation*, vol. 34, no. 3, pp. 276-280, 1986.

[12] M. Souden and J. Benesty, "A Study of the LCMV and MVDR Noise Reduction Filters," *IEEE Transactions on Signal Processing*, vol. 58, no. 3, pp. 4925-4935, 2010.

A High Performance Parallel FDTD Based on Winsock and Multi-Threading on a PC-Cluster

X. Duan [1], X. Chen [1], K. Huang [1], and H. Zhou [2]

[1] College of Electronics and Information Engineering
Sichuan University, Chengdu, 610064, P. R. China
shawnduan@gmail.com, xingcsc@yahoo.com.cn, kmhuang@scu.edu.cn

[2] Institute of Applied Physics and Computational Mathematics of Beijing
Beijing, 100094, P. R. China
zhou-haijing@vip.sina.com

Abstract - Parallel technology is a powerful tool to provide the necessary computing power and memory resources for the FDTD method to simulate electrically-large and complex structures. In this paper, a high performance parallel FDTD is developed for multi-core cluster systems. It employs Winsock to achieve efficient inter-process communication as well as multi-threading to make full use of the hardware resources of multi-core processors on a PC-cluster. Key steps for parallel FDTD such as synchronization, data exchange, load balancing, etc., are investigated. An experiment simulating the scattering of an incident electromagnetic wave form of a computer case is presented which shows that the proposed parallel FDTD achieved speedup of 25.1 and parallel efficiency of 83.7% when 10 processors with 30 cores are utilized, and outperforms traditional parallel FDTD based on MPI or MPI-OpenMP, which gained speedup of 22.9, 24.9 and parallel efficiency of 76.3%, 83.1% respectively under the same circumstances.

Index Terms ─ FDTD, multi-threading, parallel computation, PC cluster, Winsock.

I. INTRODUCTION

As one of the most popular numerical methods, finite-difference time-domain (FDTD) has been widely used to solve various electromagnetic problems [1, 2]. However, the implementation of FDTD for simulating electrically-large and complex structures requires intensive computation and large amounts of memory resources, which is not possessed by a single machine. A highly efficient solution is to implement the FDTD algorithm in a parallel computer system, such as a PC cluster [3, 4, 5].

The FDTD method is conducive to parallel computation due to its structured mesh, regular data structures, and localized calculation [3, 6]. A common method to parallelize the FDTD is to divide the computation domain into many sub-domains that are calculated in different nodes of a cluster, and because the workload of each sub-domain is far less than that of the whole computation space, the memory, and time consumption is greatly reduced [4, 5, 7, 8]. Up till now, message passing interface (MPI), a library specification for message-passing [9, 10], is by far the most popular parallel programming environment for the FDTD to realize operations such as data exchange, synchronization, and etc. [3, 4, 6, 7, 8].

Today's PC clusters have employed multi-core processors, which integrate multiple execution cores on the same chip and thereby introduce a new level of parallelization. Many of the previous researches [3, 4, 5, 6, 7, 8] on the parallel FDTD have not taken multi-core processors into consideration. To take advantage of the computing capability of multi-core processors, it is necessary

for a parallel computation to carefully take both the intranode communication and the internode communication into account. Some implementations of MPI have made efforts to it. For instance, MPICH2-1.3.1 offers multi-core support by integrating a low-level communication subsystem called Nemesis to minimize the overhead for intranode communication by using lock-free queues in the processes and other optimizations such as a fastbox mechanism to bypass the queues [11,12]. However, in comparison with MPI that uses messages to perform intranode communication, creating threads to make data accessible through shared memory is a more natural method and supports greater bandwidth [13, 14].

A few studies [15,16] utilize open multi-processing (OpenMP), a shared memory parallel programming interface [17, 18], together with MPI to enhance shared-memory performance. However, a straight-forward integration of OpenMP constructs into the MPI program often does not give good speedup results [19]. Optimization techniques like minimizing OpenMP parallel overhead, aggregating messages, CPU affinity and cache-line alignment are usually necessary for a better performance. Thus, it requires programmers to have relatively substantial experience in tuning an OpenMP code.

In this work, a novel parallel FDTD algorithm based on Winsock and multi-threading is proposed. To fully exploit the computation capacity of a PC cluster with both multi-processor and multi-core features, it utilizes the efficient, low-level Winsock programming rather than MPI to realize the message passing between processors, creates threads, and maps them to cores by using Win32 thread application program interface (API), so the sub-domain computation is carried out in each core. Data exchange between threads is performed by shared variables being directly written by one thread and read by another. Meanwhile in this parallel FDTD, only magnetic field values on the sub-domains' interfaces need to be transmitted by using an overlapping scheme, an efficient synchronization mechanism is used to impose constraints on the execution order of threads, and the different workload of various cells (such as ordinary and perfectly matched layer (PML) [20]) are taken into consideration in the domain decomposition phase to achieve better load balancing.

A numerical experiment has been conducted to estimate the efficiency of the proposed FDTD parallelization strategy. In the experiment, three parallel FDTD codes based on the proposed method, MPI, and MPI-OpenMP, respectively, are developed to simulate the same electromagnetic model in parallel on a PC cluster, and their run time, speedup, and parallel efficiency are compared and analyzed.

The remainder of this paper is organized as follows: Section II briefly introduces the FDTD method, while Section III describes the essential elements of the parallel FDTD based on Winsock and multi-threading. The experimental results are presented in Section IV and finally conclusions in Section V.

II. A BRIEF INTRODUCTION TO THE FDTD METHOD

Since Kane S. Yee's paper in 1966 [1], the FDTD has developed into a widely-used numerical simulation method. In Yee's difference scheme, the computation domain is discretized to space grids in Cartesian Coordinates. The FDTD update equations are then obtained by discretizing Maxwell's two curl equations using central-difference approximations to the space and time partial derivatives. The updated equations for Ex and Hx [6] are as follows:

$$E_x^{n+1}(i+\frac{1}{2},j,k)=\frac{\varepsilon_x-0.5\Delta t\sigma_x}{\varepsilon_x+0.5\Delta t\sigma_x}E_x^{n}(i+\frac{1}{2},j,k)+\frac{\Delta t}{\varepsilon_x+0.5\Delta t\sigma_x}\left[\begin{array}{l}\dfrac{H_z^{n+\frac{1}{2}}(i+\frac{1}{2},j+\frac{1}{2},k)-H_z^{n+\frac{1}{2}}(i+\frac{1}{2},j-\frac{1}{2},k)}{\Delta y}\\ -\dfrac{H_y^{n+\frac{1}{2}}(i+\frac{1}{2},j,k+\frac{1}{2})-H_y^{n+\frac{1}{2}}(i+\frac{1}{2},j,k-\frac{1}{2})}{\Delta z}\end{array}\right], \quad (1)$$

$$H_x^{n+\frac{1}{2}}(i,j+\frac{1}{2},k+\frac{1}{2})=\frac{\mu_x-0.5\Delta t\sigma_{Mx}}{\mu_x+0.5\Delta t\sigma_{Mx}}H_x^{n-\frac{1}{2}}(i,j+\frac{1}{2},k+\frac{1}{2})+\frac{\Delta t}{\mu_x+0.5\Delta t\sigma_{Mx}}\left[\begin{array}{l}\dfrac{E_y^{n}(i,j+\frac{1}{2},k+1)-E_y^{n}(i,j+\frac{1}{2},k)}{\Delta z}\\ -\dfrac{E_z^{n}(i,j+1,k+\frac{1}{2})-E_z^{n}(i,j,k+\frac{1}{2})}{\Delta y}\end{array}\right], \quad (2)$$

thus only adjacent cells are needed for the computation. Similar equations can be written for the other electric and magnetic field components.

III. A PARALLEL FDTD BASED ON WINSOCK AND MULTI-THREADING

A. Parallel programming model

In a PC cluster, processors are in a distributed address space while cores in the same processor are in a shared address space. The address space has a significant influence on the data exchange [21]. To accommodate the hybrid address space of a PC cluster, the parallel FDTD algorithm in this work employs a two-level programming model, as shown in Fig. 1. The upper level consists of processes created by the main console and assigned in processors while the bottom level is composed of threads created by each process for cores in a processor.

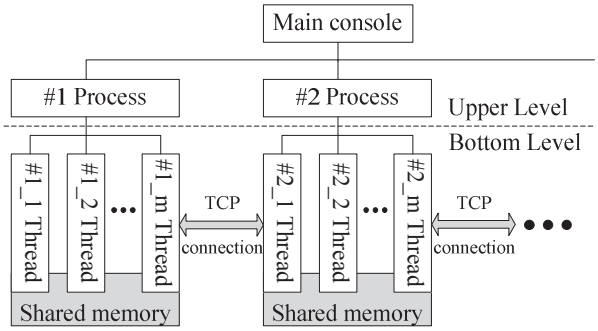

Fig. 1. The two-level programming model for the parallel FDTD.

This work adopts Winsock rather than MPI to realize an inter-process message passing. Winsock defines a standard interface between a Windows TCP/IP client application and the underlying TCP/IP protocol stack [22, 23]. As shown in Fig. 2, a connection using the transmission control protocol (TCP) is established to a specific socket separately on both sides. Once the connection is set up, they can pass messages by calling *send*() and *recv*() .

Explicit threading is employed in the bottom level of the programming model, directly splitting up the computation. The key steps using the Win32 thread API [13] to multi-thread are as follows:

a. A process starts with a single thread of execution. This is called the main thread.
b. This is followed by *_beginthreadex*() being used to create new sub-threads. Those sub-threads can now start their own computation tasks.
c. During the computation, shared variables are used and data exchange is performed by write or read accesses of the threads. Meanwhile, synchronization both coordinates thread execution and manages shared data.
d. When the computation task is finished, each sub-thread calls *_endthreadex*() to terminate.

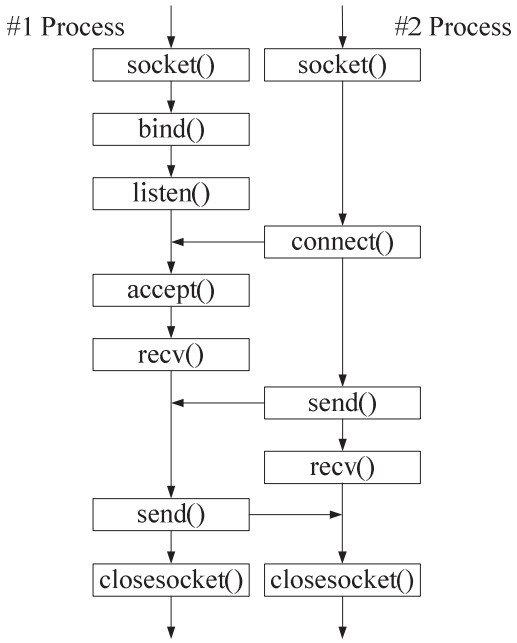

Fig. 2. The flow chart of Winsock programming.

For a better efficiency, a fixed mapping from the threads to the execution cores is employed by calling *SetThreadAffinityMask*() . This prevents threads from migrating to other cores during program execution.

B. Domain decomposition

Figure 3 shows the spatial parallelism used in this work that divides the whole computation space into sub-domains. Each sub-domain is assigned to one process for parallel computation. In each sub-domain, additional pages, called expand pages, are introduced to store field values from neighbors' interface for data exchange. Every process creates threads according to the

number of execution cores employed in the parallel computation, splits a sub-domain further into smaller sub-domains, and then assigns them to each thread. For threads in the same process, field values stored in shared variables are mutually directly accessible, thus eliminating the need for expanded pages.

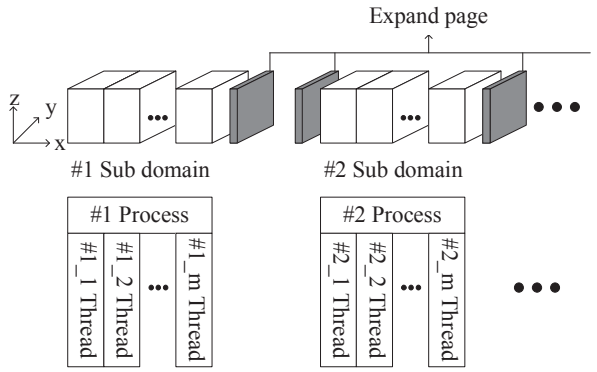

Fig. 3. Domain decomposition.

C. Synchronization

At each time step of FDTD, the update of the electric and magnetic fields are executed sequentially. Execution of threads in the wrong order may produce unwanted outputs. Figure 4 illustrates the synchronization mechanism adopted in this work, where N is the number of sub-threads, and *count* is defined as a volatile integer. *InterlockedIncrement*64(&*count*) increases by 1 the value of variable *count* as an atomic operation, and *InterlockedExchange*64(&*count*, 0) sets variable *count* to 0 as an atomic operation as well.

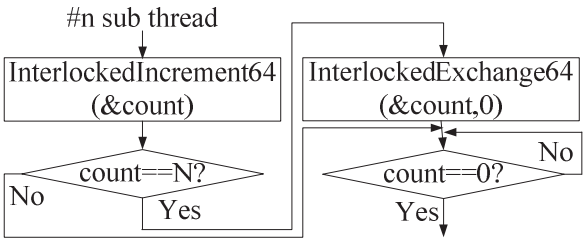

Fig. 4. The synchronization mechanism.

D. Data exchange

According to the FDTD updated equations, for cells on the interfaces between two adjacent sub-domains, the field data on the neighboring threads are required, necessitating the execution of data exchange. For threads on the same processor, data exchange is done by shared E and H variables directly written by one thread and read by another. As for threads on different processors, messages containing E and H values are passed by explicitly calling the Winsock API: *send*() and *recv*() [23].

Data exchange is one of the main factors affecting the parallel efficiency, along with synchronization and load balancing. This work utilizes an overlapping scheme [7], i.e. the interface of adjacent sub-domains assigned to two processes is overlapped, on which the electric field components are updated in both neighboring threads created by separate processes, shown in Fig. 5. Although the electric field components on the interface are calculated twice, only magnetic field components are transmitted at each time step. However, the overlapping scheme does not apply to the threads created in the same process due to the use of shared variables; otherwise data race occurs, leading to calculation errors.

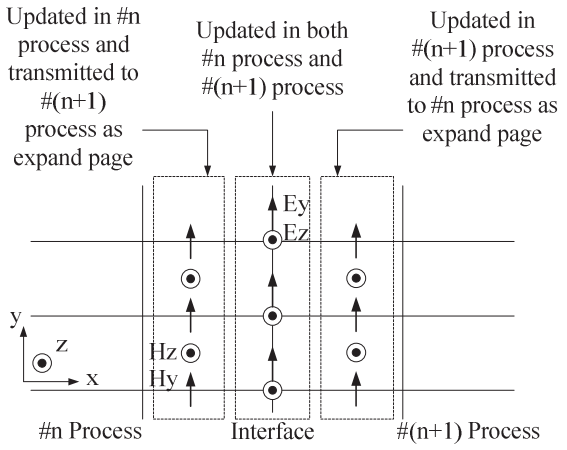

Fig. 5. The field exchange configuration employing the overlapping scheme.

E. Load balancing

Load balancing is a critical issue for a parallel computation to achieve high efficiency [24]. For the parallel FDTD, a good load balancing strategy should suitably divide computation space so that every thread is equal in actual execution duration between any two succeeding operations of synchronization, avoiding idle conditions owing

to mutual waiting. One of crucial factors affecting load balancing is various cells such as ordinary cells and PML cells, due to the different workloads that they possess. However, no specific rule exists for evaluating this factor in the domain decomposition, just experience acquired from repeated experiments. Our experiments show that a PML cell requires approximately 2.6 times more computing time than that of an ordinary cell. So a PML cell is evaluated as 2.6 ordinary cells when the whole space is divided into sub-domains.

F. The thread execution

A thread carries out the actual FDTD calculation, as illustrated in Fig. 6. Electric and magnetic fields are updated sequentially, each followed by a synchronization operation. If a thread possesses a sub-domain interface between neighboring nodes, exchange of the magnetic field components with neighboring processes, through sending and receiving operations, is performed upon update of the magnetic field.

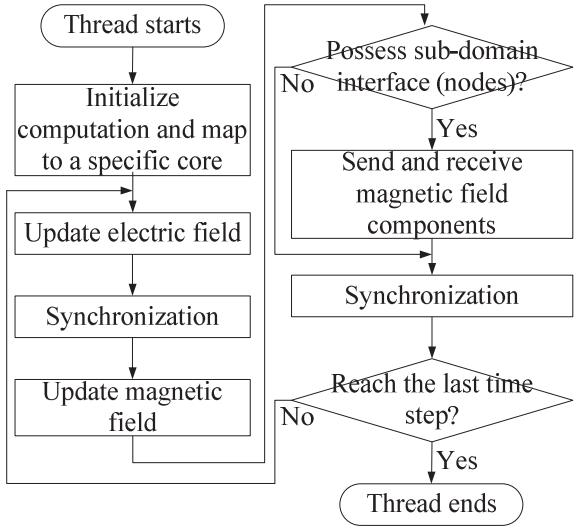

Fig. 6. The flow chart of the thread execution.

optimizations for multi-core processors. The MPI based code creates a process binding to each execution core, and the data exchange between two cores is realized by calling MPI_Sendrecv(), just like that between two processors. Channel Nemesis is chosen to optimize intranode and internode communication. The MPI-OpenMP based code is similar to the pure MPI code. It creates a process in each processor, and employs OpenMP to automatically parallelize to the computing loops [15, 19], shown in Fig. 7. The *parallel* pragma is hoisted outside the loop of time steps to minimize threading overhead. When synchronization is not a necessity at the end of a parallel loop, *nowait* is specified with the *for* directive. Thread binding is achieved by calling $SetThreadAffinityMask()$.

```
Do initialization work;
#pragma omp parallel private (…)
{
for timestep=0 to timestep_max
   {
   …
   #pragma omp for private (…) nowait
   computation loops;
   …
   #pragma omp master
   {
   MPI_Sendrecv();
   }
   #pragma omp barrier
   }
}
```

Fig. 7. MPI-OpenMP algorithm.

IV. RESULTS AND ANALYSIS

To estimate the parallel performance of the proposed method, three parallel FDTD codes based on the proposed method, the MPI library, and MPI-OpenMP, respectively, are developed in Visual Studio 2010. The implementation of MPI used in this paper is MPICH2-1.3.1, the latest version supporting the MPI 2.0 standard and

As depicted in Fig. 8, an electromagnetic plane wave with a frequency of 1GHz propagates to a computer case, and the three parallel FDTD codes are employed to simulate the scattered field of the computer case. For this scattered field problem, its whole computation space is discreted into $720*170*330$ cells along x, y, and z axis, respectively, with $dx = dy = dz = 0.001m$.

The experiment is carried out on a PC cluster comprising Intel Q6600 processors interconnected by a fast 1000Mb/s Ethernet. Each processor possesses 4 cores; in the experiment, one core is left to process system work and up to three cores can be used for the parallel FDTD computation.

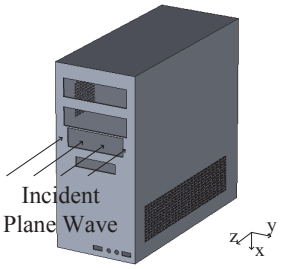

Fig. 8. The computation model.

The scattered field simulated by the three parallel FDTD codes agrees well with the simulation by computer simulation technology (CST) Microwave Studio. Table 1 demonstrates the tested run time and memory consumption of the three parallel FDTD codes, which drop quickly upon introduction of more threads/processes. One can see that the proposed method always costs less run time in comparison with both the MPI based and the MPI-OpenMP based parallel FDTD, and three codes consume the same amount of memory.

Table 1: Run time (in seconds) and memory consumption (in MB)

Number of threads/processes		1	6	12	18	24	30
Run time	The proposed method	7092	1257	648	444	344	282
	MPI	7092	1292	661	468	377	309
	MPI-OpenMP	7092	1268	655	449	346	284
Memory Consumption		2950	1500	775	412	231	140

Figure 9 gives the measured speedup and parallel efficiency for the three parallel FDTD codes. Here, speedup is the ratio of sequential implementation execution time and parallel

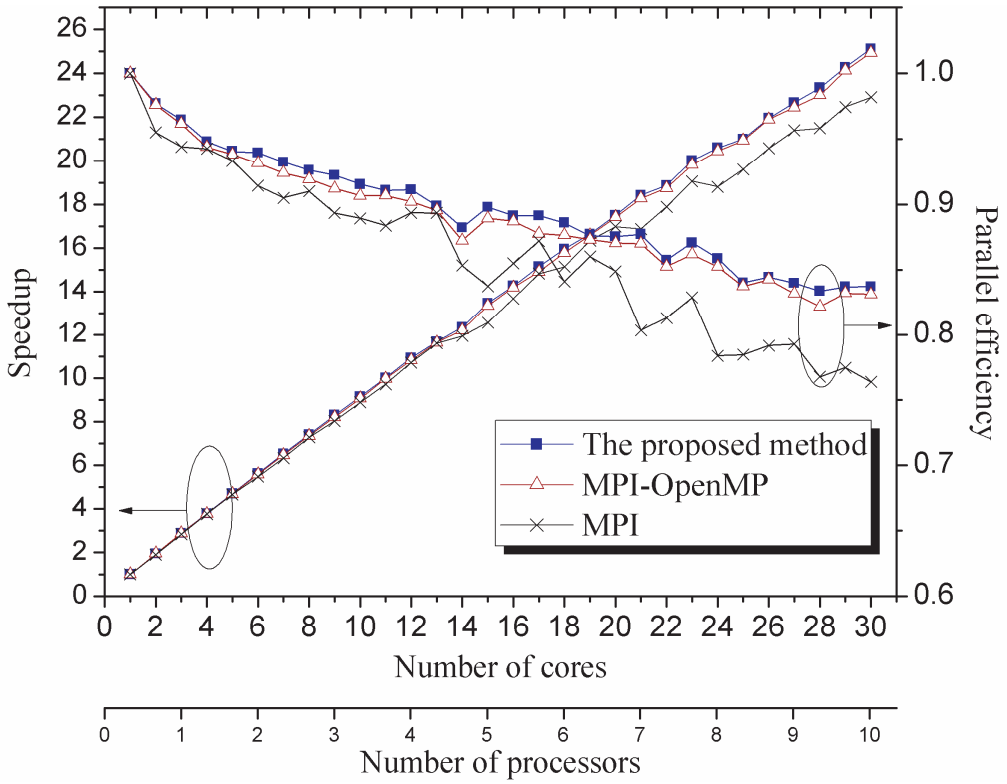

Fig. 9. Speedup and parallel efficiency.

execution time, while parallel efficiency is equal to speedup divided by the number of cores employed. One can observe that the speedup and parallel efficiency of the proposed method is considerably higher than that of the MPI based FDTD and the discrepancy becomes even larger with the increase of the number of cores. Compared with the MPI-OpenMP version of FDTD, the proposed method's speedup and parallel efficiency is slightly bigger, but it is worth noting that the former is more difficult to optimize because it needs a careful fine tuning to achieve good performances. When 30 cores are utilized, the proposed method's speedup rises to 25.1 with parallel efficiency of 83.7%, while the MPI application's speedup is 22.9 with parallel efficiency of 76.3% and the MPI-OpenMP application's speedup is 24.9 with parallel efficiency of 83.1%.

V. CONCLUSION

Today's PC clusters have improved remarkably in their computation ability by utilizing powerful new hardware, such as processors integrated with multiple cores. Parallel FDTD should be carefully designed to make full use of PC clusters' multi-processor and multi-core features. This paper presents a high performance parallel FDTD method using Winsock and multi-threading to parallelize the FDTD computation. Threads are created to do the sub-domain computation in each execution core. Neighboring threads that are on the same nodes directly access each others' memory during data exchange. Winsock sets up TCP connections between neighboring threads that run on different nodes to pass messages. Meanwhile, some techniques have been utilized to improve the parallel FDTD's synchronization, data exchange, load balancing, and etc.

A numerical experiment of simulating a scattered field problem on a PC cluster with multi-core processors has been conducted to verify the validation and efficiency of the proposed method. In the experiment, the proposed method exhibits higher speed up and parallel efficiency than the FDTD using MPI or MPI-OpenMP. Moreover, the proposed method is natural and easy to implement for a good performance due to its explicit and direct threading. Those features make the method widely usable in numerical simulation problems.

ACKNOWLEDGEMENT

This work was supported by NCET of China (No. NCET-08-0369) and the National Natural Science Foundation of China (No. 10876020).

REFERENCES

[1] K. Yee, "Numerical Solution of Initial Boundary Value Problems Involving Maxwell's Equations in Isotropic Media," *IEEE Transactions on Antennas and Propagation*, vol. 14, no.3, pp. 302-307, 1966.

[2] A. Taflove, *Computational Electromagnetics: The Finite-Difference Time-Domain Method*, Artech House, Norwood, 2000.

[3] C. Guiffaut and K. Mahdjoubi, "A Parallel FDTD Algorithm using the MPI Library," *IEEE Antennas and Propagation Magazine*, vol. 43, no. 2, pp. 94-103, 2001.

[4] G. A. Schiavone, I. Codreanu, R. Palaniappan, and P. Wahid, "FDTD Speedups Obtained in Distributed Computing on a Linux Workstation Cluster," *Antennas and Propagation Society International Symposium*, vol. 3, pp. 1336-1339, 2000.

[5] V. Varadarajan and R. Mittra, "Finite-Difference Time-Domain (FDTD) Analysis using Distributed Computing," *IEEE Microwave and Guided Wave Letters*, vol. 4, no.5, pp. 144-145, 1994.

[6] W. Yu, R. Mittra, T. Su, Y. Liu, and X. Yang, *Parallel Finite-Difference Time-Domain Method*, Artech House, 2006.

[7] W. Yu, Y. Liu, T. Su, N.-T. Hunag, and R. Mittra, "A Robust Parallel Conformal Finite-Difference Time-Domain Processing Package using the MPI Library," *IEEE Antennas and Propagation Magazine*, vol. 47, no. 3, pp. 39-59, 2005.

[8] W. Yu, M. R. Hashemi, R. Mittra, D. N. de Araujo, M. Cases, N. Pham, E. Matoglu, P. Patel, and B. Herrman, "Massively Parallel Conformal FDTD on a BlueGene Supercomputer," *IEEE Transactions on Advanced Packaging*, vol. 30, no. 2, pp. 335-341, 2007.

[9] M. Snir, S. Otto, S. Huss-Lederman, D. Walker, and J. Dongarra, *MPI: The Complete Reference,* The MIT Press, 1996.

[10] W. Gropp, E. Lusk, and A. Skjellum, *Using MPI: Portable Parallel Programming with the Message-Passing Interface, second edition*, The MIT Press, 1999.

[11] D. Buntinas, G. Mercier, and W. Gropp, "Implementation and Shared-Memory Evaluation of MPICH2 over the Nemesis Communication Subsystem," *Proc. of the 13th European PVM/MPI Users' Group Meeting (Euro PVM/MPI 2006)*, September 2006.

[12] D. Buntinas, G. Mercier, and W. Gropp, "Design and Evaluation of Nemesis, A Scalable Low-Latency Message-Passing Communication Subsystem," *Proceedings of International Symposium on Cluster Computing and the Grid 2006 (CCGRID '06)*, 2006.

[13] S. Akhter and J. Roberts, *Multi-Core Programming: Increasing Performance through Software Multi-threading*, Intel Press, 2006.

[14] F. Cappello and D. Etiemble, "MPI Versus MPI+OpenMP on the IBM SP for the NAS Benchmarks," *Supercomputing ACM/IEEE 2000 Conference*, 2000.

[15] M. F. Su, I. El-Kady, D. A. Bader, and S.-Y. Lin, "A Novel FDTD Application Featuring OpenMP-MPI Hybrid Parallelization," *Parallel Processing, 2004 International Conference*, pp. 373-379, 2004.

[16] R. Rosenberg, G. Norton, J. C. Novarini, W. Aderson, and M. Lanzagorta, "Modeling Pulse Propagation and Scattering in a Dispersive Medium: Performance of MPI/OpenMP Hybrid Code," *SC 2006 Conference, Proceeding of the 2006 ACM/IEEE*, pp. 47-47, 2006.

[17] B. Chapman, G. Jost, and R. Van Der Pas, *Using OpenMP: Portable Shared Memory Parallel Programming*, The MIT Press, 2008.

[18] R. Chandra, L. Dagum, D. Kohr, D. Maydan, J. McDonald, and R. Menon, *Parallel Programming in OpenMP*, Academic Press, 2001.

[19] A. Rane and D. Stanzione, "Experiences in Tuning Performance of Hybrid MPI/OpenMP Applications on Quad-Core Systems," *Proc. of 10th LCI Int'l Conference on High-Performance Clustered Computing*, 2009.

[20] J. Berenger, "A Perfectly Matched Layer Medium for the Absorption of Electromagnetic Waves," *J. Comput.*, vol. 114, 1994, pp. 185-200.

[21] T. Rauber and G. Rünger, *Parallel Programming for Multicore and Cluster Systems*, Springer, 2010.

[22] A. Jones and J. Ohlund, *Network Programming for Microsoft Windows*, Microsoft Press, 2002.

[23] B. Quinn and D. Shute, *Windows Sockets Network Programming*, Addison-Wesley Professional, 2009.

[24] J. Watts and S. Taylor, "A Practical Approach to Dynamic Load Balancing," *IEEE Transactions on Parallel and Distributed Systems*, vol. 9, no. 3, pp. 235-248, 1998.

Xin Duan was born on May 23, 1986 in Sichuan, China. He received his B.S. degree in Information and Communication Engineering in 2008 from Sichuan University. He is now working toward his M.S. degree in Electromagnetics and Microwave in Sichuan University. His research is mainly focused on computational electromagnetics and antenna design.

Xing Chen received his M.S. degree in Radio Physics in 1999 and the Ph.D. degrees in Biomedical Engineering in 2004, both from Sichuan University, China. He joined the teaching staff in 1991, and is now a Professor in the College of Electronics and Information Engineering of Sichuan University. His main research interests are in the fields of antenna design, optimization algorithm, numerical methods, and parallel computation. He is a senior member of the Chinese Institute of Electronics.

Kama Huang received his M.S. degree in 1988 and his Ph.D. degree in 1991 in Microwave Theory and Technology both from the University of Electronic Science and Technology, China. He has been a professor of the College of Electronics and Information Engineering of Sichuan University, China since 1994, and the director of the College since 1997. In 1996, 1997, 1999, and 2001, he was a visiting scientist at the Scientific Research Center "Vidhuk" in the Ukraine, Institute of Biophysics CNR in Italy, Technical University Vienna in Austria, and Clemson University in USA, respectively. At these institutions, he cooperated with the scientists to study the interaction between electromagnetic fields and complex media in biological structure and reaction systems. He has published over one hundred papers.

Haijing Zhou was born in Beijing in 1970. He received his B.S., M.S., and Ph.D. degrees in Microwave engineering in 1991, 1994, and 1997, respectively, from UESTC (University of Electronics Science and Technology of China). Since 1998, he has been working at IAPCM (Institute of Applied Physics and Computational Mathematics of Beijing), as an Associated Professor (1999) and a Professor (2005), where his research is mainly in the areas of high power microwave, ultra-wideband electromagnetics, and computational electromagnetics. His current interests include classical electromagnetic field theory, transient electromagnetics, computational electromagnetics, microwave technology, antenna technology, and wave propagation, etc.

Negative Index of Reflection in Planar Metamaterial Composed of Single Split-Ring Resonators

Ming-Chun Tang, Shaoqiu Xiao, Duo Wang, Jiang Xiong, Kun Chen, and Bingzhong Wang

The Institute of Applied Physics
University of Electronic Science and Technology of China, Chengdu, China, 610054
xiaoshaoqiu@uestc.edu.cn

Abstract - This paper reports the negative index of refraction in planar metamaterial consisted of only a traditional single split-ring resonator (SRR), which is proved to exhibit simultaneously negative permittivity and negative permeability without the use of assistant metallic structures by retrieving the effective electromagnetic parameters. With the aid of current distributions investigation, it is demonstrated that within the left-handed band the negative permittivity is generated in a way analogous to the case of dual parallel cut-wire metamaterial, and negative permeability arises from the asymmetric second-order magnetic resonant mode.

Index Terms - Negative index reflection, negative permeability, negative permittivity, planar metamaterial, single SRR.

I. Introduction

In 2001, the fantastic negative refraction was accomplished by a prism made of left-handed material (LHM) [1, 2], which had been previously predicated by Veselago [3]. Since then, various kinds of LHMs have been constructed, such as SRR-shaped [4], Ω-shaped [5], brick-wall-shaped [6], cut-wire-shaped [7], S-shaped [8, 9], right-angle-shaped [10], H-shaped [11], chirality-shaped [12] resonators, and so on. Typically, these LHMs designs can be classified into two categories: one, like those reported in [1 and 4], is realized from separate arrays of periodically arranged split ring resonators that exhibit negative permeability and metallic wires that exhibit negative permittivity; the other, as proposed in [5–12], only uses sub-wavelength structures which incorporate traditional wires and SRRs into different combined patterns with simultaneous electric and magnetic resonances. However, most of these LHMs share certain defects. For example, most metallic patterns are printed on both sides of the substrates [1, 5-8], and some lumped active elements (such as varactor diodes) are added in the design [8, 9], both of which increase the complexity of design and application; some LHMs resort to composite metamaterial units [10] or bear too long unit length along the electric polarized direction [11, 12], whose unit cell takes up too much space accordingly.

Given that their performances are qualitatively similar to those of double split-ring resonators (SRRs) [13], single SRRs have been utilized to design different kinds of metallic metamaterials, recently. As their electric resonance properties are just like cut wires, they have already seen applications in fabricating planar electric metamaterials [14-16]. On the other hand, being able to generate circulating currents, they have also been used to realize magnetic resonances [17-22]. Generally, a LHM could only function on the condition that the negative electric and magnetic responses are modulated to a common frequency band [1, 3]. However, since an ordinary single SRR has a much lower fundamental magnetic resonance frequency than that of the electric resonance, it is impossible to achieve a common frequency band after modulation. Therefore, no LHM composed of single SRR units have been reported yet.

In this paper, after a thorough numerical investigation of the resonance characteristics of a single SRR, we propose one new method to design LHM with a single SRR unit. In the design, we utilize the magnetic resonant frequency in asymmetrical second-order mode, and the electric resonant frequency in fundamental electric resonant mode. The two frequency bands, after subtle adjustment of unit dimension, are accommodated to

overlap very well; thus, contributing to the accomplishment of our expected LHM. It is of interest that, without resorting to additional lumped active elements or metallic cut wires, the proposed LHM unit is easily achieved and boasts a simple and uniform configuration.

II. NUMERICAL INVESTIGATION ON AN ORDINARY SINGLE SRR

The unit cell of an ordinary metallic single SRR metamaterial is schematically shown in Fig. 1. The single split ring with a thickness of 0.0017 mm is placed in the center of the cube with the dimensions $L_x \times L_y \times L_z$=15mm×15mm×15mm, and the cube is filled with Rogers RT/duroid 5880 with relative dielectric constant ε_r=2.2. The detailed geometry of SRR is: the gap of ring g=1mm, the outer radius R=6mm, and the width w=1.1mm.

The numerical simulations are all performed using the finite-element method (Ansoft's HFSS), whose accuracy has been already confirmed by its good agreement with experimental results as in literatures [23, 24]. A theoretical model based on an artificial waveguide with the transverse boundaries of two ideal magnetic conductors and two ideal electric conductor planes is employed. This enables the model to be equivalent to an infinite layer medium illuminated by a normal incident plane wave [25-27]. To be specific, input/output ports are imposed in x-direction, and perfectly electric conducting (PEC) and perfectly magnetic conducting (PMC) boundary conditions are imposed in y- and z- directions, respectively. It is noted that, the electric component of the electromagnetic wave perpendicular to the split bearing side of the ring (along y-axis) is adopted for the sake of eliminating the undesired bi-anisotropic effect via asymmetry [27, 28].

At first, we discuss the condition in Fig. 2. As sketched, the single SRR is placed where the electromagnetic wave propagates (in the x-direction) perpendicular to the SRR face (in the yz-plane) and external polarized magnetic field (in the z-direction) is parallel to its face. Shown in the simulated transmission spectrum, the SRR can be electrically excited around 7.35GHz (i.e., in the fundamental electric resonant mode), in agreement with the theoretical analysis in literature [29]. Further, the induced current distribution at 7.35GHz is presented. Obviously, the charge accumulates symmetrically on opposite arms of the ring, and the ring is in analogy to the dual parallel connected cut-wires of the same dimensions. Thus, the ring can be viewed as two parallel LC resonant circuits operating in the fundamental modes. Owing to the same dimensions of the two arms, the two LC resonances are both operating in the same fundamental electric resonant frequency band.

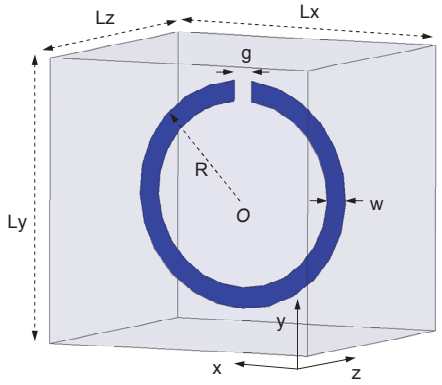

Fig. 1. The unit cell of the metallic metamaterial designed with single SRR.

Then, we rotate the SRR around y- axis for 90° in xz plane, shown in Fig. 3. In this simulation, the single SRR is placed where the electromagnetic wave propagates (in the x-direction) parallel to the SRR face (in the xy-plane). An external polarized magnetic field (in the z-direction) is perpendicular to its face, which can induce magnetic response in addition to electric response. The corresponding simulated transmission spectrum is, also, presented in Fig. 3. There are three dips appearing within this frequency region. As is aforementioned, the third dip at 7.35GHz results from the external electric excitation. Therefore, the other two dips (including 2.7GHz and 6.35GHz) could only be caused by external magnetic excitation, since the bi-anisotropic effect has been eliminated [28].

In order to confirm its resonance mechanism, the current distributions at each dip are demonstrated in Fig. 4. It is obvious that the circling current is induced by the external magnetic field, which incurs a magnetic response in fundamental mode around 2.7GHz in Fig. 4(a) [22]. Naturally, the corresponding second-order mode (i.e., the dip at 6.35GHz in Fig. 3) could occur at a higher resonant frequency. For clarity, the current distributions at the higher mode are demonstrated in Fig. 4(b). It is noted that, the current distribution in second-mode is

non-uniform and asymmetric [30]. This can be ascribed to the following two main reasons; one is that there is no intrinsic symmetric even-mode current distributions existing based on magnetic excitation in this type of SRR. As is well known, the polarization currents are directly contributed by external magnetic field [13, 31], whenever the SRR is excited at the arbitrary-order magnetic resonant modes. It can be assumed that, if the magnetic resonances in even-modes were symmetric, the current distributions should also be symmetrically distributed at the two arms (just like aforementioned electric resonance in fundamental mode in Fig. 2). Eventually, it would lead the sum of the even-mode response for the external magnetic field to be zero, i.e., the external magnetic field would make no contribution to the overall SRR magnetic response. The other reason is that, the other kind of response (electric response in the fundamental mode at 7.35GHz) is quite near to the magnetic response in the second-mode 6.35GHz in Fig. 3, and those nearby responses could exhibit mutual coupling between each other, which disturbs current distributions. For the electric resonance in the fundamental mode, because of the influence of nearby magnetic excitation, the current distributions induced by the external electric field in the two paralleled arms depicted in Fig.4(c) are apparently not as symmetric as in Fig. 2

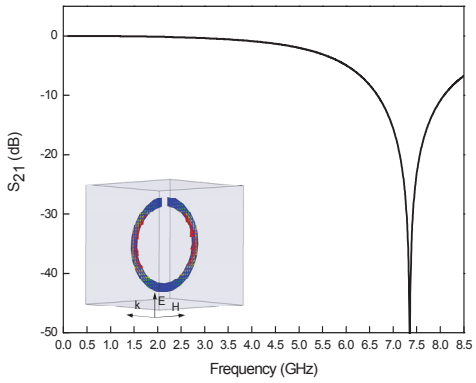

Fig. 2. The simulated transmission spectrum and current distribution (at the dip 7.35GHz), when the single SRR is only electric excited.

III. NEGATIVE INDEX OF REFRACTION ENABLED BY SINGLE SRRS

As is known, negative permittivity can be achieved by the electric resonance, and negative permeability can be ensured by magnetic resonance analogously. It is aforementioned in Section II that the ordinary single SRR would usually exhibit electric resonance and magnetic resonance at different frequencies, as shown in Fig. 3. However, negative refraction requires a negative permittivity and a negative permeability at a common frequency range, which necessitates certain overlapping frequency range of the electric resonance and magnetic resonance frequency of single SRR.

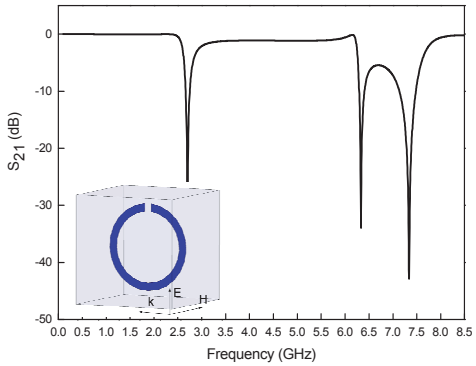

Fig. 3. The simulated transmission spectrum on the condition that the single SRR is both electrically and magnetically excited.

Considering the electric resonant frequency in fundamental mode is near to the magnetic resonant frequency in second-order mode, a parametric study is carried out in order to make the two resonance frequency bands closer by adjusting the SRR dimensions as shown in Fig. 5. Firstly, the effect of the split gap (g) is numerically studied. From Fig. 5(a), it is observed that the split gap has little impact on the distance between the two resonance frequency bands. When the split gap becomes

larger, the electric resonance frequency goes up in accordance with the two magnetic resonance frequencies. The main reason is that the enlargement of split gap results in the reduction of the effective electric length along the E-polarized direction induced by an external electric field, and the decrease of the effective circulating current path and split capacitance induced by an external magnetic field. This leads to the increase of electric resonance frequency (ω_{eo}) and each magnetic resonance frequency (ω_{mo}). The effect of the SRR width (w) has also been studied in Fig. 5(b). As mentioned above, the single SRR is in analogy to the dual

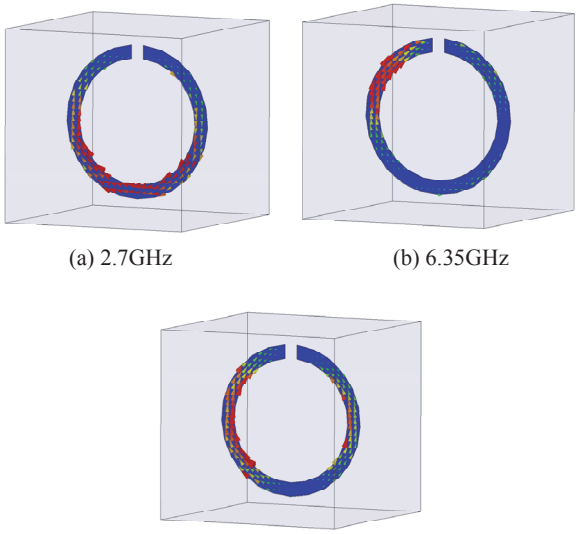

(a) 2.7GHz (b) 6.35GHz

(c) 7.35GHz

Fig. 4. Current distributions at three different resonant dips. (a) The fundamental magnetic resonant frequency; (b) The second-order magnetic resonant frequency; (c) The fundamental electric resonant frequency.

parallel connected cut wires. Hence, by decreasing the width of SRR (which is equivalent to the effective radius of cut wire in literature [32]), the corresponding ω_{eo} drops distinctly. Meanwhile, its influence on the ω_{mo} can be neglected except a little variation due to the small difference in split capacitance. Therefore, in Fig. 5(b) it is of our interest that, when w goes narrower, the above two resonant frequencies get closer. Especially, the two resonant frequency regions occupy overlapping band (in the dotted zone) when w=0.2mm, leading to a narrow passband centered at 6.4GHz occurrence. Thirdly, the effect of the radius (R) of metallic SRR on the resonance frequency has been investigated shown in Fig. 5(c). When the radius (R) goes up, both of the ω_{eo} and ω_{mo} are simultaneously dropping. We ascribe this phenomenon to that, the increase of R brings about the corresponding enlargement of the effective electric length along the E-polarized direction induced by an external electric field, and also the increase of the effective circulating current path induced by an external magnetic field, simultaneously.

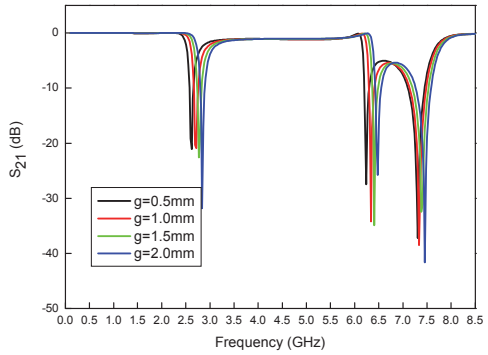

(a)

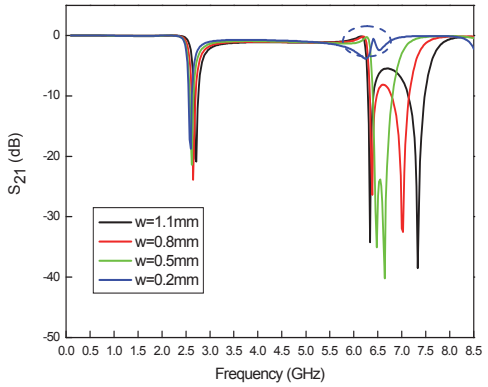

(b)

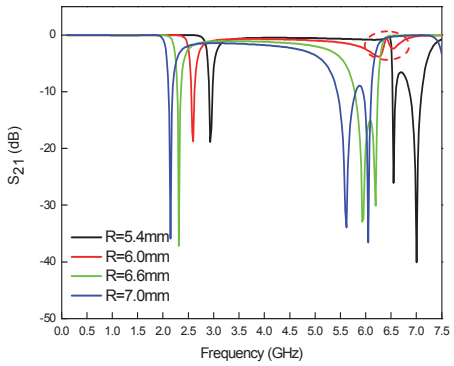

(c)

Fig. 5. The effect of metallic SRR dimensions on the resonance frequency; (a) the split gap (*g*), (b) the width (*w*), the radius (*R*).

Furthermore, in order to judge the existence of the electric resonance around 6.4GHz in Fig. 5 easily, we also rotate the SRR around *y*- axis for 90° in *xz* plane, with the electromagnetic environment the same as Fig. 2. Fig. 6(a) demonstrates that the SRR provides a stopband near 6.1GHz, exhibiting strong electric response (according to the current distribution on the two arms at the dip 6.1GHz) in analogy with the simulated result in Fig. 2. It verifies that there is also a strong electric resonance occurring within the passband. Logically, the magnetic resonance also exists in the passband to ensure negative index of refraction. Moreover, Fig. 6(b) shows the effect of SRR width (*w*) on the resonance frequency, when the single SRR is only electric excited (i.e., it is placed in the same electromagnetic environment as that in Fig. 6(a)). Apparently, when the *W* goes narrower, the electric resonance frequency (ω_{eo}) drops distinctly (from 7.24GHz to 7.10GHz), which is in good accordance with the results in Fig. 5(b), thus confirming the validation of our aforementioned theory [32].

To further confirm the effectiveness of our proposed LHM design, a retrieval calculation is performed to obtain the effective permittivity ε_{eff} and the effective permeability μ_{eff} from the scattering parameters S_{21} and S_{11} of the proposed SRR metamaterial. According to literature [33],

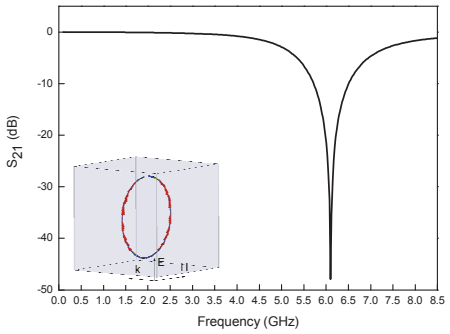

(a)

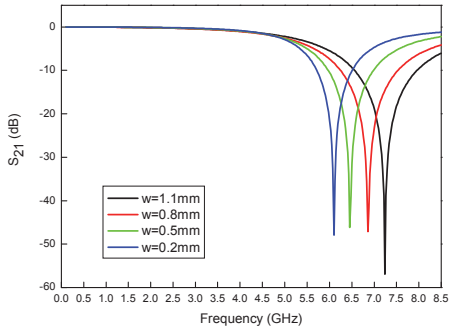

(b)

Fig. 6. The simulated transmission spectrum when the single SRR is only electric excited; (a) the transmission spectrum and the current distribution (at the dip 6.1GHz), (b) the effect of SRR width (*w*) on the resonance frequency.

in order to attain electrometric parameters (including permittivity and permeability), the refractive index (*n*) and the wave impedance (*z*) is firstly obtained from Equations (1) and (2), respectively, and then the electrometric parameters are acquired from Equations (3) and (4), respectively.

$$n = \frac{1}{kd}\cos^{-1}\left[\frac{1}{2S_{21}}\left(1 - S_{11}^2 + S_{21}^2\right)\right]. \quad (1)$$

$$z = \sqrt{\frac{\left(1+S_{11}\right)^2 - S_{21}^2}{\left(1-S_{11}\right)^2 - S_{21}^2}}. \quad (2)$$

$$\varepsilon = n/z. \quad (3)$$

$$\mu = nz. \quad (4)$$

It is noted, in the retrieval procedure the Kramers–Kronig relations is applied to achieve the uniqueness of their values here [34]. The retrieved results in Fig. 7 demonstrate that, within the negative refractive index frequency band, the ε_{eff} and μ_{eff} are simultaneously negative corresponding to the passband region from 6.34GHz to 6.45GHz, which is also the overlapping region between fundamental electric resonant frequency band and second-order magnetic resonant frequency band. Thus, the retrieved datas are consistent with the results concluded earlier. Also, Fig. 7 shows the imaginary parts of permittivity and permeability are relative smooth and almost zero, which indicate very weak anti-resonances and low losses of our proposed LHM unit in spite of its very simple configuration [35]. However, it is also worth mentioning that, our proposed LHM can only provide a much narrower bandwidth (with only 3.4% fractional bandwidth) with negative index of reflection than LHM proposed in literature [33].

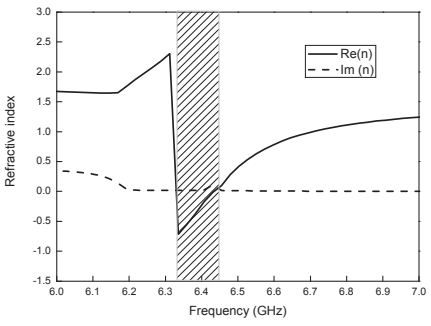

(a)

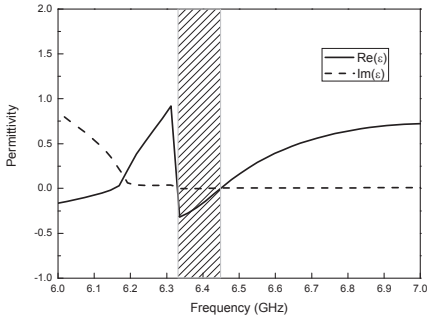

(b)

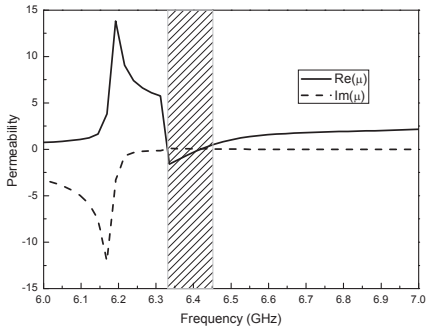

(c)

Fig. 7. Retrieved electromagnetism parameters of the metamaterial composed of SRRs from the scattering parameters in Fig. 5 where both electric and magnetic excitations provided (w=0.2mm); (a) refractive index, (b) permittivity, and (c) permeability.

In addition, the current distributions under different excitations at different phases have been compared and discussed in Fig. 8. Figs. 8(a) and (b) present the current distributions, when the SRR is excited by time-varying external electric field and magnetic field, respectively [31]. As is well known that, the different resonances come from in phase and out of phase responses of the structure with the driving incident field, due to the different excitations. It is further attested in Fig. 8(a) that the relatively symmetric charge distribution at both arms of SRR is observed when there is only electric excitation, while the majority of charges are accumulated at only one arm when only magnetic excitation provided in Fig. 8 (b). And

it deserves to be mentioned that, the electric response is more significant at phases 90°, and 135°, while magnetic response is more significant at phase 45°. In Fig. 8 (c), the majority of charges accumulate at two arms in approximately symmetrical distribution at phase 135°, just like that in Fig. 8 (b). Meanwhile, the majority of charges accumulate at only one arm at phase 45° also like that in Fig. 8 (a), exhibiting distinctly asymmetric current distributions. This phenomenon that there is also most of the asymmetric current distributions on the two legs at 90° in Fig. 8 (c), can be ascribed to the strong mutual coupling between the magnetic and electric responses centered at the nearby phases (shown in Fig. 8 (a) and 8 (b), respectively). The above phenomenon further validates the existence of the simultaneously electric and magnetic responses, and confirms the accomplishment of the LHM design.

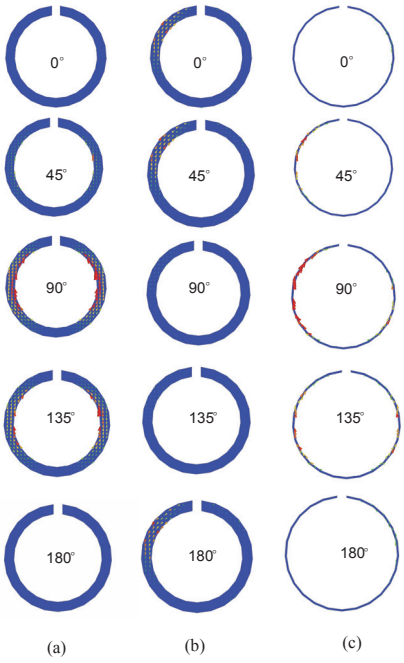

Fig. 8. Current distributions at different phases within half of a period. (a) Only electric excitation at the dip 7.35GHz in Fig. 2; (b) second-order magnetic excitation at the dip 6.35GHz in Fig. 4(b); (c) both electric and magnetic excitations at 6.53GHz for proposed LHM unit.

IV. CONCLUSION

We have numerically investigated the left-handed response in metallic metamaterial comprised of single SRRs. It is learned from simulation data that the electric response in the fundamental mode and magnetic response in second-mode for the traditional single SRR is very near. By adjusting the geometric parameters of the SRR configuration, a simple LHM without using additional metallic wires can be easily realized.

ACKNOWLEDGEMENT

The authors would like to express their thanks to the anonymous reviewers for their careful reading of the manuscript, and their constructive suggestions for the improvement of our work. And the work was in part supported by the National Nature Science Foundation of China (Grant No. 60872034, 60971029), in part by the New-Century Talent Program of the Education Department of China (Grant No. NCET070154), in part by the Funding of State Key Laboratory of Millimeter Waves (Grant No. K 00809), and in part by the Aviation Science foundation (Grant No. 20090180007).

REFERENCES

[1] R. Shelby, D. Smith, and S. Schultz, "Experimental Verification of a Negative Index of Refraction," *Science* 292, **77**, 2001.

[2] G. Monti and L. Tarricone, "Dispersion Analysis of a Negative Group Velocity Medium with MATLAB," *Applied Computational Electromagnetic Society (ACES) Journal* 24, 5, 2009.

[3] V. G. Veselago, "The Electrodynamics of Substances with Simultaneously Negative Values of ε and μ," *Sov. Phys. Usp.* 10, 509, 1968.

[4] R. W. Ziolkowski, "Design, Fabrication, and Testing of Double Negative Metamaterials," *IEEE Trans. Antennas Propag.* 51, 1516, 2003.

[5] L. Ran, J. Huangfu, Y. Li, X. Zhang, K. Chen, and J. A. Kong, "Microwave Solid-State Left-Handed Material with a Broad Bandwidth and an Ultralow Loss," *Phys. Rev. B* 70, 073102,

2004.

[6] H. Chen, L. Ran, J. Huangfu, X. Zhang, K. Chen, T. M. Grzegorczyk, and J. A. Kong, "Negative Refraction of a Combined Double S-Shaped Metamaterial," *Appl. Phys. Lett.* 86, 151909, 2005.

[7] N. T. Tung, V. T. T. Thuy, J. W. Park, J. Y. Rhee, and Y. P. Lee, "Left-Handed Transmission in a Simple Cut-Wire Pair Structure," *J. Appl. Phys.* **107**, 023530, 2010.

[8] H. Chen, L. Ran, J. Huangfu, X. Zhang, K. Chen, T. M. Grzegorczyk, and J. A. Kong, "Left-Handed Materials Composed of Only S-Shaped Resonators," *Phys. Rev. E* 70, 057605, 2004.

[9] D. Wang, L. Ran, H. Chen, and M. Mu, "Experimental Validation of Negative Refraction of Metamaterial Composed of Single Side Paired S-Ring Resonators," *Appl. Phys. Lett.* 90, 254103, 2007.

[10] E. Plum, J. Zhou, J. Dong, V. A. Fedotov, T. Koschny, C. M. Soukoulis, and N. I. Zheludev, "Metamaterial with Negative Index due to Chirality," *Phys. Rev. B* 79, 035407, 2009.

[11] Z. Wang, D. Wang, T. Jiang, L. Peng, J. Huangfu, and L. Ran, "Very Simple Metallic Subwavelength Cell for Constructing Left-Handed Metamaterial," *Appl. Phys. Lett.* 94, 231905, 2009.

[12] Y. -H. Liu, C. -R. Luo, and X. -P. Zhao, "H-Shaped Structure of Left-Handed Metamaterials with Simultaneous Negative Permittivity and Permeability," *Acta Phys. Sin.* 56, 5883, 2007.

[13] J. B. Pendry, A. J. Holden, D. J. Robbins, and W. J. Stewart, "Magnetism from Conductors and Enhanced Nonlinear Phenomena," *IEEE Trans. Microwave Theory Tech.* 47, 2075, 1999.

[14] Y. Yuan, C. Bingham, T. Tyler, S. Palit, T. H. Hand, W. J. Padilla, D. R. Smith, N. M. Jokerst, and S. A. Cummer, "Dual-Band Planar Electric Metamaterial in the Terahertz Regime," *Opt. Express* 16, 9746, 2008.

[15] M. Tang, S. Xiao, T. Deng, and B. Wang, "Novel Folded Single Split Sing Resonator and its Application to Eliminate Scan Blindness in Infinite Phased Array," in *Proceedings of International Symposium on Signals, Systems and Electronics*, 2010, vol.1, p. 274.

[16] W. J. Padilla, A. J. Taylor, C. Highstrete, Mark Lee, R. D. Averitt, "Dynamical Electric and Magnetic Metamaterial Response at Terahertz Frequencies," *Phys. Rev. Lett.* 96, 107401, 2006.

[17] S. Linden, C. Enkrich, M. Wegener, J. Zhou, T. Koschny, C. M. Soukoulis, "Magnetic Response of Metamaterials at 100 Terahertz," *Science* 306, 1351, 2004.

[18] J. Zhou, Th. Koschny, M. Kafesaki, E.N. Economou, J. B. Pendry, and C.M. Soukoulis, "Saturation of the Magnetic Response of Split-Ring Resonators at Optical Frequencies," *Phys. Rev. Lett.* 95, 223902, 2005.

[19] M. V. Gorkunov, S. A. Gredeskul, I. V. Shadrivov, and Y. S. Kivshar, "Effect of Microscopic Disorder on Magnetic Properties of Metamaterials," *Phys. Rev. E* 73, 056605, 2006.

[20] T. F. Gundogdu, I. Tsiapa, A. Kostopoulos, G. Konstantinidis, N. Katsarakis, R. S. Penciu, M. Kafesaki, E. N. Economou, Th. Koschny, and C. M. Soukoulis, "Experimental Demonstration of Negative Magnetic Permeability in Far-Infrared Frequency Regime," *Appl. Phys. Lett.* 89, 084103, 2006.

[21] L. Jelinek, R. Marqués, and M. J. Freire, "Accurate Modeling of Split Ring Metamaterial Lenses for Magnetic Resonance Imaging Applications," *J. Appl. Phys.* 105, 024907, 2009.

[22] A. A. Zharov, I. V. Shadrivov, and Y. S. Kivshar, "Nonlinear Properties of Left-Handed Metamaterials," *Phys. Rev. Lett.* 91, 037401, 2003.

[23] T. J. Yen, W. J. Padilla, N. Fang, D. C. Vier, D. R. Smith, J. B. Pendry, D. N. Basov, and X. Zhang, "Terahertz Magnetic Response from Artificial Materials," *Science* 303, 1494, 2004.

[24] H. T. Chen, W. J. Padilla, J. M. O. Zide, A. C. Gossard, A. J. Taylor, and R. D. Averitt, "Active Terahertz Metamaterial Devices," *Nature* (London) 444, 597, 2006.

[25] M. Beruete, M. Sorolla, and I. Campillo, "Left-Handed Extraordinary Optical Transmission Through a Photonic Crystal of Subwavelength Hole Arrays," *Opt. Express* 14, 5445, 2006.

[26] M. Beruete, I. Campillo, M. Navarro-Cia, F. Falcone, and M. S. Ayza, "Molding Left- or Right-Handed Metamaterials by Stacked Cutoff Metallic Hole Arrays," *IEEE Trans. Antennas*

Propag., 55, 1514, 2007.

[27] P. Ding, E. J. Liang, L. Zhang, Q. Zhou, and Y. X. Yuan, "Antisymmetric Resonant Mode and Negative Refraction in Double-Ring Resonators under Normal-to-Plane Incidence," *Phys. Rev. E* 79, 016604, 2009.

[28] R. Marqués, F. Medina, and R. Rafii-El-Idrissi, "Role of Bianisotropy in Negative Permeability and Left-Handed Metamaterials," *Phys. Rev. B* 65, 144440, 2002.

[29] D. R. Smith, J. Gollub, J. J. Mock, W. J. Padilla, and D. Schurig, "Calculation and Measurement of Bianisotropy in a Split Ring Resonator," *J. Appl. Phys.,* 100, 024507, 2006.

[30] Z. -G. Dong, S. -Y. Lei, M. -X. Xu, H. Liu, T. Li, F. -M. Wang, and S. -N. Zhu, "Negative Index of Refraction in Metallic Metamaterial Comprising Split-Ring Resonators," *Phys. Rev. E* 77, 056609, 2008.

[31] H. Chen, L. Ran, J. Huangfu, T. M. Grzegorczyk, and J. A. Kong, "Equivalent Circuit Model for Left-Handed Metamaterials," *J. Appl. Phys.,* 100, 024915, 2006.

[32] S. I. Maslovski, S. A. Tretyakov, and P. A. Belov, "Wire Media with Negative Effective Permittivity: A Quasi-Static Model," *Microwave Opt. Tech. Lett.,* 35, 47, 2002.

[33] D. R. Smith, D. C. Vier, Th. Koschny, and C. M. Soukoulis, "Electromagnetic Parameter Retrieval from Inhomogeneous Metamaterials," *Phys. Rev. E* 71, 036617, 2005.

[34] Z. Szabó, G. –H. Park, R. Hedge, and E. –P. Li, "A Unique Extraction of Metamaterial Parameters Based on Kramers–Kronig Relationship," *IEEE Trans. Microwave Theory Tech.* 58, 2646, 2010.

[35] T. Koschny, P. Markoš, D. R. Smith, and C. M. Soukoulis, "Resonant and Antiresonant Frequency Dependence of the Effective Parameters of Metamaterials," *Phys. Rev. E* 68, 065602, 2003.

Deformation Effect on Transmission Properties of the One Dimensional Photonic Crystal

Abir Mouldi and Mounir Kanzari

Laboratoire de Photovoltaïque et Matériaux Semi-conducteurs (LPMS),
Ecole Nationale d'Ingénieurs de Tunis BP 37 le Belvédère 1002 Tunis, Tunisie
abir20052002@yahoo.fr , mounir.kanzari@enit.rnu.tn

Abstract ─ We considered the influence of multilayer structure parameters which are the index contrast, the period's number and the reference wavelength on the transmission spectrum of a deformed structure. Deformation was introduced by applying the power law $y = x^{k+1}$.We revealed that the higher optical index contrast enhance the deformation effect on transmission properties of the structure at normal incidence. This work is a detailed study of the effect of the deformation introduced in the multilayer stack according to the mentioned law.

Index Terms ─ Deformation, index contrast, multilayer structure, period's number, reference wavelength, transmission properties.

I. INTRODUCTION

The photonic crystals (PCs) are beginning to have a profound effect on the development of nanoscale devices because they can significantly enhance the interactions between light and matter [1-3]. The properties of photonic crystals are not based on absorption or emission transitions. Instead they are determined by the index of refraction periodicity which can be scaled from submicron dimensions (to control UV/VUV light) to the centimetre scale (to control microwaves) [4,5]. The idea of photonic crystals is to introduce periodicity comparable to the optical wavelength in such a way that a photonic band gap (PBG) is formed. Different users need PCs with different PBG widths. So, flexibility and tunability of the PBG of PCs is crucial for flexible and dynamic nanophotonic circuits in future [6-8]. Chirped structure can be introduced in the photonic crystal to change the PBG. So, not only the quarter wave periodic structures but also the deformed ones have become significant structures of photonic crystals. In this work, the deformation was introduced by applying the power law, so that the coordinates y of the deformed object was determined through the coordinates x of the initial (periodic structure) object in accordance with the following rule: $y = x^{k+1}$. Here k is the coefficient defining the asymmetry degree [9-12]. For example, the periodic structure is projected into itself without any changes of dimensions if $k = 0$. Deviation of the k value from 0 leads to a deformed multilayer structure. This deformation occurs when its interest by the optimization of the deformation degree; but this optimization is not simple, it depends on the structure parameters such as the optical contrast ratio (the ratio of high refractive to low refractive index), the number of periods, and the reference wavelength. Within this, the present work considers the study of the deformed 1D-PCs behaviour when varying these parameters. So, we treat the interaction between the deformation degree k and the other parameters of the structure in aim to optimize the structure by widening the PBG at normal incidence. Through this study, we become able to control the PBG properties of the deformed system by controlling the structure parameters. The numerical method employed to obtain the transmission response of the structure is the transfer matrix method.

II. METHOD OF MODELING

For the calculation of system reflection and transmission, we employed the transfer matrix method (TMM). This technique is a finite

difference method particularly well suited to the study of PBG materials and it can solve the standard problem of the photonic band structures and the scattering (transmission, reflection, and absorption) spectrum [13].

It is based on the Abeles method in terms of forward and backward propagating electric field, that is, E^+ and E^- which were introduced to calculate the reflection and transmission. Abeles showed that the relation between the amplitudes [14] of the electric fields of the incident wave E_0^+, reflected wave E_0^-, and the transmitted wave after *m* layers, E_{m+1}^+, is expressed as the following matrix for stratified films within *m* layers:

$$\begin{pmatrix} E_0^+ \\ E_0^- \end{pmatrix} = \frac{C_1 C_2 C_3 ... C_{m+1}}{t_1 t_2 t_3 ... t_{m+1}} \begin{pmatrix} E_{m+1}^+ \\ E_{m+1}^- \end{pmatrix}. \quad (1)$$

Here, C_j is the propagation matrix with the matrix elements.

$$C_j = \begin{pmatrix} \exp\left(i\varphi_{j-1}\right) & r_j \exp\left(-i\varphi_{j-1}\right) \\ r_j \exp\left(i\varphi_{j-1}\right) & \exp\left(-i\varphi_{j-1}\right) \end{pmatrix}, \quad (2)$$

where t_j and r_j are the Fresnel transmission and reflection coefficients, respectively, between the $(j-1)^{th}$ and j^{th} layer. The Fresnel coefficients t_j and r_j can be expressed as follows by using the complex refractive index $\hat{n}_j = n_j + ik_j$ and the complex refractive angle θ_j. For parallel (P) polarization

$$r_{jp} = \frac{\hat{n}_{j-1}\cos\theta_j - \hat{n}_j \cos\theta_{j-1}}{\hat{n}_{j-1}\cos\theta_j + \hat{n}_j \cos\theta_{j-1}}, \quad (3)$$

$$t_{jp} = \frac{2\hat{n}_{j-1}\cos\theta_{j-1}}{\hat{n}_{j-1}\cos\theta_j + \hat{n}_j \cos\theta_{j-1}}. \quad (4)$$

Moreover, for perpendicular (S) polarization:

$$r_{jp} = \frac{\hat{n}_{j-1}\cos\theta_{j-1} - \hat{n}_j \cos\theta_j}{\hat{n}_{j-1}\cos\theta_{j-1} + \hat{n}_j \cos\theta_j}, \quad (5)$$

$$t_{jp} = 2\frac{\hat{n}_{j-1}\cos\theta_{j-1}}{\hat{n}_{j-1}\cos\theta_{j-1} + \hat{n}_j \cos\theta_j}. \quad (6)$$

The complex refractive indices and the complex angles of incidence obviously follow Snell's law: $\hat{n}_{j-1}\sin\theta_{j-1} = \hat{n}_j \sin\theta_j$ (j = 1, 2… *m*+1). The values ϕ_{j-1} in equation (2) indicate the change in the phase of the wave between $(j-1)th$ and jth boundaries and are expressed by the equation:

$$\varphi_0 = 0, \quad (7)$$

$$\varphi_{j-1} = \frac{2\pi}{\lambda}\hat{n}_{j-1} d_{j-1}\cos\theta_{j-1}. \quad (8)$$

Except for *j* = 1, λ is the wavelength of the incident light in vacuum and d_{j-1} is the thickness of the $(j-1)th$ layer. By putting $E_{m+1}^- = 1$, because there is no reflection from the final phase, Abeles obtained a convenient formula for the total reflection and transmission coefficients, which correspond to the amplitude reflectance *r* and transmittance *t*, respectively, as follows:

$$r = \frac{E_0^-}{E_0^+} = \frac{c}{a}, \quad (9)$$

$$t = \frac{E_{m+1}^+}{E_0^+} = \frac{t_1 t_2 ... t_{m+1}}{a}. \quad (10)$$

The quantities *a* and *c* are the matrix elements of the all product C_j matrix:

$$C_1 C_2 C_3 ... C_{m+1} = \begin{pmatrix} a & b \\ c & d \end{pmatrix}. \quad (11)$$

By using equations (9) and (10), we can easily obtain the energy reflectance *R* as:

$$R = |r|^2. \quad (12)$$

For (S) and (P) polarizations, and the energy transmittance *T* as:

$$T_S = \mathrm{Re}\left(\frac{\hat{n}_{m+1}\cos\theta_{m+1}}{\hat{n}_0\cos\theta_0}\right)|t_S|^2, \quad (13)$$

$$T_P = \mathrm{Re}\left(\frac{\cos\theta_{m+1}/\hat{n}_{m+1}}{\cos\theta_0/\hat{n}_0}\right)\left|\frac{\hat{n}_{m+1}}{\hat{n}_0}t_S\right|^2 = \mathrm{Re}\left(\frac{\hat{n}_{m+1}\cos\theta_{m+1}}{\hat{n}_0\cos\theta_0}\right)|t_P|^2, \quad (14)$$

for S and P polarization, respectively, where Re indicates the real part.

III. MODEL AND FORMALISM

The deformation was introduced by applying a power law, so that the coordinates y which represents the transformed object were determined

using the coordinates x of the initial object in accordance with the following rule:

$$y = x^{k+1}, \quad (15)$$

where k is the deformation degree.

The initial optical phase thickness, when we apply the y function, is:

$$\phi = \frac{2\pi}{\lambda} x_0 \cos\theta. \quad (16)$$

The optical phase thickness of the j[th] layer is:

$$\varphi_j = \frac{2\pi}{\lambda} x_0 [\, j^{k+1} - (j-1)^{k+1}] \cos(\theta_j). \quad (17)$$

Here, $x_0 = \frac{\lambda_0}{4}$ is the optical thickness of each layer of the periodic structure, and λ_0 is the reference wavelength.

For the deformed system, the optical thickness of each layer becomes variable and depends on the j^{th} layer and the deformation degree k. So, the optical thickness of each layer after deformation by the y function takes the following form:

$$x_{0j} = x_0 [\, j^{k+1} - (j-1)^{k+1}]. \quad (18)$$

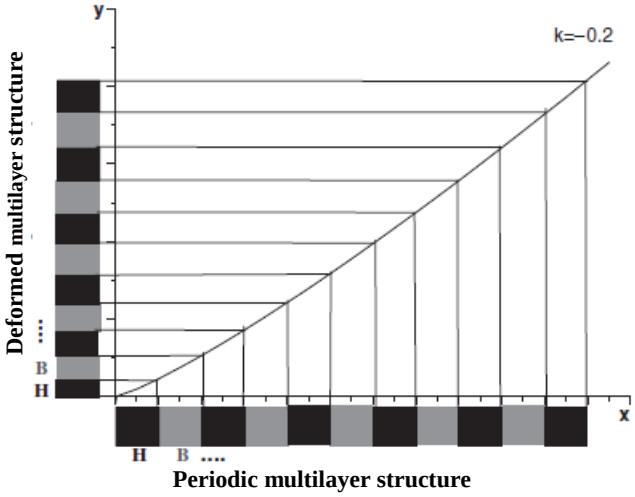

Fig. 1. Principle of introducing a deformation into a periodic multilayer structure, for example for k= -0.2.

It is clear that the optical thickness of each layer increases with k increasing. Figure 1 describes the principle of the transformed system by the y function.

For our study, refractive indices are assumed to be constant in the wavelength region of interest. We define the parameter contrast index x which presents the ratio between the high index and the low index of the layers forming the system $x = \frac{n_H}{n_B}$. The band gap width is defined as the wavelength range when T < 0.01%.

III. STUDY OF DEFORMED STRUCTURE ACCORDING TO THE LAW $y = x^{k+1}$

A. Interaction between the deformation degree and the contrast of indices

The profiles of the optical properties of the system response as a function of k as well as the optimal value of k differ according to the contrast of indices. Figure 2 presents these profiles for some values of contrast.

We perform this study for $k \in [0;0.4]$. For a given contrast, the forbidden photonic band exists for an interval of k values and it is absent for other k values. The contrast is more important when the interval is large, for a contrast of $1.614 = n_{TiO_2} / n_{SiO_2}$ the band exists only for k lower than 0.2493, for a contrast of 2.41, the band is possible for values lower than 0.3264. Moreover, the curve $\delta\lambda = f(k)$ for a particular contrast have a tendency to increase at the beginning, reach a maximum (the k value corresponding to this maximum increases when increasing the contrast) and then decrease to a value under which, the PBG becomes absent. The PBG middle has the same profile as function of k for different contrasts, the PBG shifts towards the high wavelengths by increasing k. In order to improve the study of the contrast influence on the PBG of the deformed system, we investigate the influence of the index contrast on the deformation effect on the structure transmission spectra i.e. how the increasing of index contrast can improve the significance of deformation. For this, we choose a value of k permitting to have a PBG for the contrast interval studied which is $[1.614;4]$.

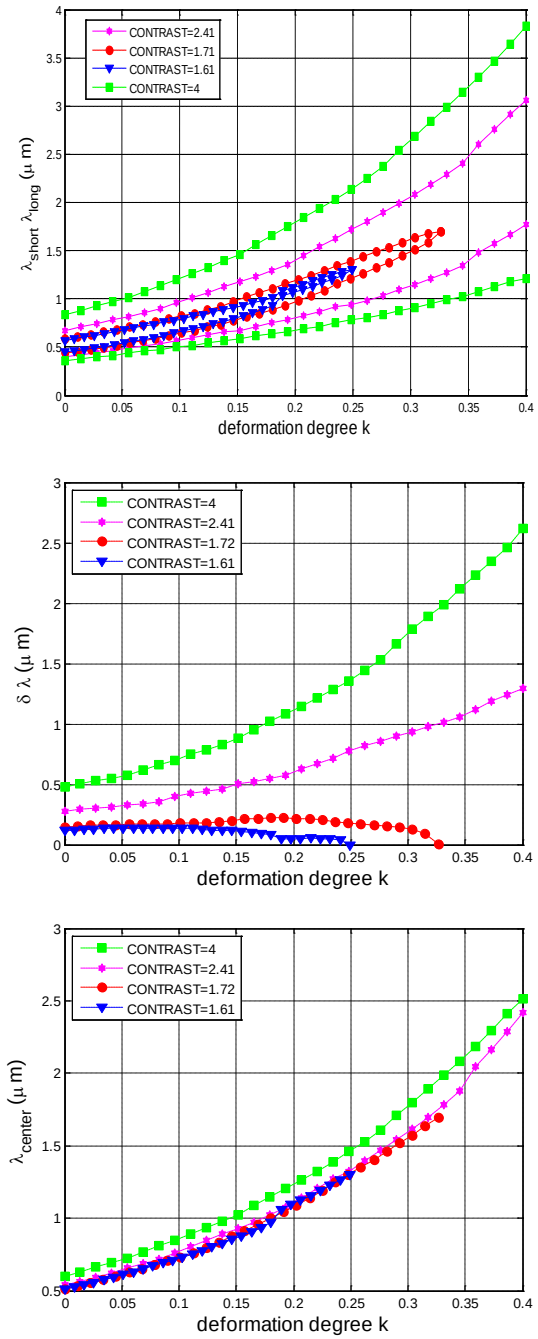

Fig. 2. PBG variation as a function of k for different values of optical index contrast. (a) Variation of the wavelengths of the negligible transmission band extremities as a function of k for different values of optical index contrast. (b) Variation of the bandwidth as a function of k for different values of optical index contrast. (c) Variation of the band center as a function of k for different values of optical index contrast.

We select, for example, the value $k = 0.2$. Then, we display the plot showing the variation of the difference between the PBG width given by a deformed system and that given by the one not deformed according to the index contrast. The widening of the forbidden band according to the contrast is noted for the not deformed system as for the deformed one, but this widening is faster and more significant for the later.

Indeed, Fig. 3 shows that the difference between the bands given by the two systems, deformed and not deformed, increases by increasing the index contrast. We generally conclude that the deformation of the system will have an interest for index contrast values relatively high. It is clear now that the best transmission spectrum is obtained for $x = 4$. Let us choose the best value of k which enables us to have the broadest band belonging to the range $[0.3; 2]$. It is the value $k = 0.2295$.

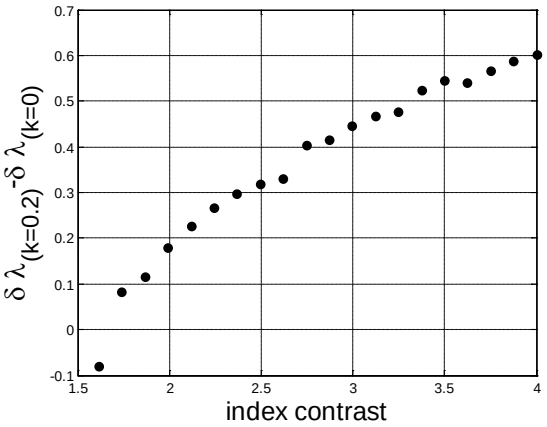

Fig. 3. Difference between the bandwidth of the deformed system and that of the not deformed one as function of the optical index contrast.

Figure 4 shows the transmission spectrum of the system with 31 layers ($j = 15$), contrast=4, and $k = 0.2295$. Its properties are: $\delta\lambda = 1.2676$ μm and $\lambda_{center} = 1.3662$ μm. We note that the PBG covers the three telecommunication wavelengths 0.85 μm, 1.3 μm, and 1.54 μm.

So, these results revealed that the choice of the optical index contrast is very influencing to the quality of the deformation when we consider the normal incidence. That gives us a liberty to choose

x and k according to the needs (spectral range, central wavelength, etc.).

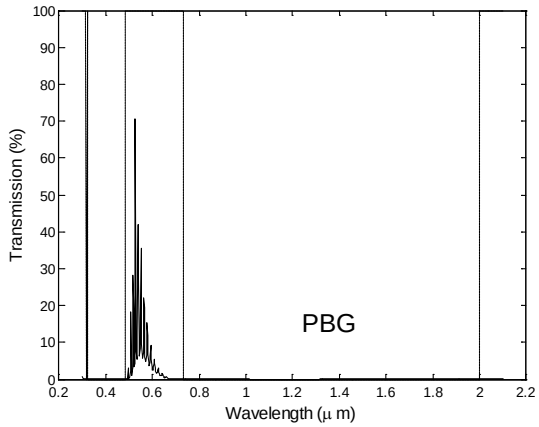

Fig. 4. Transmission at normal incidence of the deformed multilayer structure TiO2(SiO2/TiO2)[15] as a function of wavelength for a reference wavelength λ_0= 0.5 μm and P-polarized light. k=0.2295, x=4. Condition PBG: T<0.01 %.

B. Interaction between the deformation degree and the number of periods

We consider now the interaction between the degree of deformation and the number of periods forming the structure. The indices of the layers are $n_H = 2.34$ and $n_B = 1.45$, the reference wavelength is 0.5 μm.

Figure 5 shows that for a given number of periods, the PBG exists only for an interval of values of k. For example, for $j = 10$, the band exists only if $k \in [0;0.0643]$. For $j = 15$, k must belong to $[0;0.2493]$. For $j = 18$, k must belong to $[0;0.34]$. If we compare Fig. 5 with Fig. 2 which gives the tendency of the optical properties of the transmission spectrum when varying k for different values of contrast, we notice that the influence of increasing j does not represent a great contribution to ameliorate the deformation effect on the structure response. In this case, the PBG middle shifts quickly towards the higher wavelengths when increasing k. Thus, to increase j doesn't represent a great interest for the studied deformed multi-layer structure.

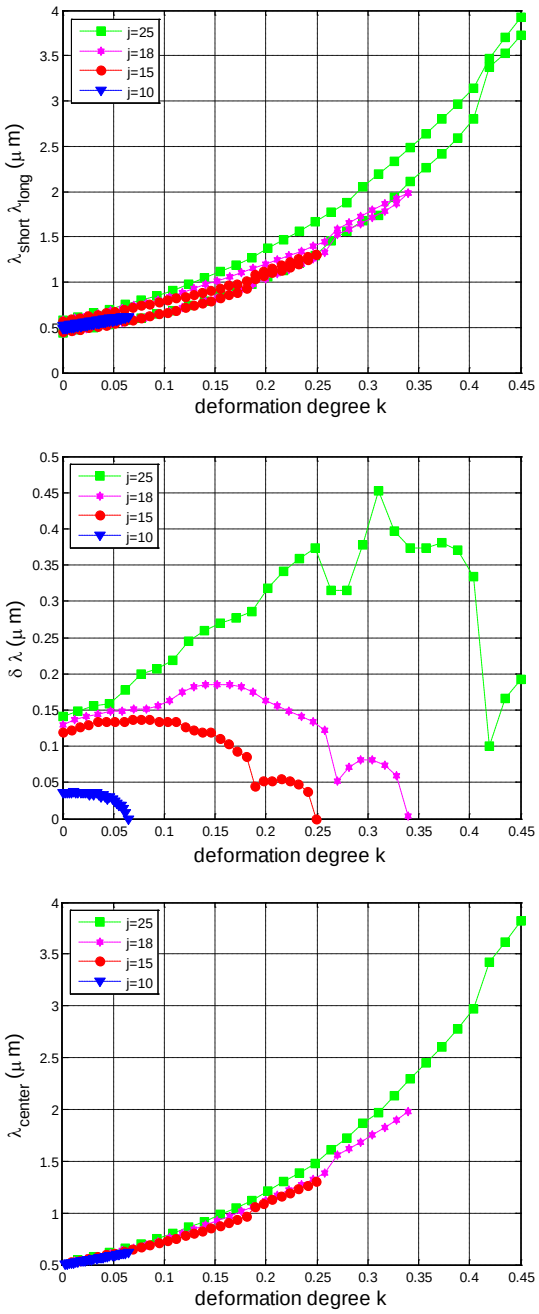

Fig. 5. PBG variation as a function of k for different values of period's number. (a) Variation of the wavelengths of the negligible transmission band extremities as a function of k for different values of period's number. (b) Variation of the bandwidth as a function of k for different values of period's number. (c) Variation of the band center as a function of k for different values of period's number.

Figure 6 gives for each j the corresponding omnidirectional bandwidth for $x = 4$ and $k = 0.2295$. With these conditions, the minimum number of periods is 7 which permits to have a PBG (width =0.0264 μm).

Figure 7 shows the variation of the difference between the PBG width given by a deformed system and that given by the not deformed system according to j with j varies between 7 and 15 periods. For $j = 7$, the deformation has a negative effect on the system response because it reduces the complete bandwidth compared to the not deformed system. But starting from $j = 8$, the deformation improves the response of the system.

C. Interaction between the deformation degree and the reference wavelength λ_0

By studying the interaction between the reference wavelength variation and that of the deformation degree (Fig. 8), we can say that the reference wavelength variation doesn't have any effect on k optimization. Moreover, the curves corresponding to the various values of λ_0 have almost the same tendency, the widening of the band and its displacement according to λ_0 are already noted for the not deformed system. So, the variation of λ_0 does not influence the effect of the deformation.

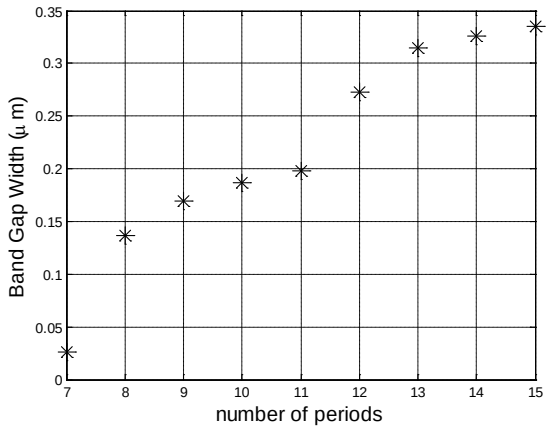

Fig. 6. Variation of the bandwidth as function of the period's number. x=4, k=0.2295.

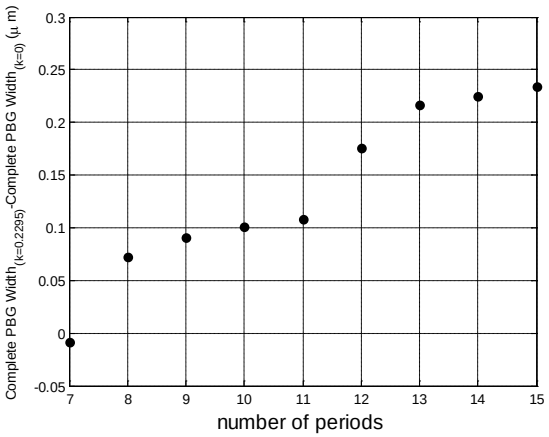

Fig. 7. Difference between the bandwidth of the deformed system and that of the not deformed one as function of the period's number. x=4, k=0.2295.

Moreover, the increase of λ_0 doesn't make it possible to increase the degree of deformation, we are always limited by the value 0.2493 of k. Some is the value of λ_0, the PBG does not exist for values of $k > 0.2493$. The optimal value of k for all the curves is the same one, it is 0.07737.

Figure 9 shows the difference between the PBG width given by a deformed system with $k = 0.07737$ and that given by the not deformed system according to λ_0, it is clear that the difference does not progress much with the wavelength reference. We thus note that the variation of the reference wavelength doesn't represent a good way to improve the effect of the deformation on the system response.

VI. CONCLUSION

We can consider the present work very interesting since it presents an optimization multi-parameter of the chirped multi-layer structure. We investigated the behaviour of the optical properties of the system versus the variation of its parameters. The interest of the deformation is not always concluded, it depends on the selected parameters of the system. This study can represent a support which gives for which parameters of the system we can consider the deformation interesting and which are the corresponding values of k optimum. In general, we can say that if we want to improve the performances of the optical

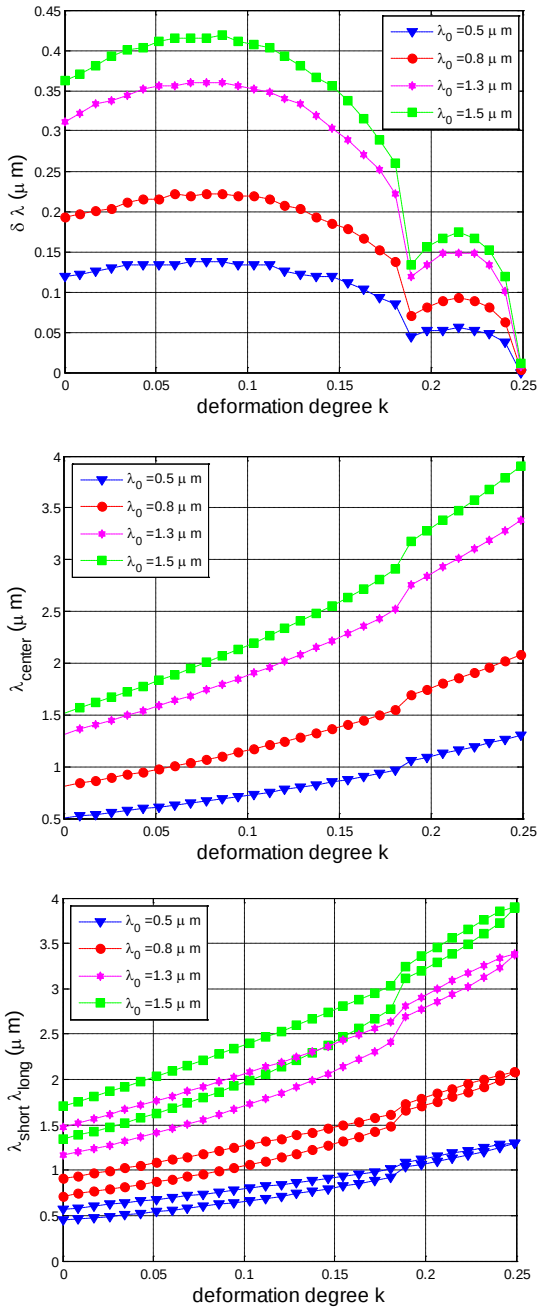

Fig. 8. PBG variation as a function of k for different values of reference wavelength. (a) Variation of the bandwidth as a function of k for different values of reference wavelength. (b) Variation of the band center as a function of k for different values of reference wavelength. (c) Variation of the wavelengths of the negligible transmission band extremities as a function of k for different values of reference wavelength.

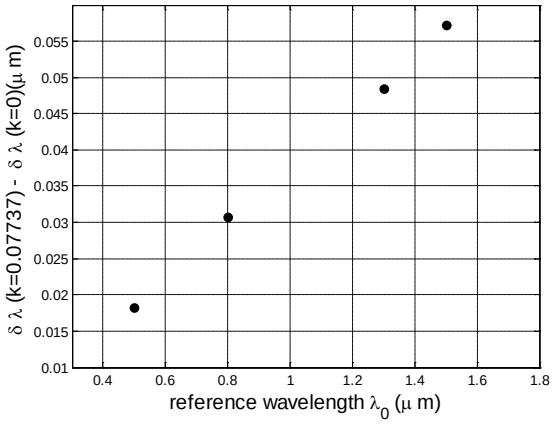

Fig. 9. Difference between the bandwidth of the deformed system and that of the not deformed one as function of the reference wavelength. k=0.07737.

components at normal incidence, it is preferable to choose the maximum index contrast and the highest degree of deformation which gives the best response which meets our needs.

REFERENCES

[1] T.F. Krauss, "Slow Light in Photonic Crystal Waveguides," *J. Phys. D: Appl. Phys.*, vol. 40, pp. 2666-2670, 2007.

[2] C. Kang and M. S. Weiss, "Photonic Crystal Defect Tuning for Optimized Light-Matter Interaction," *Proc. SPIE*, 7031, 70310G, 2008.

[3] F. Bordas, C. Seassal, E. Dupuy, P. Regreny, M. Gendry, P. Viktorovitch, M. J. Steel, and A. Rahmani, "Room Temperature Low-Threshold in As/InP Quantum Dot Single Mode Photonic Crystal Microlasers at 1.5 μm using Cavity-Confined Slow Light," *Optics Express*, vol. 17, pp. 5439-5445, 2009.

[4] R. H. Lipson and C. Lu, "Photonic Crystals: A Unique Partnership Between Light and Matter," *Eur. J. Phys.*,vol. 30, pp. 33-48, 2009.

[5] J. Smajic, C. Hafner, D. Erni, Jasmin Smajic, Christian Hafner, and Daniel Erni, "Automatic Calculation of Band Diagrams of Photonic Crystals Using the Multiple Multipole Method," *Applied Computational Electromagnetic Society (ACES) Journal*, vol. 18, no. 3, pp. 172-180, 2003.

[6] Z. F. Sang and Z. Y. Li, "Optical Properties of One-Dimensional Photonic Crystals Containing Graded Material," *Optics Communications*, vol. 259, pp. 174-178, 2006.
[7] K. Busch and S. John, "Liquid-Crystal Photonic-Band-Gap Materials: The Tunable Electromagnetic Vacuum," *Phys. Rev. Lett.*, vol. 83, pp. 967-970, 1999.
[8] K. R. Khan and T. X. Wu, "Finite Element Modeling of Dual-Core Photonic Crystal Fiber," *Applied Computational Electromagnetic Society (ACES) Journal*, vol. 23, no. 3, pp. 215-219, 2008.
[9] J. Zaghdoudi, M. Kanzari, and B. Rezig, "Design of Omnidirectional Asymmetrical High Reflectors for Optical Telecommunication Wavelengths," *Eur. Phys. J.*, vol. 42, pp. 181-186, 2004.
[10] J. Zaghdoudi, M. Kanzari, and B. Rezig, "Design of Omnidirectional High Reflectors for Optical Telecommunication Bands using the Deformed Quasiperiodic One Dimensional Photonic Crystals," *ICTON Tu.*, p. 7, 2005.
[11] J. Zaghdoudi, M. Aissaoui, M. Kanzari, and B. Rezig, "Optical Properties of Periodic and Quasiperiodic One Dimensional Photonic Crystals: A Comparison," *Proc. Of SPIE* 6182, 61822J, 2006.
[12] J. Zaghdoudi, M. Kanzari, and B. Rezig, "A Dielectric Chirped Layered Mirror for Optical Telecommunication Wavelengths," *Opt. Rev.*, vol. 14(2), pp. 91-96, 2007.
[13] Z. LI, "Principles of the Plane-Wave Transfer-Matrix Method for Photonic Crystals," *Science and Technology of Advanced Materials*, vol. 6, pp. 837-841, 2005.
[14] F. Abelès, *Ann Phys.*, Paris 12, 596, 1950.

2011 INSTITUTIONAL MEMBERS

DTIC-OCP LIBRARY
8725 John J. Kingman Rd, Ste 0944
Fort Belvoir, VA 22060-6218

AUSTRALIAN DEFENCE LIBRARY
Northcott Drive
Canberra, A.C.T. 2600 Australia

BEIJING BOOK CO, INC
701 E Linden Avenue
Linden, NJ 07036-2495

DARTMOUTH COLLEGE
6025 Baker/Berry Library
Hanover, NH 03755-3560

DSTO EDINBURGH
AU/33851-AP, PO Box 830470
Birmingham, AL 35283

SIMEON J. EARL – BAE SYSTEMS
W432A, Warton Aerodome
Preston, Lancs., UK PR4 1AX

ENGINEERING INFORMATION, INC
PO Box 543
Amsterdam, Netherlands 1000 Am

ETSE TELECOMUNICACION
Biblioteca, Campus Lagoas
Vigo, 36200 Spain

GA INSTITUTE OF TECHNOLOGY
EBS-Lib Mail code 0900
74 Cherry Street
Atlanta, GA 30332

TIMOTHY HOLZHEIMER
Raytheon
PO Box 1044
Rockwall, TX 75087

HRL LABS, RESEARCH LIBRARY
3011 Malibu Canyon
Malibu, CA 90265

IEE INSPEC
Michael Faraday House
6 Hills Way
Stevenage, Herts UK SG1 2AY

INSTITUTE FOR SCIENTIFIC INFO.
Publication Processing Dept.
3501 Market St.
Philadelphia, PA 19104-3302

LIBRARY – DRDC OTTAWA
3701 Carling Avenue
Ottawa, Ontario, Canada K1A OZ4

LIBRARY of CONGRESS
Reg. Of Copyrights
Attn: 407 Deposits
Washington DC, 20559

LINDA HALL LIBRARY
5109 Cherry Street
Kansas City, MO 64110-2498

MISSOURI S&T
400 W 14th Street
Rolla, MO 56409

MIT LINCOLN LABORATORY
Periodicals Library
244 Wood Street
Lexington, MA 02420

NATIONAL CHI NAN UNIVERSITY
Lily Journal & Book Co, Ltd
20920 Glenbrook Drive
Walnut, CA 91789-3809

JOHN NORGARD
UCCS
20340 Pine Shadow Drive
Colorado Springs, CO 80908

OSAMA MOHAMMED
Florida International University
10555 W Flagler Street
Miami, FL 33174

NAVAL POSTGRADUATE SCHOOL
Attn:J. Rozdal/411 Dyer Rd./ Rm 111
Monterey, CA 93943-5101

NDL KAGAKU
C/0 KWE-ACCESS
PO Box 300613 (JFK A/P)
Jamaica, NY 11430-0613

OVIEDO LIBRARY
PO BOX 830679
Birmingham, AL 35283

DAVID PAULSEN
E3Compliance
1523 North Joe Wilson Road
Cedr Hill, TX 75104-1437

PENN STATE UNIVERSITY
126 Paterno Library
University Park, PA 16802-1808

DAVID J. PINION
1122 E Pike Street #1217
SEATTLE, WA 98122

KATHERINE SIAKAVARA
Gymnasiou 8
Thessaloniki, Greece 55236

SWETS INFORMATION SERVICES
160 Ninth Avenue, Suite A
Runnemede, NJ 08078

YUTAKA TANGE
Maizuru Natl College of Technology
234 Shiroya
Maizuru, Kyoto, Japan 625-8511

TIB & UNIV. BIB. HANNOVER
DE/5100/G1/0001
Welfengarten 1B
Hannover, Germany 30167

UEKAE
PO Box 830470
Birmingham, AL 35283

UNIV OF CENTRAL FLORIDA
4000 Central Florida Boulevard
Orlando, FL 32816-8005

UNIVERSITY OF COLORADO
1720 Pleasant Street, 184 UCB
Boulder, CO 80309-0184

UNIVERSITY OF KANSAS – WATSON
1425 Jayhawk Blvd 210S
Lawrence, KS 66045-7594

UNIVERSITY OF MISSISSIPPI
JD Williams Library
University, MS 38677-1848

UNIVERSITY LIBRARY/HKUST
Clear Water Bay Road
Kowloon, Honk Kong

CHUAN CHENG WANG
8F, No. 31, Lane 546
MingCheng 2nd Road, Zuoying Dist
Kaoshiung City, Taiwan 813

THOMAS WEILAND
TU Darmstadt
Schlossgartenstrasse 8
Darmstadt, Hessen, Germany 64289

STEVEN WEISS
US Army Research Lab
2800 Powder Mill Road
Adelphi, MD 20783

YOSHIHIDE YAMADA
NATIONAL DEFENSE ACADEMY
1-10-20 Hashirimizu
Yokosuka, Kanagawa,
Japan 239-8686

APPLIED COMPUTATIONAL ELECTROMAGNETICS SOCIETY JOURNAL
http://aces.ee.olemiss.edu

INFORMATION FOR AUTHORS

PUBLICATION CRITERIA

Each paper is required to manifest some relation to applied computational electromagnetics. **Papers may address general issues in applied computational electromagnetics, or they may focus on specific applications, techniques, codes, or computational issues.** While the following list is not exhaustive, each paper will generally relate to at least one of these areas:

1. **Code validation.** This is done using internal checks or experimental, analytical or other computational data. Measured data of potential utility to code validation efforts will also be considered for publication.

2. **Code performance analysis.** This usually involves identification of numerical accuracy or other limitations, solution convergence, numerical and physical modeling error, and parameter tradeoffs. However, it is also permissible to address issues such as ease-of-use, set-up time, run time, special outputs, or other special features.

3. **Computational studies of basic physics.** This involves using a code, algorithm, or computational technique to simulate reality in such a way that better, or new physical insight or understanding, is achieved.

4. **New computational techniques** or new applications for existing computational techniques or codes.

5. **"Tricks of the trade"** in selecting and applying codes and techniques.

6. **New codes, algorithms, code enhancement, and code fixes.** This category is self-explanatory, but includes significant changes to existing codes, such as applicability extensions, algorithm optimization, problem correction, limitation removal, or other performance improvement. **Note: Code (or algorithm) capability descriptions are not acceptable, unless they contain sufficient technical material to justify consideration.**

7. **Code input/output issues.** This normally involves innovations in input (such as input geometry standardization, automatic mesh generation, or computer-aided design) or in output (whether it be tabular, graphical, statistical, Fourier-transformed, or otherwise signal-processed). Material dealing with input/output database management, output interpretation, or other input/output issues will also be considered for publication.

8. **Computer hardware issues.** This is the category for analysis of hardware capabilities and limitations of various types of electromagnetics computational requirements. Vector and parallel computational techniques and implementation are of particular interest.

Applications of interest include, but are not limited to, antennas (and their electromagnetic environments), networks, static fields, radar cross section, inverse scattering, shielding, radiation hazards, biological effects, biomedical applications, electromagnetic pulse (EMP), electromagnetic interference (EMI), electromagnetic compatibility (EMC), power transmission, charge transport, dielectric, magnetic and nonlinear materials, microwave components, MEMS, RFID, and MMIC technologies, remote sensing and geometrical and physical optics, radar and communications systems, sensors, fiber optics, plasmas, particle accelerators, generators and motors, electromagnetic wave propagation, non-destructive evaluation, eddy currents, and inverse scattering.

Techniques of interest include but not limited to frequency-domain and time-domain techniques, integral equation and differential equation techniques, diffraction theories, physical and geometrical optics, method of moments, finite differences and finite element techniques, transmission line method, modal expansions, perturbation methods, and hybrid methods.

Where possible and appropriate, authors are required to provide statements of quantitative accuracy for measured and/or computed data. This issue is discussed in "Accuracy & Publication: Requiring, quantitative accuracy statements to accompany data," by E. K. Miller, *ACES Newsletter*, Vol. 9, No. 3, pp. 23-29, 1994, ISBN 1056-9170.

SUBMITTAL PROCEDURE

All submissions should be uploaded to ACES server through ACES web site (http://aces.ee.olemiss.edu) by using the upload button, journal section. Only pdf files are accepted for submission. The file size should not be larger than 5MB, otherwise permission from the Editor-in-Chief should be obtained first. Automated acknowledgment of the electronic submission, after the upload process is successfully completed, will be sent to the corresponding author only. It is the responsibility of the corresponding author to keep the remaining authors, if applicable, informed. Email submission is not accepted and will not be processed.

EDITORIAL REVIEW

In order to ensure an appropriate level of quality control, papers are peer reviewed. They are reviewed both for technical correctness and for adherence to the listed guidelines regarding information content and format.

PAPER FORMAT

Only camera-ready electronic files are accepted for publication. The term **"camera-ready" means that the material is neat, legible, reproducible, and in accordance with the final version format listed below.**

The following requirements are in effect for the final version of an ACES Journal paper:

1. The paper title should not be placed on a separate page.

The title, author(s), abstract, and (space permitting) beginning of the paper itself should all be on the first page. The title, author(s), and author affiliations should be centered (center-justified) on the first page. The title should be of font size 16 and bolded, the author names should be of font size 12 and bolded, and the author affiliation should be of font size 12 (regular font, neither italic nor bolded).

2. An abstract is required. The abstract should be a brief summary of the work described in the paper. It should state the computer codes, computational techniques, and applications discussed in the paper (as applicable) and should otherwise be usable by technical abstracting and indexing services. The word "Abstract" has to be placed at the left margin of the paper, and should be bolded and italic. It also should be followed by a hyphen (—) with the main text of the abstract starting on the same line.

3. All section titles have to be centered and all the title letters should be written in caps. The section titles need to be numbered using roman numbering (I. II. ….)

4. Either British English or American English spellings may be used, provided that each word is spelled consistently throughout the paper.

5. Internal consistency of references format should be maintained. As a guideline for authors, we recommend that references be given using numerical numbering in the body of the paper (with numerical listing of all references at the end of the paper). The first letter of the authors' first name should be listed followed by a period, which in turn, followed by the authors' complete last name. Use a coma (,) to separate between the authors' names. Titles of papers or articles should be in quotation marks (" "), followed by the title of journal, which should be in italic font. The journal volume (vol.), issue number (no.), page numbering (pp.), month and year of publication should come after the journal title in the sequence listed here.

6. Internal consistency shall also be maintained for other elements of style, such as equation numbering. Equation numbers should be placed in parentheses at the right column margin. All symbols in any equation have to be defined before the equation appears or right immediately following the equation.

7. The use of SI units is strongly encouraged. English units may be used as secondary units (in parentheses).

8. Figures and tables should be formatted appropriately (centered within the column, side-by-side, etc.) on the page such that the presented data appears close to and after it is being referenced in the text. When including figures and tables, all care should be taken so that they will appear appropriately when printed in black and white. For better visibility of paper on computer screen, it is good to make color figures with different line styles for figures with multiple curves. Colors should also be tested to insure their ability to be distinguished after black and white printing. Avoid the use of large symbols with curves in a figure. It is always better to use different line styles such as solid, dotted, dashed, etc.

9. A figure caption should be located directly beneath the corresponding figure, and should be fully justified.

10. The intent and meaning of all text must be clear. For authors who are not masters of the English language, the ACES Editorial Staff will provide assistance with grammar (subject to clarity of intent and meaning). However, this may delay the scheduled publication date.

11. Unused space should be minimized. Sections and subsections should not normally begin on a new page.

ACES reserves the right to edit any uploaded material, however, this is not generally done. It is the author(s) responsibility to provide acceptable camera-ready files in pdf and MSWord formats. Incompatible or incomplete files will not be processed for publication, and authors will be requested to re-upload a revised acceptable version.

COPYRIGHTS AND RELEASES

Each primary author must execute the online copyright form and obtain a release from his/her organization vesting the copyright with ACES. Both the author(s) and affiliated organization(s) are allowed to use the copyrighted material freely for their own private purposes.

Permission is granted to quote short passages and reproduce figures and tables from and ACES Journal issue provided the source is cited. Copies of ACES Journal articles may be made in accordance with usage permitted by Sections 107 or 108 of the U.S. Copyright Law. This consent does not extend to other kinds of copying, such as for general distribution, for advertising or promotional purposes, for creating new collective works, or for resale. The reproduction of multiple copies and the use of articles or extracts for commercial purposes require the consent of the author and specific permission from ACES. Institutional members are allowed to copy any ACES Journal issue for their internal distribution only.

PUBLICATION CHARGES

All authors are allowed for 8 printed pages per paper without charge. Mandatory page charges of $75 a page apply to all pages in excess of 8 printed pages. Authors are entitled to one, free of charge, copy of the printed journal issue in which their paper was published. Additional reprints are available for $ 50. Requests for additional re-prints should be submitted to the managing editor or ACES Secretary.

Corresponding author is required to complete the online form for the over page charge payment right after the initial acceptance of the paper is conveyed to the corresponding author by email.

ACES Journal is abstracted in INSPEC, in Engineering Index, DTIC, Science Citation Index Expanded, the Research Alert, and to Current Contents/Engineering, Computing & Technology.